Title
Turbulence-driven shear flow and self-regulating drift wave turbulence in a cylindrical plasma device

Author
Yan, Zheng

Publication Date
2009

UNIVERSITY OF CALIFORNIA, SAN DIEGO

Turbulence-driven shear flow and self-regulating drift wave turbulence in a cylindrical plasma device

A dissertation submitted in partial satisfaction of the
requirements for the degree Doctor of Philosophy
in
Engineering Science (Mechanical Engineering)

by

Zheng Yan

Committee in charge:

Professor George R. Tynan, Chair
Professor Paul F. Linden
Professor Juan C. Lasheras
Professor Farrokh Najmabadi
Professor Clifford M. Surko

2009

The dissertation of Zheng Yan is approved, and it is acceptable in quality and form for publication on microfilm:

Chair

University of California, San Diego

2009

To my parents Renqin and Zhenhong

To my husband Long and my son Haowen

TABLE OF CONTENTS

LIST OF FIGURES

ACKNOWLEDGEMENTS

–Zheng Yan

This is a great opportunity to express my gratitude to all those people who have given me the possibility to complete this dissertation.

My deepest gratitude is to my advisor, Prof. George R. Tynan. I have been very fortunate to have him as my advisor. He has taught me a lot about physics, science and life in general. He encouraged me to not only grow as an experimentalist but also as an independent thinker. His patience and support all along helped me overcome many hard situations in life and finish this dissertation. I owe my deepest gratitude to him.

I also owe a great deal of thanks to a number of teachers and scientists, who helped me a lot along the way. At Southeast University in China, Prof. Yiqian Xu, Prof. Fan Gu and Prof. Jun Zhang have guided me with a great introduction to the world of science. At UCSD, Dr. Christopher Holland, Dr. Jonathan Yu and Dr. Stefan M$\ddot{u}$ller have provided me a lot assistance and guidance in area of analysis, experimentation, computer and theory. Dr. Karl R. Umstadter, Dr. Eric Hollmann and Dr. Ray Seraydarian are always available when I need help.

I would also like to express my sincere thanks to the people who have been working in CSDX and PISCES group, including Russ Doerner, Daisuke Nishijima, Leo Chousal, Rolando Hernandez, Tyler Lynch, Min Xu, Laizhong Cai, Nazli Taheri, Timothy R. Palmer and Richard David Price. Especially thank Leo Chousal and Rolando Hernandez for their invaluable help to me in the lab work, Min Xu and Laizhong Cai for their friendship and help on the experiments.

The UCSD Mechanical and Aerospace Engineering department staff do an excellent job of making a graduate student's life easier. In particular, I would thank Cynthia Escobedo, Brandi Pate and Ruth Lingo for their care for me and my baby son.

My sincere gratitudes are also owed to my Ph.D committee members, Prof. Paul

F. Linden, Prof. Juan C. Lasheras, Prof. Farrokh Najmabadi and Prof. Clifford M. Surko. Thank them for reviewing my thesis and the valuable comments.

Finally, I would like to give my special thanks to my family. Thanks to my parents, Renqin Yuan and Zhenhong Yan, as well as my parents in-law, Jun Wu and Danian Sun, for their love and support over the years.

Most of all, I want to thank my husband, Long Sun. His love, support and encouragement make the way worth it. Thank is as well to my baby son, Haowen. His coming to this world has been making me happier than I can say.

The text and data in Chapter 3, in full, is a reprint of the material as it appears in 'The statistical properties of the turbulent Reynolds stress and its link to the shear flow generation', Z.Yan, J.H.Yu, C.Holland, M.Xu, S.H.M$\ddot{u}$ller and George Tynan, Phys. Plasmas, 15, 092309 (2008). Copyright 2008 American Institute of Physics. The dissertation author was the primary investigator and author of this paper.

This work is supported by the DoE Grant No. DE-FG02-06ER54871.

VITA

1999	B.S., Southeast University, Nanjing, China
2002	M.S., Southeast University, Nanjing, China
2002–2008	Graduate Student Researcher, Center of Energy Research, University of California, San Diego, California, USA
2008	Teaching Assistant, Department of Mechanical and Aerospace Engineering, University of California, San Diego, California, USA
2009	Ph.D., University of California, San Diego, California, USA

PUBLICATIONS

Z.Yan, J.H.Yu, C.Holland, M.Xu, S.H.Muller, and G.R.Tynan, 'Statistical analysis of the turbulent Reynolds stress and its link to the shear flow generation in a cylindrical laboratory plasma device', Phys. of Plasmas, 15, 092309, 2008

E.M.Hollmann, A.Y.Pigarov, Z.Yan, 'Measurement and modeling of detached plasma cooling via ro-vibrational excitation of H-2 neutrals in PISCES-A', Journal of Nuclear Materials, 363: 359-364, 2007

J.H.Yu, C.Holland, G.R.Tynan, G.Antar, Z.Yan, 'Examination of the velocity time-delay-estimation technique', Journal of Nuclear Materials, 363-365, 728-732, 2007

FIELDS OF STUDY

Major Field: Engineering Science (Mechanical Engineering)

Studies in Plasma Physics
Professor George R. Tynan

Studies in Fluid Mechanics
Professor Paul F. Linden

Studies in Applied Mathematics
Professor Stefan Llewellyn Smith

ABSTRACT OF THE DISSERTATION

Turbulence-driven shear flow and self-regulating drift wave turbulence in a cylindrical plasma device

by

Zheng Yan

Doctor of Philosophy in Engineering Science (Mechanical Engineering)

University of California, San Diego, 2009

Professor George R. Tynan, Chair

This dissertation provides an experimental test of the basic theory of the self-regulating drift wave turbulence (DWT)/sheared zonal flow (ZF) system in a cylindrical plasma device. The work is carried out from three approaches: the first explores the statistical properties of the turbulent Reynolds stress and its link to the ZF generation, the second investigates the dynamical behavior of the DWT/ZF system and the third investigates the variation of the DWT driven ZF verses magnetic field strength and ion-neutral drag.

A radially sheared azimuthally symmetric plasma flow is generated by the DWT turbulent Reynolds stress which is directly measured by a multi-tip Langmuir probe. A statistical analysis shows that the cross-phase between the turbulent radial and azimuthal velocity components is the key factor determining the detailed Reynolds stress profile. The coincidence of the radial location of the non-Gaussian distribution of the turbulent Reynolds stress and the ion saturation current, as well as the properties of the joint probability distribution function (PDF) between the radial particle flux and turbulent Reynolds stress suggest that the bursts of the particle transport appear to be associated with radial transport of azimuthal momentum as well. The results link the behavior of the Reynolds stress, its statistical properties, generation of bursty radially going azimuthal momentum transport events, and the formation of the large-scale ZF.

From both Langmuir probe and fast-faming imaging measurements this shear flow is found to evolve with low frequency ($\sim$250-300Hz). The envelope of the higher frequency (above 5kHz) floating potential fluctuations associated with the DWT, the density gradient, and the turbulent radial particle flux are all modulated out of phase with the strength of the ZF. The divergence of the turbulent Reynolds stress is also modulated at the same slow time scale in a phase-coherent manner consistent with a turbulence-driven shear flow sustained against the collisional and viscous damping, and the radial turbulence correlation length and cross field particle transport are reduced during periods of strong flow shear. The results are qualitatively consistent with theoretical expectations for coupled DWT-ZF dynamics.

The drift turbulence/zonal flow system shows a strong variation with magnetic field and neutral gas pressure. The density fluctuation amplitude, radial particle flux and the absolute value of the divergence of the turbulent Reynolds stress at shear layer and the shear flow are negligible when B$\sim$600G. As the magnetic field is raised, these quantities all exhibit a rapid increase for 600G $<$B $<$700G. When B $>$700G these quantities increase at a slower rate. The ZF is stronger at lower neutral pressure and weaker at higher neutral pressure, and the density fluctuation amplitude, radial particle flux and the absolute value of the divergence of the turbulent Reynolds stress at shear layer and the shear flow all

decrease with an increase of the neutral pressure.

1

Introduction

1.1 Motivation

As the energy demand of the world grows rapidly, the well known problems that exist in our current energy system such as climate change and security of supply become even more severe. Controlled fusion may be an attractive future energy options. The typical fusion reactions are [1]:

$$D + D \rightarrow He^3(0.82MeV) + n(2.45MeV) \tag{1.1}$$

$$D + D \rightarrow T(1.01MeV) + p(3.02MeV) \tag{1.2}$$

$$D + T \rightarrow He(3.5MeV) + n(14.1MeV) \tag{1.3}$$

To achieve net energy gain, the fusion plasma must be maintained at a high temperature, T, with a sufficient ion density n, for a sufficient time τ_E. An important measure of this is the Lawson's criterion [2], as shown by the Eqn.1.4 and Eqn.1.5, which gives the minimum condition for an energy producing fusion reaction.

$$n\tau_E \geq 10^{14} s/cm^3 \qquad for \qquad deuterium - tritium \qquad fusion \tag{1.4}$$

$$n\tau_E \geq 10^{16} s/cm^3 \qquad for \qquad deuterium - deuterium \qquad fusion \tag{1.5}$$

The plasma pressure, $p = nT$ is limited by large-scale Magnetohydrodynamics (MHD) instabilities. Thus there exists a minimum value of the energy confinement time, τ_E defined as the total energy content of the plasma W divided by power loss P_{loss} (rate of energy loss)[1],for which energy gain is possible:

$$\tau_E = \frac{W}{P_{loss}} \tag{1.6}$$

If the heat transport is diffusive, then the energy confinement time τ_E scales as $\tau_E \sim L^2/\chi_i$, where $L = T/\nabla T$ is the temperature gradient scale length and χ_i is ion thermal diffusion coefficient such that the heat flux $q = -n\chi_i \frac{\partial T}{\partial r}$. In the random walk model χ_i scales as $\chi_i \sim \frac{(\Delta l)^2}{\tau_r}$, where $(\Delta l)^2$ is the magnitude of the average step size between collisions and τ_r is the average time between random walk steps. Therefore τ_E scales as $\tau_E \sim \frac{L^2}{(\Delta l)^2}\tau_r$. Thus a decrease in $(\Delta l)^2$ or increase in τ_r will lead to increase in τ_E and thus make it easier to reach Lawson criterion. Neoclassical transport theory (due solely to the coulomb collisions) gives the minimum possible value for χ and maximum possible value for τ_E. However, these values are too optimistic when compared to experimental observations. The experimental data show that actual ion thermal conductivity is anomalously large by a factor on the order of $1 - 10$ with respect to the neoclassical χ_i, while the electron heat conduction and particle diffusion coefficients are each anomalous by about two orders of magnitude larger than expected from neoclassical theory[1]. This discrepancy has made the achievement of energy producing fusion reaction challenging.

It now has been generally accepted that the so-called 'anomalous' cross field transport is in fact due to the plasma turbulence which is driven by free energy sources in the plasma. Such free energy sources are, for example, due to the density gradient, temperature gradient, and/or non-equilibrium distribution function [3]. See Carreras [4] for a review on the turbulent processes in magnetized plasma. Plasma turbulence may cause random perturbations in the guiding center orbits of the particles. The randomness of the fluctuations leads to a collision-like diffusion of particles and energy and increase the averaged step size. Turbulent transport, therefore, limits particle and energy confinements in magnetic confinement devices. Thus the real problem of understanding anomalous transport is understanding plasma turbulence, which is critical to achieve a positive net energy gain. Fig.1.1a is a sample density fluctuation measurements[5] obtained with beam-emission-spectroscopy (BES)[6] in DIIID tokamak[7]. The plots are for two poloidally adjacent channels near $r/a = 0.95$ position(r is minor radius and a is major radius in toroidal geometry). The ambient turbulence amplitude is relatively large, $\tilde{n}/n \geq 5\%$.

More recently modeling and theory suggest that the saturation of turbulence is mediated by the self-generated zonal flow. Such flow can be spontaneously generated by the turbulence via turbulent Reynolds stresses (i.e. the turbulent transport of momentum) in a way similar to the formation of zonal flows in planetary atmospheres and rotating fluids [8, 9]. From a spectral point of view, this process can be considered to be nonlinear energy transfer of kinetic energy from small-scaled turbulence into large-scaled shear flow.

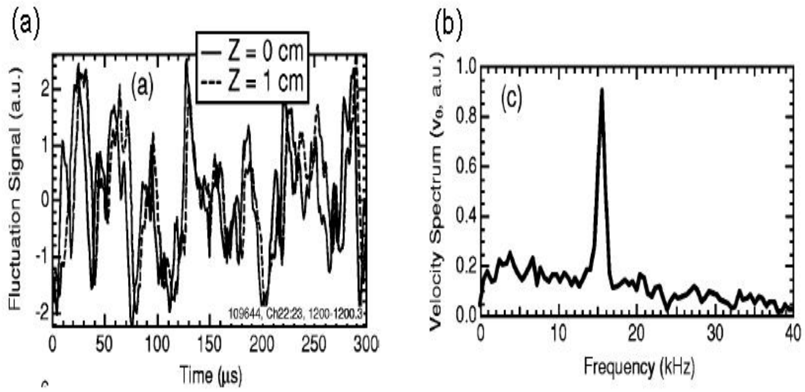

Figure 1.1: (a) Sample density fluctuation measurements from two poloidally adjacent channels near $r/a = 0.95$. (b) The power spectrum of the derived poloidal velocity exhibiting coherent oscillations near 15.5kHz[5].

These zonal flows exhibit a low frequency branch, referred as the 'residual' zonal flow (ZF) or Hinton-Rosenbluth mode [10, 11] and a related higher frequency branch, identified as geodesic acoustic modes (GAM)[12, 13]. Both the ZF and GAM are toroidally and poloidally symmetric $\vec{E} \times \vec{B}$ flows that exhibit a significant radial (i.e., the direction parallel to the mean plasma gradient) shear. Fig.1.1b is a power spectrum of the poloidal velocity obtained by applying time-delay-estimation (TDE) to the BES density fluctuation measurements in the edge of the DIIID tokamak[5]. The poloidal flow exhibits a coherent mode ~ 15.5kHz. Fig.1.2a shows the radial and poloidal phase relationship of the coherent poloidal flow while Fig.1.2b hows a sample snap shot of the 2D flow field, inferred from ensemble average 2D cross-correlation. It clearly shows the radial shear and poloidal uniformity. The results in the literature[5] have demonstrated the observed flow oscillation is a GAM. Similar results are available for the ZF as well.

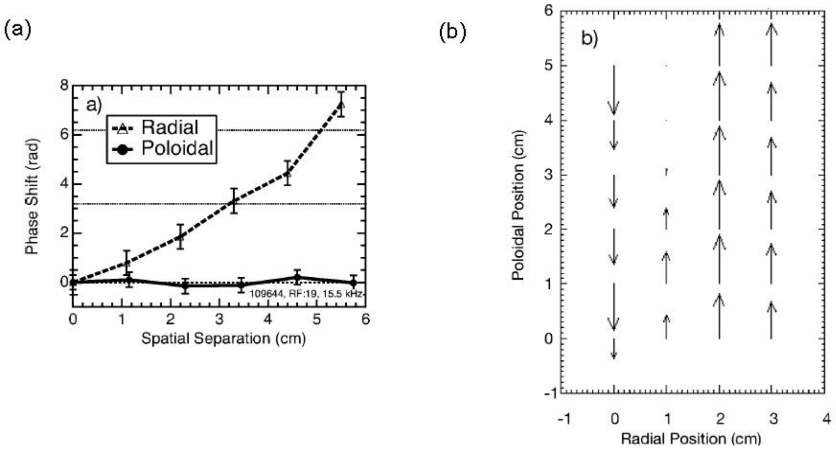

Figure 1.2: (a) Radial and poloidal phase relationship of coherent v_θ oscillation at 15.5kHz. (b) Sample snap shot of 2D flow field of 15.5kHz v_θ oscillation[5].

Theory predicts that the zonal flow random shearing effect on the turbulence will regulate the amplitude and size of the turbulence. In addition, theory predicts that the shear flow is nonlinearly driven by the turbulence. Thus the plasma turbulence and shear flow form a self-regulating system [8]. In experiments it is found sometimes plasma can spontaneously transition from a state with strong turbulent transport (L-mode) to a state with significantly reduced anomalous transport (H-mode)[14, 15], resulting in a 2-3 times increase in τ_E. The formation of such 'Transport barrier' is represented as extreme example of the effect of a shear flow on turbulence. Therefore, understanding the mechanism of the zonal flow generation and the turbulence/ZF interaction play a crucial role in understanding the turbulent transport, which is a critical issue for magnetic fusion research. Although modeling and theory have effectively predicted and interpreted the improvement of plasma confinement, these models still require further experimental tests. In particular, the dynamical behavior of the DWT/ZF system and the non-linear coupling between the DWT and ZF are critical issue requiring experimental study. However, because of the complications that arise from the complicated toroidal geometry, diagnostic limitations and limited access, there have not yet been conclusive evidences to validate this basic theory. These studies of turbulence-driven shear flow in a cylindrical plasma device were motivated by this situation. In the following two sections we will first give an overview of the basic physics of the drift-wave turbulence and the zonal flow generation. We then summarize previous experimental results, based on which we then describe the aim of this thesis.

1.2 Overview of drift-wave turbulence

A single charged particle in magnetic field will execute a circular motion (gyromotion) around the field line due to the Lorentz force. However a typical plasma density might be 10^{12} ion-electron pairs per cm^3, and each follows a complicated trajectory. Therefore, it will be hopeless to predict the plasma behavior by following each single particle. Some of the plasma phenomena observed in real experiments, particularly in low temperature experiments where collisions are strong, can be explained by a fluid description of the ion and electron motion[16]. Each species of the plasma particles (electrons and each type of ions) is described by a set of fluid equations (analogous to the Navier-Stokes equation, but accounting for the fast gyromotion of the charged particles around the magnetic field) for density n and velocity $\vec{u}$ [16].

$$\frac{\partial n}{\partial t} + \nabla \cdot (n\vec{u}) = 0 \tag{1.7}$$

$$mn\left[\frac{\partial \vec{u}}{\partial t} + (\vec{u} \cdot \vec{\nabla})\vec{u}\right] = en(\vec{E} + \vec{u} \times \vec{B}) - \vec{\nabla}p - \vec{\nabla} \cdot \Pi + \vec{R} \tag{1.8}$$

where, Π is the anisotropic viscous tensor and $\vec{R}$ represents the exchange of momentum with other fluid species (e.g. ions with electrons and neutrals). These equations combined with Maxwell's equations provide a complete description of the plasma.

A spatially inhomogeneous plasma, i.e., $n_0 = n_0(x)$, with finite pressure gradient transverse to the magnetic fields can develop 'drift waves' so called because the waves propagate in the direction of the electron diamagnetic velocity, $V_{de} = -\dfrac{mkT}{eBL_n}$[16]. The quantity $1/L_n = \dfrac{d \ln n_0(x)}{dx}$ is the scale length of the equilibrium density gradient $dn_0(x)/dx$. The theoretical properties of linear drift waves are well understood and are discussed in a review paper [17]. The simplest nonlinear model[18] for the drift-wave is found by expanding Eqn.1.8 to the second order in ω/Ω_{ci}, where, $\Omega_{ci} = eB/M_i$ is the ion gyrofrequency. Thus the ion velocity can be presented as the sum of the $\vec{E} \times \vec{B}$ and polarization drift,

$$\vec{u} = -\vec{\nabla}\phi \times \frac{\vec{B}}{B_0^2} + \frac{1}{\Omega_{ci}B_0}\left[-\frac{\partial}{\partial t}\vec{\nabla}_\perp\phi - (\vec{u}_E \cdot \vec{\nabla}_\perp)\vec{\nabla}_\perp\phi\right] \tag{1.9}$$

where, $\vec{u}_E = -\vec{\nabla}\phi \times \dfrac{\vec{B}}{B_0^2}$ is the $\vec{E} \times \vec{B}$ drift and $-\vec{\nabla}\phi$ is the electric field $\vec{E}$. The term in the square brackets is the polarization drift. When $\vec{R}_e = 0$ (i.e., when the electrons do not suffer collisions), the continuity equation Eqn.1.7 can then be used to find a nonlinear equation which describes the evolution of the perturbed potential,

$$\frac{\partial}{\partial t}(\phi - \vec{\nabla}_{\perp}^2 \phi) - \left[(\vec{\nabla}_{\perp}\phi \times \hat{z}) \cdot \vec{\nabla}_{\perp}\right] \vec{\nabla}_{\perp}^2 \phi + \frac{1}{L_n}\frac{\partial}{\partial y}\phi = 0 \tag{1.10}$$

Eqn.1.10 is known as the Hasegawa-Mima equation, or HM equation[18]. In this equation the potential is normalized with T_e/e, the time with the $1/\Omega_{ci}$, and distance with $\rho_s(\rho_s = c_s/\Omega_{ci}$ is the ion gyroradius evaluated at the sound speed c_s, where $c_s = \sqrt{T_e/M_i}$). To get this model several simplifying physical assumptions have been made: (1)Homogeneous background magnetic field, i.e., $\vec{B} = B_0\hat{z}$; (2) Cold ions (ion thermal balance equation dropped) and $T_i \ll T_e$; (3)Adiabatic electrons and quasineutrality, i.e., $n_i \approx n_e \approx n_0(x)\exp(\frac{e\phi}{T_e})$ (Boltzmann relation); (4)The polarization drift (the term in the square brackets in Eqn.1.9) is small compared to the primary $\vec{E} \times \vec{B}$ drift. Note that the key nonlinearity here is the $\vec{E} \times \vec{B}$ advection of the ion polarization drift. The HM model is similar to the 2D incompressible neutral fluid except two differences: (1) The background gradient appears in the HM model, and (2) the time derivative , $\frac{\partial \phi}{\partial t}$, appears in the HM model. The HM model behaves like a 2D incompressible fluid in the limit that $\phi/\vec{\nabla}_{\perp}^2\phi \to 0$ or $k\rho_s \gg 1$, i.e., wavelength is much smaller than ρ_s.

With a plane wave solution of the potential, $\phi = \phi_k \exp(i\vec{k}\cdot\vec{r} - i\omega t)$, a dispersion relation of the drift wave can be presented as $\omega_\star = \frac{k_\theta V_{de}}{1 + k_\perp^2}$. Note that in this description the drift-wave is marginally stable ($\omega_\star$ is purely real). This is illustrated with the Fig.1.3. When there is no parallel electron resistivity dissipation, i.e., $\vec{R}_e \cdot \frac{\vec{B}}{|B|} = 0$, the pressure gradient is balanced by the electric field, thus the density and potential satisfy Boltzmann relation, $\frac{\tilde{n}}{n} = \frac{e\tilde{\phi}}{kT_e}$ $(\frac{e\tilde{\phi}}{kT_e} \ll 1)$ for an isothermal plasma. As a result where the density is

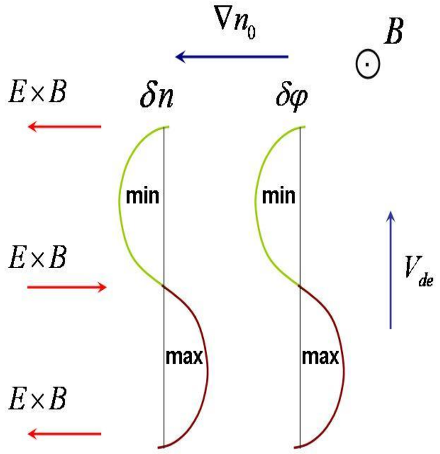

Figure 1.3: Physical mechanism of a drift wave.

positive, the potential is positive. The resulting $\vec{E}\times\vec{B}$ velocity bring plasma from different density to a fixed point. The net effect is to propagate the drift wave azimuthally in the direction of the electron diamagnetic velocity V_{de}. Density and potential perturbation are in phase and the system is stable. The HM model was useful to study evolution of spectrum without dissipation. However, this idealized model does not apply to most experimental conditions where $\vec{R}_e \neq 0$, such as ours.

The Hasegawa-Wakatani model(HW), which is derived from the same equations (Eqn.1.7 and Eqn.1.8) but includes the electron parallel dissipation, electron-ion collisions and ion viscosity, describes the dynamics of the drift turbulence in the presence of electron and ion dissipation. The governing equations are two coupled dimensionless equations as

$$(\frac{\partial}{\partial t} - \vec{\nabla}\phi \times \hat{z} \cdot \vec{\nabla})\vec{\nabla}_{\perp}^{2}\phi = c_1(\phi - n) + c_2\vec{\nabla}_{\perp}^{4}\phi \tag{1.11}$$

$$(\frac{\partial}{\partial t} - \vec{\nabla}\phi \times \hat{z} \cdot \vec{\nabla})(n + \ln n_0) = c_1(\phi - n) \tag{1.12}$$

where, $c_1 = k_\|^2 V_{the}^2/\nu_e \Omega_{ci}$, the so-called 'adiabatic parameter'. Here $k_\|$ is the parallel wavenumber, V_{the} the electron thermal velocity and ν_e the electron collision frequency. $c_2 = \mu/\rho_s^2\Omega_{ci}$, is the normalized ion viscosity.

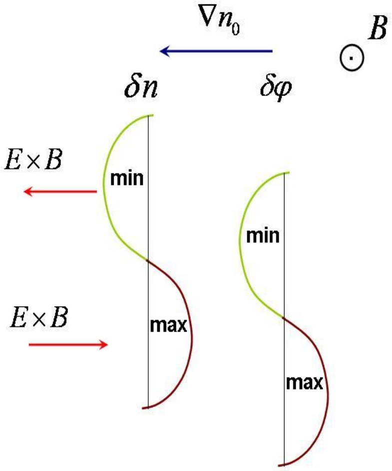

Figure 1.4: Physical mechanism of a drift wave.

In the HW model (Eqn.1.11 and Eqn.1.12) there are three dimensionless parameters determining the nonlinear dynamics of the drift wave turbulence: (1) the normalized the density scale length ρ_s/L_n, (2) the 'adiabatic parameter', c_1, and (3) the normalized ion viscosity c_2. In the presence of the neutral collisions the dimensionless ion-neutral collision frequency ν_{in} is also relevant, and should be much less than 1. The parameter c_1 quantifies the degree to which the Boltzmann relation is maintained via parallel electron dynamics. For $c_1 \gg 1$, parallel collisions are negligible. This is the HM model. For $c_1 \approx 1$, the Boltzmann relation breaks down and density and potential fluctuations become particially de-correlated and also acquire a finite phase shift. For $c_1 \ll 1$, density acts as a passive scalar following streamlines of the potential. This is in the hydrodynamic limit. The dynamics of this extreme are as the 2D Euler fluid. The typical drift-wave perpendicular spatial scale is ρ_s and the time scale is $\omega_\star \ll \Omega_{ci}$. Drift turbulence occurs typically when $\rho_s/L_n \ll 1$ and $c_2 \ll 1$, which then allow the convective derivative term to become important in the momentum equation Eqn.1.8. In our experiments these conditions are satisfied with $c_1 \approx 1$, $\rho_s/L_n \approx 0.3 - 0.5, c_2 \approx 0.2 - 0.3$ and $\nu_{in} \approx 0.01$. In the presence of finite electron dissipations (i.e., $c_1 \sim 1$), the electrons can not respond quickly to a perturbation in the plasma potential. Consequently, there is finite phase shift between density and potential. As a result of this phase shrift, the $\vec{E} \times \vec{B}$ velocity reinforces the density perturbation and the system becomes unstable as ρ_s/L_n is decreased. This is illustrated in the Fig.1.4. Typically fluctuations with $0.1 \le k_\theta \rho_s \le 1$ become linearly unstable, with $\frac{\omega_R}{2\pi} \approx \frac{\omega_\star}{2\pi} \sim 10 - 100$kHz and with $\frac{\omega_I}{\omega_R} \sim 0.01 - 0.1$. A detailed discussion of the transition to a state of drift turbulence in CSDX deviece has been given previously[19].

1.3 Zonal flow generation in drift-wave turbulence

Turbulence in fluids is generally three-dimensional. However, under certain circumstances the vorticity of the motion is ordered along a particular axis. In such case the turbulence can be reasonably described as two-dimensional. Examples of this include a thin accretion disk of materials orbiting a central object like a star, or in a thin-atmosphere system with some rotation like geophysical turbulence, or the magnetized plasma[20].

A key difference between 2D and 3D turbulence is that in 3D turbulence there exists a finite strain field $\frac{\partial v_z}{\partial z} \neq 0$ which causes vortex tube stretching (here z is aligned with the vortex axis). This allows both enstrophy and energy transfer to small spatial scales where energy is dissipated by viscosity in a process referred as a direct energy cascade[21]. However, in 2D turbulence the strain field vanishes, i.e., $\frac{\partial v_z}{\partial z} = 0$, so the vortex stretching does not occur. This leads to a dual cascade of energy and enstrophy[22] wherein the kinetic energy is transfered to the largest scales and enstrophy is transfered to the smallest scales. Both enstrophy and kinetic energy are conserved in such process. This process can be illustrated by two colliding vortices: When two like sign vortices approach together they will merge together to form a single vortex, which due to conservation of momentum and energy must be larger in size. This process can be repeated and resulting in a formation of progressively larger-scaled structure. Eventually a large-scale coherent structure will be formed [23, 24].

In toroidal plasma zonal flows, by definition, are poloidally and toroidally symmetric electric field perturbation, which are constant on the magnetic surface but rapidly varies in the radial direction ($k_\theta = k_\varphi = 0$, finite k_r, with k_θ, k_φ and k_r denoting the poloidal, toroidal and radial wavenumber respectively). Fig.1.5a [8] is a schematic of a zonal flow. Because the variation of the electric field perturbation is in the radial direction, the associated $\vec{E} \times \vec{B}$ flow is in the poloidal direction and changes sign with radius. Zonal flows are predicted to be linearly stable and are thought to be generated by a nonlinear transfer of kinetic energy from the turbulence at $\vec{k}_1$ and $\vec{k}_2$ to large-scaled shear flows with $\vec{k}_{ZF}$ mediated by three wave coupling process satisfying criteria $\vec{k}_1 + \vec{k}_2 = \vec{k}_{ZF}$, where

$\vec{k}_1$,$\vec{k}_2$ are turbulent fluctuation wavenumbers and $\vec{k}_{ZF}$ is zonal flow wave number [21]. To illustrate this process, consider a highly simplified model of azimuthal momentum balance for an incompressible inviscid two-dimensional plasma fluid with azimuthal flow u_θ in a cylindrical plasma in the presence of a flow damping rate μ [25] as,

$$\frac{\partial u_\theta}{\partial t} + \frac{\partial u_\theta u_r}{\partial r} = -\mu u_\theta \tag{1.13}$$

where $u_r u_\theta$ is Reynolds stress and μ is damping rate of the mean flow due to dissipative processes. Taking a spatial Fourier transform of this equation gives,

$$\frac{\partial u_\theta(\vec{k})}{\partial t} + ik_r \sum_{\vec{k}_1,\vec{k}_2,\vec{k}=\vec{k}_1+\vec{k}_2} u_\theta(\vec{k}_1)u_r(\vec{k}_2) = -\mu u_\theta(\vec{k}) \tag{1.14}$$

where $u_i(\vec{k})$ is the ith component of the transformed velocity u at wavenumber $\vec{k}$. Multiplying this equation by the complex conjugate $u_\theta^\star(\vec{k})$ results in a new equation. Taking the complex conjugate of this new result and adding these two equations together give the evolution of the kinetic energy of the flow $u_\theta^2(\vec{k})$ as,

$$\frac{\partial \left| u_\theta(\vec{k}) \right|^2}{\partial t} - 2k_r \sum_{\vec{k}_1,\vec{k}_2,\vec{k}=\vec{k}_1+\vec{k}_2} Im \left[u_\theta^\star(\vec{k}) u_\theta(\vec{k}_1) u_r(\vec{k}_2) \right] = -\mu \left| u_\theta(\vec{k}) \right|^2 \tag{1.15}$$

The 2nd term of the LHS of this equation represents the nonlinear transfer of kinetic energy in k space across spatial scales via 3-wave coupling. Consider a zonal flow to have $\vec{k}_{ZF} = k_r^{ZF}\hat{r}$, and generally it is assumed to have $|\vec{k}_1|$, $|\vec{k}_2| \gg |k_r^{ZF}|$. This assumption implies that the wavevectors of the interacting triplets $\left\{\vec{k}_1, \vec{k}_2, k_r^{ZF}\right\}$ form 'narrow' triangles such as those shown in Fig.1.5b, rather than equilateral triangles in the 2D neutral fluid turbulence, where the magnitudes $\left\{\vec{k}_1, \vec{k}_2, \vec{k}_{ZF}\right\}$ are all comparable[21].

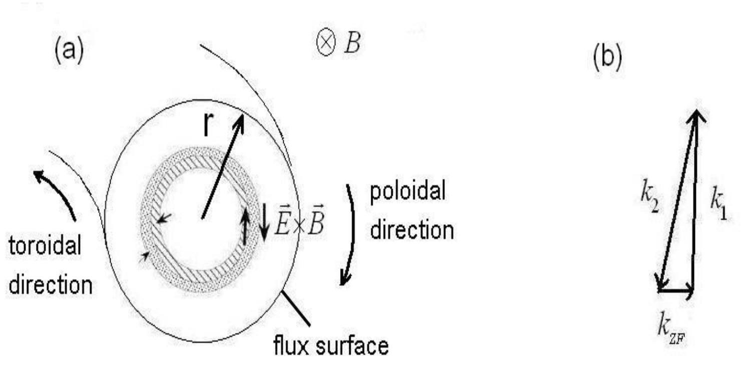

Figure 1.5: (a) Schematic of zonal electric field. The poloidal cross section of toroidal plasma is illustrated. The hatched region and the dotted region denote the positive and negative charges respectively[8]. (b) Schematics of zonal flow-drift wave interaction for zonal flow with a wavevector k_{ZF} and two drift wave vectors k_1 and k_2.

For low beta plasma with significant plasma fluctuation amplitude for $k\rho_s \ll 1$, the fluid velocity can be taken to be electrostatic $\vec{E} \times \vec{B}$ drift velocity, i.e., $u(\vec{k}) = -(ik\phi(\vec{k}) \times B)/B^2$, where $\phi(\vec{k})$ is the Fourier transformed electrostatic potential. Then averaging Eqn.1.15 over zonal flow scales we can write in from of $\phi(\vec{k}_{ZF})$,

$$\frac{\partial \left|\phi(\vec{k}_{ZF})\right|^2}{\partial t} = 2\gamma(\vec{k}_{ZF}) \left|\phi(\vec{k}_{ZF})\right|^2 + Re \sum_{\vec{k}_1,\vec{k}_2} T_k(\vec{k}_1, \vec{k}_2) \left\langle \phi^\star(\vec{k}_{ZF})\phi(\vec{k}_1)\phi(\vec{k}_2)\right\rangle \quad (1.16)$$

where $T_k(\vec{k}_1, \vec{k}_2)$ is a quadratically nonlinear wave-wave coupling coefficient. This equation simply says that the fluctuation energy contained in the k_{ZF} component is formed by a balance of the linear growth(damping) rate of this mode with the energy transfered away (into) this mode.

The simulations by Hasegawa and Wakatani [26] have shown the condensation of the kinetic energy into large-scaled shear flow. Fig.1.6 is an example of these results. The most conspicuous feature of the potential contours is the formation of the closed potential surface with $\phi(r) \approx 0$ as shown in Fig.1.6b. This is due to the generation of poloidal and toroidal symmetric potential through inverse cascade of turbulent spectra [26].

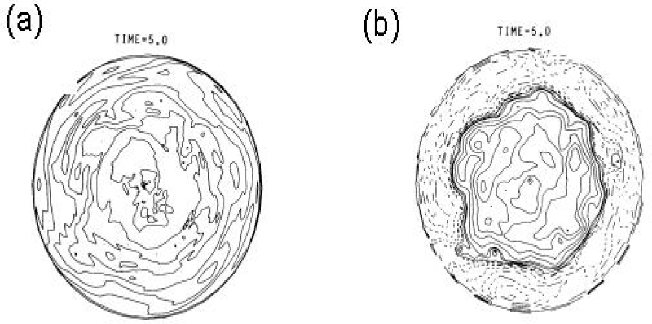

Figure 1.6: (a) The density contour. (b) The potential contour from the 3D computer simulation of electrostatic plasma turbulence in a cylindrical plasma with magnetic curvature and shear. In (b) the solid (dashed) lines are for the positive (negative) potential contours. Note the development of closed potential contour near the $\phi \approx 0$ surface[26].

The significance of the generation of zonal flows is that they can regulate turbulence and transport, which is the key element that drives the strong current interest in zonal flow. In the case of a smooth, mean shear flow, the shearing tilts turbulent eddies, narrowing the radial extent and elongating them, as illustrated in Fig.1.7(a,b)[8]. Some simulations show the sheared flow can break up turbulent eddies. This implies that the radial wavenumber increases with time. The increase in k_r implies reductions of the effective 'step size' Δl in the turbulent diffusivity $\chi_{turb} \approx \Delta l^2/\tau_{corr}$ [27], thus reduces turbulent transport and increases energy confinement time. In addition, the transfer of energy between the turbulence and ZF conserves total energy. Thus an increase in the ZF comes at the expense of the drift turbulence energy, and thus reduces χ. A recent review article [8] gives a detailed summary of this process. Zonal flows and drift-wave turbulence are thus in a self-organization system. As the theory of zonal flow generation and their roles in regulating plasma turbulence and associated transport are now well developed, detailed experimental tests of theory are now needed.

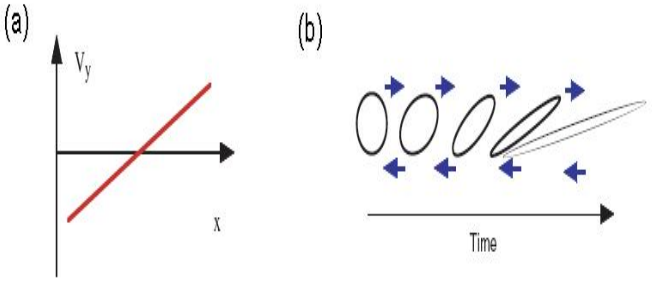

Figure 1.7: (a) Sheared mean flow. (b) Shearing of the vortex. Picture taken from Ref.[8]

1.4 Previous relevant plasma turbulence experiments

To investigate the drift-wave turbulence/zonal flow theoretical dynamical behavior measurements of the plasma density and electrostatic potential have to be made. Such measurements are realized by using the Langmuir probe,by heavy ion beam probe (HIBP), or by measuring spatial propagation of fluctuation immersed in a ZF. Because of the high plasma density and temperature near the core region of the plasma, Langmuir probe measurements are limited to the edge region. Observation of the ZF requires the capability of either measuring the radial electric field (from probes or HIBP) or the plasma velocity fields directly. With such experimental techniques the structure of the plasma profiles in the plasma boundary region has been investigated in tokamak, stellarator and reversed field pinch, demonstrating an onset of the improved confinement, associated with the existence of the shear flow. Fig.1.8 shows the examples of frequency spectra in CHS, T-10, TEXT, JFT-2M, ASDEX-U and DIIID. The picture is taken from Ref.[30]. The common feature of the spectra is the existence of the solitary peaks, which have been identified as the finite frequency sheared ZF known as the GAM. The Hinton-Rosenbluth branch of the ZF was observed in CHS using twin heavy-ion-beam-probe (HIBP) located at two different toroidal positions separated by 90^o[31] as shown in Fig.1.9. In Fig.1.9a the power spectrum of the electric field (red lines) and the coherence between the electric fields at two different toroidal locations show that the $0.3 - 1$kHz electric field fluctuations have long-range correlations, suggesting the activity of zonal flow of nearly zero frequency. This is also clearly shown in Fig.1.9b with blue lines showing a high coherence between electric fields at different toroidal locations and red lines showing the zero phase (divided by π) between these two.

As the existence of the ZF is an unambiguous phenomenon in many magnetic confinement devices, attentions have turned to understand the mechanisms that drive the

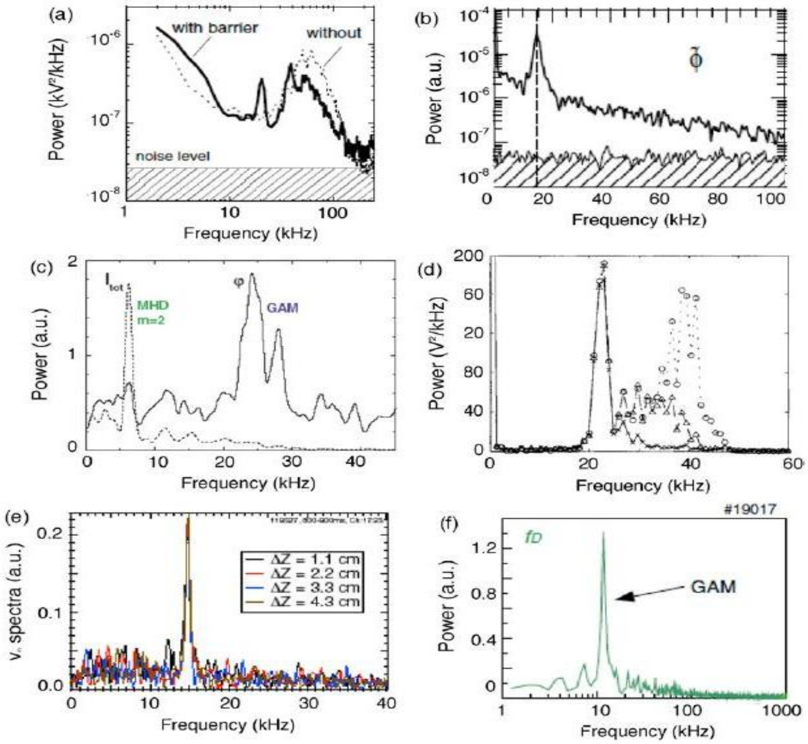

Figure 1.8: Potential fluctuation spectra measured with HIBP. (a) Electric field fluctuation in CHS[32]. (b) Potential fluctuation spectra in JFT-2M. The hatched area means the noise level[33]. (c) Potential and density fluctuation spectra in T-10[34]. (d) Potential fluctuation spectra in TEXT-U for three different locations. The crosses, diamonds and circles correspond to $\rho = 0.85$, $\rho = 0.76$ and $\rho = 0.69$, respectively [35]. (e) Velocity fluctuation spectra measured with BES in DIII-D[36]. (f) Spectrum of Doppler frequency measured with DR in ASDEX-U[37]. Picture taken from Ref.[30]

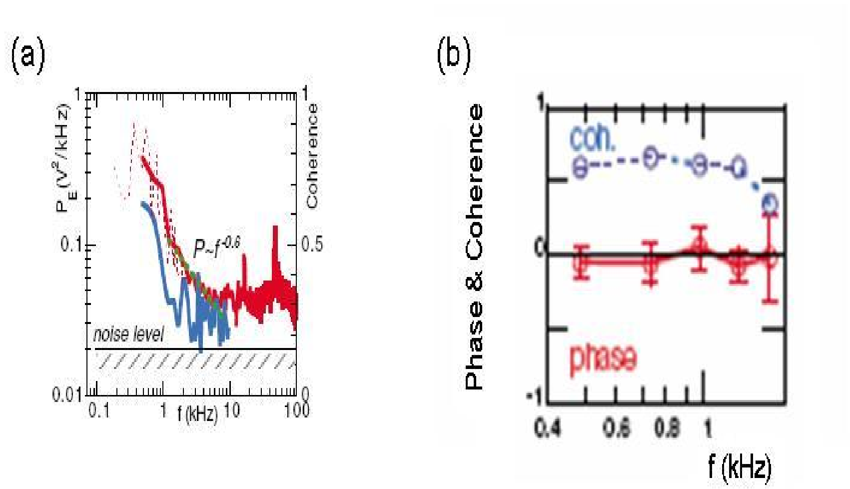

Figure 1.9: (a) Power spectra of potential difference (red lines), and coherence between potential differences (blue line) at the two toroidal locations. The hatched region shows the noise level for power. (b) An example of phase (divided by π) and coherence between potential differences at two toroidal locations on a magnetic flux surface. Picture taken from Ref.[31]

sheared flow. In a few experiments it has been suggested that turbulent Reynolds stress is the mechanism generating the shear flow. A preliminary investigation was done in the TJ-IU torsatron and ISTTOK tokamak. In those experiments a radial profile of the Reynolds stress has been measured in the plasma boundary region[38] and shows a radial gradient close to the velocity shear layer location. This stress gradient is estimated to be in the range of $10^7 - 10^8 m/s^{-2}$. The damping term was estimated to be $\gamma_{mp} v_{i\theta}$, where $v_{i\theta}$ is the ion poloidal velocity assuming to be close to the phase velocity of the fluctuations (about $1 km/s$). For the typical edge plasma condition, the flow damping rate is estimated as $\gamma_{mp} \approx 10^4 s^{-1}$. Thus the radial gradient of Reynolds stress is large enough to possibly drive significant poloidal flows in the plasma boundary region. In HT-

6M tokamak[39] the Reynolds stress is also measured and used with measurements of a plasma flow ti evaluate the mechanism leading to an H mode transition. The results show a clear correlation between the enhanced Reynolds stress gradient and the poloidal flow acceleration, suggesting the turbulence-induced Reynolds stress might be the dominant mechanism to create the poloidal flow and E_r shear. More recently in CHS a wavelet analysis reveals that there is a correlation between disparate-scale components of electric field fluctuations[32]. It is found that the wavelet power of the lower frequency $(2.5 < f < 10kHz)$ close to the stationary zonal flow is anti-correlated with the power of the turbulence $(30 < f < 250kHz)$. There are also a few experiments demonstrating the effect of zonal flows on plasma transport and confinement. In CHS by using HIBPs it is found that the particle transport is modulated by the zonal flow[40], as shown in Fig.1.10. It clear shows difference in the fluctuation spectrum according to the zonal flow phase.

The experiments carried out on various magnetic confinement devices, using many diagnostic techniques, have confirmed that the zonal flows really do exist in toroidal plasmas and the available data suggest that the ZF/turbulence interactions are consistent with the theoretical models. However, there are still many issues unaddressed. One question is how the turbulent statistical properties (e.g. turbulence amplitudes, cross phases and cross coherency) lead to the development of the detailed Reynolds stress profile that in turn drives the shear flow. So far, to our knowledge only the mean Reynolds stress profile and its link to the shear flow generation have been examined. Furthermore, there have been no detailed experimental studies of the link between the turbulent Reynolds stress, background shear flow and formation of bursty or intermittent transport events. Another

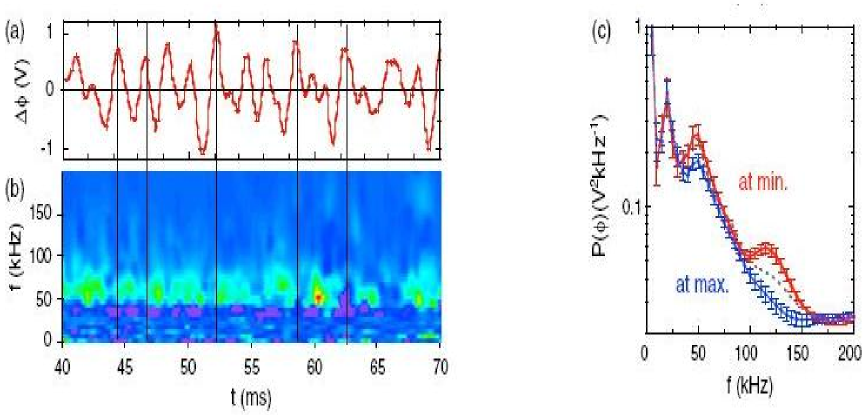

Figure 1.10: The modulation effect of stationary zonal flow on particle transport in CHS[40]. (a) Temporal evolution of stationary zonal flows and (b) an image plot of particle flux. (c) Conditional averages of potential fluctuation spectra in the time windows discriminated by the phase of zonal flow; i.e. maxima, zero and minima. Picture taken from Ref.[30]

issue is there has been no full experimental validation of theoretical picture of the drift wave turbulence/zonal flow self-organization dynamic system in a single experiment-the existing observations are made across multiple experiments operating in widely varying conditions.

A full experimental demonstrations needs several observations to be made in one experimental plasma device. Firstly, an existence of the shear flow with correct symmetric properties must be demonstrated. Secondly, such shear flow has to be demonstrated to be generated against damping mechanisms by the turbulent Reynolds stress. Thirdly, the shearing effect of the resulting shear flow on the turbulence including a reduction of the turbulence radial correlation length should be observed. Fourthly, there must be an anti-correlation between the turbulence energy and the flow energy consistent with a conservation of total energy. No such complete set of observation presently exists. Studies of this issue will have a great significance to further understand the shear flow generation mechanism and fill the gap between the theories and the experiments.

1.5 Previous experimental results on CSDX

To study the interaction between drift-wave turbulence and shear flow it is clear that firstly, a detail transition to drift turbulence should first be demonstrated. Such studies need have a known source of free energy, an identifiable initial instability, and a known source of dissipation. And the system should undergo a transition to turbulence so that the final turbulent state could be compared with theory. In previous work this transition has been demonstrated by increasing the value of the magnetic field[19], which decreases ρ_s and increases the dimensionless parameter L_n/ρ_s, which determines the strength of the convective derivative in the HW model(and this is analogous to increase the R_e number in a neutral fluid experiments). It is found when the magnetic field, B, is increased from 300G to 1kG the floating potential changes from discrete mode consistent with linear drift wave eigenmode to broadband turbulence (See Fig.1.11). During this transition the fluctuation energy at low poloidal wavenumbers, which are linearly stable, are found sharply increase as a turbulent state is realized with the increase of the magnetic field, which suggests that the turbulence energy is nonlinear transfered from turbulence into large azimuthal scale fluctuation, as shown in Fig.1.12. Simulations of the collisional drift turbulence using the HW model in our plasma device have also clearly shown the formation of the shear flow qualitatively similar to those observed in the experiments[42], as shown in Fig.1.13,which illustrate that the dynamics of the system are dominated by the $m = 3$ mode and the zonal flow.

With the Langmuir probe measurements an azimuthally symmetric radially sheared plasma flow has been demonstrated. A turbulent momentum conservation analysis has shown this shear flow is sustained against dissipation by the turbulent Reynolds stress generated by collisional drift fluctuations in the device. The time-averaged azimuthal component of the ion momentum equation is shown in Eqn.1.17 as,

$$\frac{1}{r^2}\frac{\partial}{\partial r}(r^2\left\langle \tilde{v}_r\tilde{v}_\theta\right\rangle) = -\nu_{in}\left\langle v_\theta\right\rangle + \mu_{ii}(\frac{\partial^2\left\langle v_\theta\right\rangle}{\partial r^2} + \frac{1}{r}\frac{\partial\left\langle v_\theta\right\rangle}{\partial r} - \frac{\left\langle v_\theta\right\rangle}{r^2}) \qquad (1.17)$$

where $\tilde{v}_r\tilde{v}_\theta$ is Reynolds stress, ν_{in} is ion-neutral collisional rate and μ_{ii} is ion-ion viscos-

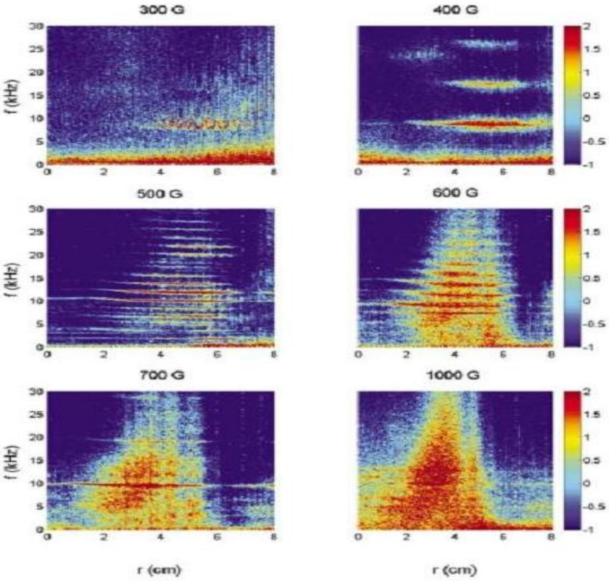

Figure 1.11: Radial profiles of potential fluctuation power spectrum with increasing B field[19]

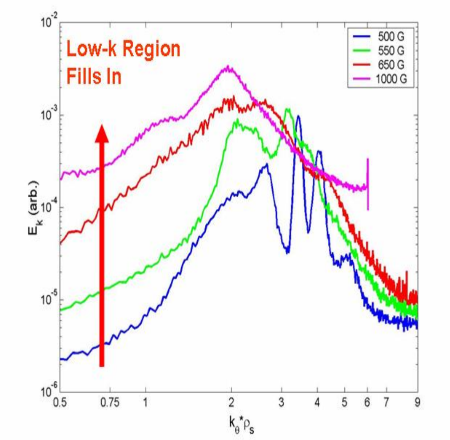

Figure 1.12: Development of the azimuthal energy wave-number spectrum $E(k_\theta)$ with increasing B. Data are from $r \sim 3$ cm. Arrows indicate a trend toward larger scales as turbulence develops. The apparent compression of the abscissa is due to the normalization by ρ_s[19].

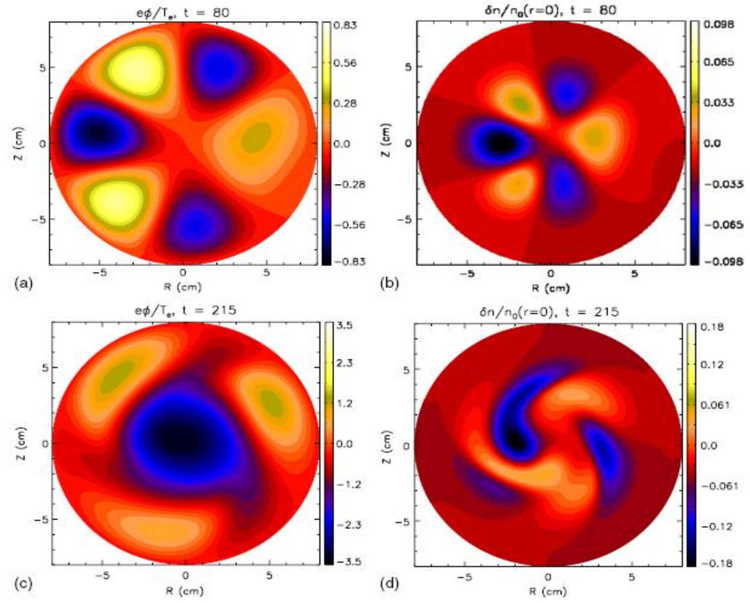

Figure 1.13: Snapshots of the potential density during the linear ($t = 80$) and nonlinear ($t = 210$) phases of the limit cycle case[42].

ity. A detailed derivation of Eqn.1.17 can be found in Ref.[41]. The turbulent Reynolds stress was measured by a four-tip Langmuir probe. Taking the measured Reynolds stress into Eqn.1.17 the mean azimuthal flow can be solved with reasonably assumed viscosity and neutral damping rate profile, as shown by the black solid line in Fig.1.14. The mean azimuthal velocity was also measured directly by applying TDE technique to azimuthally separated probe tips measuring floating potential, shown as open diamond in Fig.1.14. Both show a shear flow existing in the plasma with a peak flow shear located approximately at $r = 3.6$cm. The good agreement of these two velocities demonstrated the shear flow generation by the turbulent Reynolds stress against collisional and viscous damping.

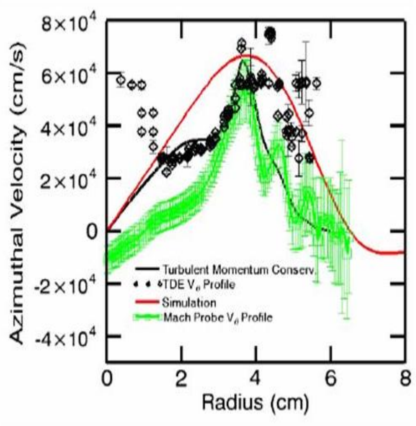

Figure 1.14: Radial profile of azimuthal velocity field measured from different methods[41].

1.6 The aim of this dissertation

The aim of this dissertation is to undertake novel studies of drift-wave turbulence/zonal flow self-organization system to understand, from an experimental point of view, how sheared ZFs can arise from plasma turbulence, and affect the turbulence-driven transport. Based on the limitations of the existing experimental results and our previous work on CSDX we perform this study through three primary avenues: The first is to directly investigate the statistical properties (e.g. turbulence amplitude, cross phase, and cross coherence) of the mean turbulent Reynolds stresses, radial turbulent particle transport and the plasma density fluctuations, from which to understand the process of the drift-wave turbulence driven shear flow generation. The analysis methods include computing the probability distribution function (PDF) of both turbulent Reynolds stresses and plasma density fluctuations, joint PDF between different components of the velocity fields and the spectrum of the turbulent Reynolds stresses. Since the turbulent Reynolds stresses play an important role in the shear flow generation, investigating the statistical properties will help to further understand the shear flow generation mechanism. The simple geometry of the linear cylindrical plasma device and the low plasma temperature ($3eV$) make it possible to directly measure turbulent stresses by Langmuir probe and thus provide an opportunity to give such detailed studies. Through this study two questions could be answered: One is what statistical properties lead to the development of the detailed Reynolds stress and associated shear flow generation. The other is what is the relationship, if any, among turbulent Reynolds stress, particle flux and background shear flow. To our knowledge, these questions have not been answered prior to this study. In Chapter 3 we describe these results in details.

The second avenue of study has been an investigation of the dynamical coupling between the drift-wave turbulence and shear flow using a combination of Langmuir probe measurements and fast-framing imaging techniques. Theory predicts that the shear flow and turbulence are in a self-organization dynamical system. An experimental test of this requires several observations to be made in one plasma apparatus as wee described in section 1.4. The goal of this study is to provide an experimental investigation of all requirements, which are necessary for the validation of the theoretical picture of the drift-wave turbulence/shear flow self-organization dynamical system. To our knowledge this is the first time to provide such fully experimental investigations in one plasma apparatus. In Chapter 4 we report such analysis in details.

The third avenue is to investigate the scaling properties of the drift-wave turbulence driven shear flow. Previous work has shown that the magnetic field is an effective parameter to control the transition to turbulence[19]. In addition, another parameter, plasma pressure, is also reported to be a possible way to control the transition to turbulence[43, 44]. Therefore it would be very interesting to investigate the evolution of the shear flow with these parameters. In the large scale magnetic confinement plasma device experiments are mostly performed when the plasma is already in 'turbulent' state. Therefore there is no way to study the shear flow evolution with those parameters during the transition to turbulence. Our small scale linear machine, which has been clearly shown an existence of the transition to turbulence process, however, provides such an opportunity for this study. In Chapter 5 we report the results of this study.

This thesis is organized as follows: In chapter 2 we describe the basic experimental setup, hardware arrangements and summarize the various analysis methods we use for this study. In chapter 3 the results of the statistical properties of the turbulent Reynolds stress are extensively discussed. In chapter 4 we discuss the results of the dynamical coupling between drift-wave turbulence and shear flow using a combination of probe based measurements and fast-framing camera. In chapter 5 we exam the variation of the shear layer and turbulence as magnetic field and neutral gas damping are varied. Lastly in chapter 6 we summarize our results and suggest several measurements for future studies.

2

Experimental set up and methods of analysis

In this chapter we will describe the basic mechanical and electrical hardware used in our experiments, and give an overview of the various methods utilized for our data analysis.

2.1 CSDX linear plasma machine

The (C)ontrolled (S)hear (D)ecorrelation E(x)periment (CSDX) is a cylindrical linear plasma device. The overall length is about 2.8m and the vacuum vessel diameter is 0.2m. Fig.2.1 provides a picture of the machine. This device is operated with a 13.56MHz 1500W RF helicon wave source via an antenna surrounding a 10cm diameter, 45cm length glass belljar. A matching circuit is adjusted such that less than 30W of power is reflected. A more detailed description of the RF source characteristics can be found in the Ref.[45].

Both source and vacuum chamber are surrounded by a set of disk-shaped electromagnet coils, providing a solenoidal magnetic field that can be varied from 0 up to 1kG. Each of these coils has an inner diameter of 28cm and outer diameter of 91cm. Each coil has a center-to-center axial core separation of 12cm. All of the magnetic field lines exiting the two ends of the device terminate on insulating surfaces to eliminate the possibility of currents flowing through the end plates of the device. Thus any fluctuating axial currents due to drift waves must be balanced by fluctuating cross-field currents carried by ion polarization drifts (which are equivalent to the turbulent Reynolds stress[46]). An axial fall-off of the solenoidal magnetic field intensity is only appreciable at the end of the vessel (40%), but is negligible at the center part of the chamber where all the experimental data in this thesis are taken. A roughing pump located at the end of the machine is used to maintain a low base pressure. Further pumping is provided by a $1000 liter/sec$ turbo pump. A calibrated mass flow controller provides gas injection and the plasma pressure is measured by a Baratron gauge located at the end of the machine.

2.2 Plasma diagnostics

2.2.1 Multi-tip Langmuir probe

Measurements of mean plasma profiles, the fluctuating density, potential, and electric fields along with the resulting turbulent Reynolds stress are made by an 18-tip Langmuir probe inserted radially in a port located 1.7 meter downstream from the source. Fig.2.2 is a schematic and a picture of the 18-tip probe. The probe array is arranged as

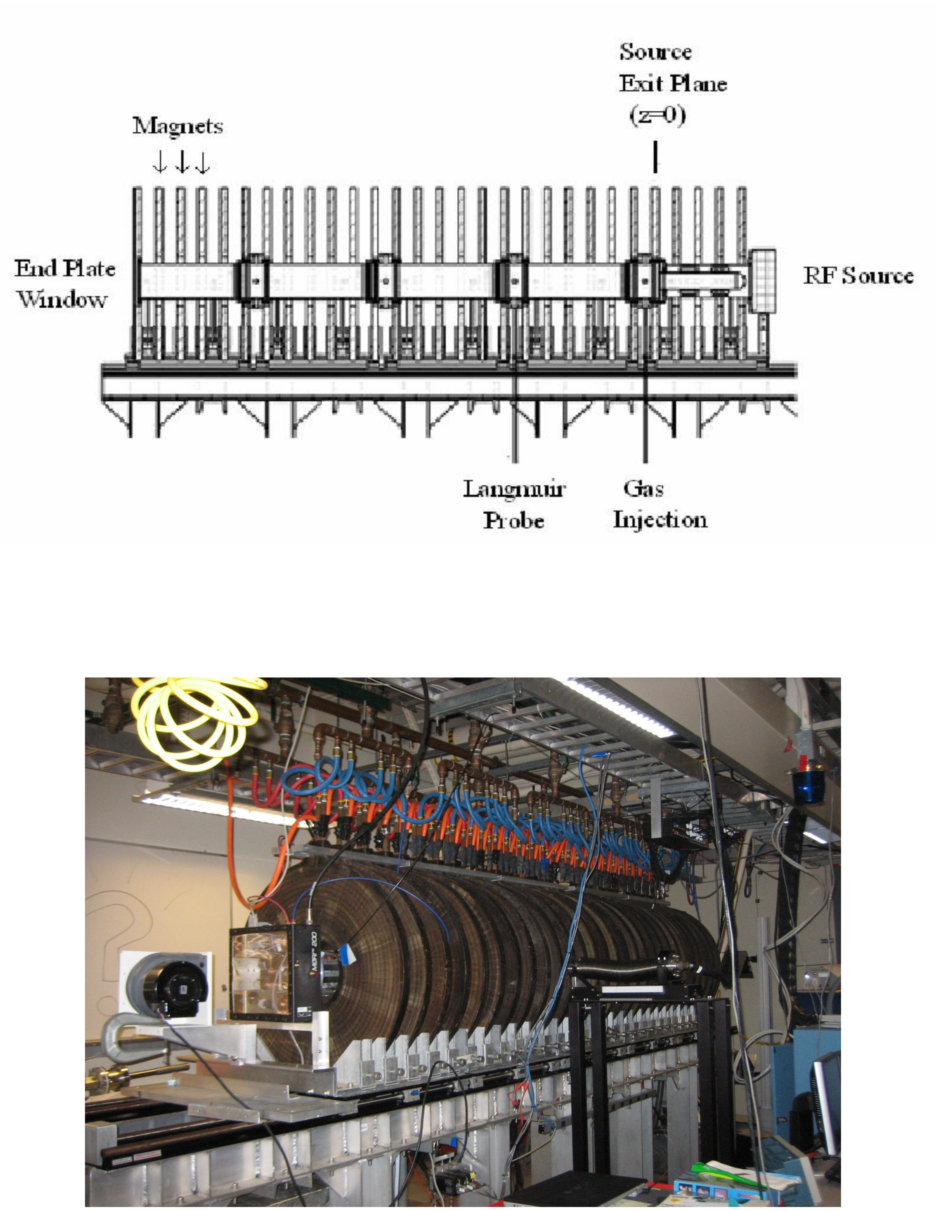

Figure 2.1: A schematic (top) and a picture (bottom) of CSDX

two 3×3 arrays are shifted along the magnetic field by 1.5mm. One array measures ion saturation current with probe tips biased at -25V dc voltage, and the other array measures floating potential with probe tips connecting to $100k\Omega$ resistor. The electrical circuit is shown in Fig.2.3. The radial displacement of the probe tips is 1.5mm and the azimuthal displacement is 2.5mm. Each tungsten tip is 0.33mm in diameter and 1mm in length. Each tip is inserted in a single ceramic tube with a diameter only 1.2mm. The arrangements of the probe tips in both radial and azimuthal directions allow the measurements of the electric field from floating potential. Here it is assumed that the electron temperature fluctuations are negligible. Thus from the relation $\phi_p \cong \phi + \chi T_e$ [48] (with $\chi \cong 5.1$ for argon in our data), where ϕ_p is plasma potential and ϕ is floating potential, fluctuating plasma potential is approximately equal to the fluctuating floating potential, i.e., $\tilde{\phi}_p \approx \tilde{\phi}$. The electric field can be obtained by $\vec{E} = -\vec{\nabla}\phi$. Besides, such arrangements of the probe tips allow the measurements of the radial and azimuthal electric field at the same location (ϕ_6 and ϕ_4 are used to compute E_θ, and ϕ_8 and ϕ_2 are used to compute E_r). Thus at later time when analyzing the cross-phase between different components of the velocity fields there is no spurious phase difference since the measurements are made at the same spatial location.

2.2.2 Data acquisition system

Fig.2.3 is the circuit schematic of the density and potential measurements from the Langmuir probe described above. For the density measurements the voltage across the 50Ω resistor passes through a AC coupled amplifier, which has 50Ω input impedance and

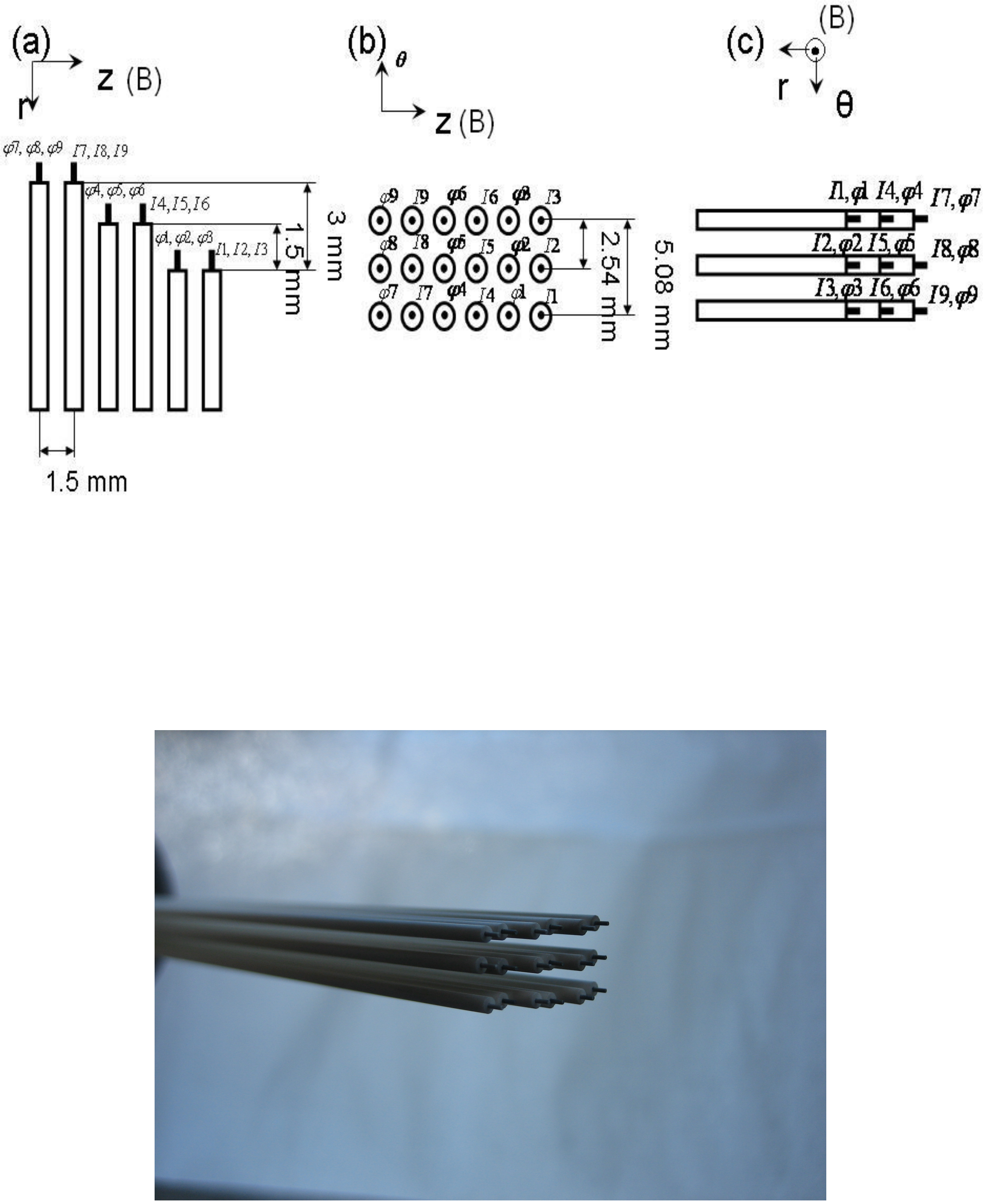

Figure 2.2: A schematic (top) and a picture (bottom) of the 18-tip probe

1MHz band width, and is recorded by a 16 bit 96 channel digitizer with 500kHz sampling rate (D-TACQ ACQ196CPCI). The resulting Nyquist frequency is 250kHz well above the electrostatic fluctuation frequency. For equilibrium density measurements the voltage across the 50Ω resistor passes through a DC-coupled differential amplifier (Lecroy DA1855A-PR2) and connects to the digitizer which has $1M\Omega$ input impedance (a 50Ω resistor is parallel to the digitizer for impedance match). For the floating potential measurements the voltage passes through a DC coupled amplifier (50Ω input impedance and $\geq$ 2MHz band width) with a gain of $A = \times 28$ for the high impedance output. A million samples ($2sec$) are usually obtained for the fluctuation data at each radial location, allowing for low-variance estimation of the fluctuation statistics.

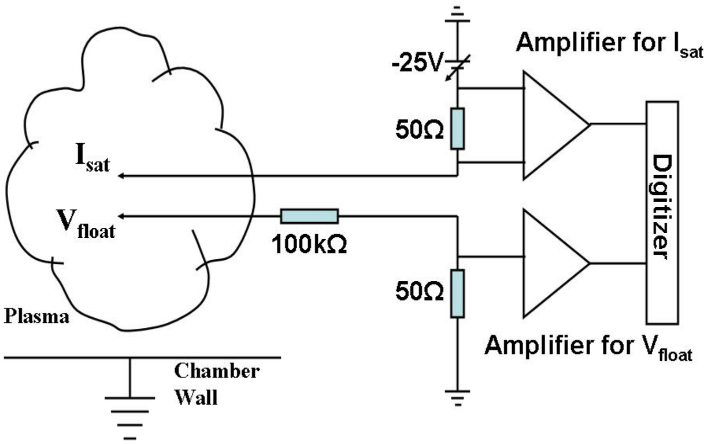

Figure 2.3: A circuit schematic of density and potential measurements

2.2.3 Fast-framing camera

A Phantom V.7 fast-framing camera is used to capture the visible light emission from the plasma. It uses 800×600 pixel SR-CMOS 12 bit monochrome sensor that is sensitive to visible light. For 128×64 resolution the sampling rate is as high as $102,000$/sec. It has continuously variable pre/post trigger allowing synchronizing Langmuir probe and camera. In experiments a Pentax 25mm f/1.4 lens is used with the camera to capture images through a telescope, which will be described in the next section.

2.2.4 Optical system

A large telescope (Celestron C11-SGT(XLT)) with small angle of view $(0.71\,^{\circ})$ provides optical path with rays that are very nearly parallel to the magnetic field. This view then effectively integrate light emission along the magnetic field, providing a line-integrated (r, θ)cross section of light emission. The aperture of the telescope is 280mm and focal length is 2800mm. Because of the large minimal focal length of the telescope and limited size of the lab, we use two mirrors to reflect the visible light from the plasma to insure enough distance for the focusing. The fast-framing camera is placed after the telescope to capture images. The whole setup is shown in Fig.2.4. The telescope and the camera are on a same optical table with leveling feet.

In this setup the camera and the two mirrors have adjustments in three dimensions, as well as pitch and yawn, while the telescope is fixed. Before taking images an alignment among camera, telescope and the vacuum chamber needs to be made. This is done by two

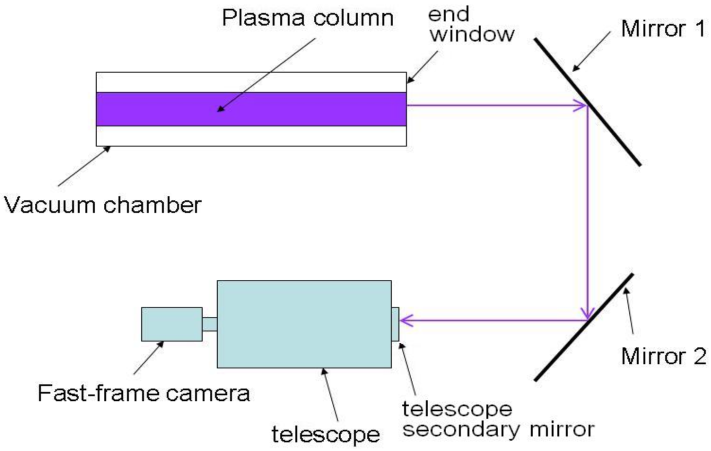

Figure 2.4: Layout of the optical system

steps. The first step is to align camera with telescope. We located the camera with lens close to the telescope and adjusted the camera focal plane to be the secondary mirror of the telescope. Then the transverse camera position is adjusted until the image of the secondary mirror is located at the center of the camera (See Fig.2.5a). Once the camera is aligned with the telescope, the second step is to align camera and telescope with the vacuum chamber. This is accomplished by first adjusting the camera focal plane to be the end window of the vacuum chamber. The center of the vacuum chamber window is located by a mechanical cross-hair mounted to the window. The alignment of the camera/telescope to the vacuum chamber is then done by adjusting the two mirrors such that the image of the center of the vacuum chamber is also the center of the source belljar located at the source end of the machine (See Fig.2.5b). Note that the images taken this way are reversed in left and right, up and down.

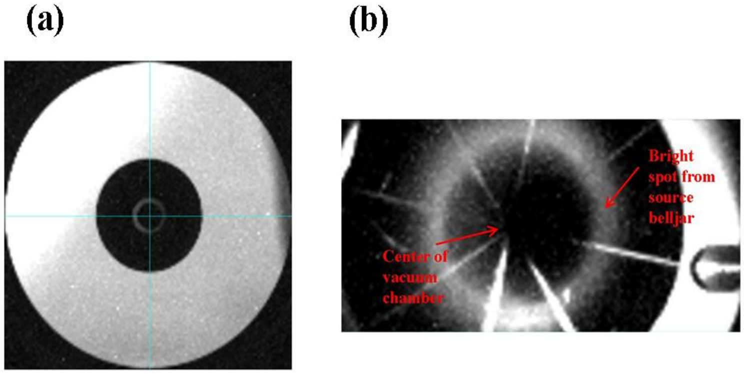

Figure 2.5: (a) Alignment between camera and telescope. (b) Alignment with vacuum chamber.

The light collected by the camera is a line-integrate light emission along the optical path for all wavelength λ, i.e., $I_{total} = \displaystyle\int I(\lambda)\, d\lambda$, where $I(\lambda)$ is the light emission intensity of wavelength λ. In general, the light emission from a given line is given by[47],

$$I(\lambda) = (const) n_e n_i \langle \sigma v \rangle \tag{2.1}$$

where n_e is the electron density, n_i is the ion density and $\langle \sigma v \rangle$ is the excitation rate of the spectral line of that ion. Therefore, $I_{total} \propto n_e f(T_e)$, where T_e is the electron temperature.

2.3 Methods of analysis

After the data was taken from the plasma, they are analyzed to study the underlying physics. This section describes the main analysis method we used in this thesis.

2.3.1 Statistical analysis

Most data are in the form of turbulent fluctuations, e.g., density, potential or light emissions, which are suitable for statistical analysis. The main statistical analysis methods include computing the auto-power spectrum $S_{xx}(f)$, cross-power spectrum $S_{xy}(f)$, cross-correlation $C_{xy}(f)$, coherence $\gamma_{xy}(f)$ and cross-phase $\alpha_{xy}(f)$, as well as probability distribution function(PDF), joint PDF and skewness. The definitions of these used in this thesis are described as below:

$$S_{xx}(f) = \left\langle |X(f)|^2 \right\rangle \tag{2.2}$$

$$S_{xy}(f) = \langle X^{\star}(f)Y(f) \rangle \tag{2.3}$$

$$\gamma_{xy}(f) = |S_{xy}(f)| / \sqrt{S_{xx}(f)S_{yy}(f)} \tag{2.4}$$

$$\alpha_{xy}(f) = Im(S_{xy}(f))/Re(S_{xy}(f)) \tag{2.5}$$

$$C_{xy}(\tau) = \int_0^T x(t)y(t-\tau)\,dt \tag{2.6}$$

where $X(f)$ and $Y(f)$ are the Fourier transform of the zero-mean time series data $x(t)$ and $y(t)$ respectively, $\star$ denotes complex conjugate, Im denotes the imaginary part, Re denotes the real part, and τ is the time lag between two time series data. Windowed FFT (fast Fourier transform) is used for the spectrum computation. Then the average value is obtained by taking ensemble average of all windows (denoting the number of windows to be M). Each realization is $T = Nt_s$ seconds in duration, with N denoting the total number of samples in each window and t_s the sampling rate. The minimal frequency resolution is $df = 1/T$ and the highest frequency that can be resolved is the Nyquist frequency $f_{Nyq} = 1/2t_s$. Therefore, the value of N should be chosen to be large enough to obtain sufficient frequency resolution. In our experiments for the ensemble averaged quantities N is chosen to have $T \sim$ 16ms. Thus the minimal frequency resolution is $\sim$ 60Hz. Hundreds of ensembles are usually obtained for the total 2s duration data allowing for low-variance estimation of the fluctuation statistics.

The probability distribution function (PDF) is computed by the histogram of the time series data normalized by its root mean square. The skewness is the third standardized moment, and defined as

$$\gamma_1 = \frac{\mu_3}{\sigma^3} \tag{2.7}$$

where,$\mu_3 = \langle (x - \langle x \rangle)^3 \rangle$ is the third moment about the mean $\langle x \rangle$. σ is the standard deviation. PDF and skewness are measures of the intermittency of the fluctuations. It has been reported that there is a universal nature to bursts of outward-going blobs of plasma in the edge of magnetic confinement laboratory plasma devices[49]. Such events are normally characterized by the non-Gaussian PDF of the ion-saturation current in regions where these events are being generated and propagating.

2.3.2 Bispectral analysis

The statistical analysis methods described in the previous section generally characterize the linear properties of the systems, and provide limited information about the nonlinear processes involved in the dynamics of the system. Bispectral analysis, on the contrary, is relevant in all system featuring quadratic nonlinearity in their governing equations, such as the convective derivative found in the plasma fluid description.

Bispectrum statistics maybe considered as Fourier transformed triple-point correlations, or frequency resolved skewness. Bispectra are transformed triple-point correlations in same sense that power spectra are transformed two-point correlations. Define the autobispectrum $S_{k_3}(k_1, k_2)$ of a signal ϕ_k as,

$$S_{k_3}(k_1, k_2) = \left\langle \phi^{\star}_{k_3} \phi_{k_1} \phi_{k_2} \right\rangle \tag{2.8}$$

where ϕ_k represents a Fourier transform of signal in wavenumber k space. The same definition may be easily written in frequency domain. The bicoherence $b_{k_3}(k_1, k_2)$ is defined as,

$$b_{k_3}(k_1, k_2) = \frac{\left|\left\langle \phi^{\star}_{k_3} \phi_{k_1} \phi_{k_2} \right\rangle\right|}{\sqrt{\left\langle |\phi_{k_3}|^2 \right\rangle} \sqrt{\left\langle |\phi_{k_1}|^2 \, |\phi_{k_2}|^2 \right\rangle}} \tag{2.9}$$

and the biphase $\Theta_{k_3}(k_1, k_2)$ as

$$\Theta_{k_3}(k_1, k_2) = \arctan\left(\frac{Im(S_{k_3}(k_1, k_2))}{Re(S_{k_3}(k_1, k_2))}\right) \tag{2.10}$$

These measures represent an ensemble-averaged coherency of the three modes which satisfy the matching condition $k_3 = k_1 + k_2$, or equivalently in frequency space $f_3 = f_1 + f_2$.

To see the utility of the bispectrum, consider a highly simplified model of the azimuthal momentum balance as we have described in Section 1.3, Eqn.1.13-1.16. Eqn.1.16 shows that to obtain the amount of the energy exchanged between a given triplet waves requires the knowledge of the coupling coefficient, which requires the bispectrum three waves analysis. However, in this thesis, we will just evaluate the auto-bicoherence defined as Eqn.2.9 from one field model to look at the nonlinear energy transfer, which will only tell the possible nonlinear coupling between different modes, but not the actual energy transfer directions and amount. A full bispectral analysis of the turbulence kinetic energy is performed underway by others in our research group.

2.3.3 Velocity measurements

To study the drift-wave turbulence/shear flow interactions the capability of measuring velocity field of the plasma is a necessary. In this section we will describe several methods used in this thesis to determine the velocity field.

2.3.3.1 Velocity measurements from 1D TDE technique on probe and imaging

The time-delay estimation (TDE) technique has been used in some plasma experiments to determine the mean fluctuating velocity field[5, 50]. The detailed investigation of this technique can be found in Ref.[52]. The main idea of this technique is to measure the advection of a quantity such as the density or potential, and then compute the cross-correlation (Eqn.2.6) between two measurements obtained at two separate locations that are separated by some distance less than the turbulent correlation length. The correlation function $C_{xy}(\tau)$ has a maximal value at some time lag τ_{max} , from which the TDE velocity is calculated by $u = \dfrac{\Delta x}{\tau_{max}}$, where Δx is the separation distance. Applying this technique to two azimuthally separated probe tips will provide a azimuthal velocity at that location. In the calculation presented in this thesis, to get a time-averaged velocity field, we choose a time window to be $1ms$, which is larger than the fluctuation time scale (in the order of $10 - 100\mu s$). By moving the time window T and repeating the calculation, an ensemble of different correlation function is calculated. Let us denote the total number of time windows as M. These M correlation functions from all time windows are then averaged, and the mean velocity is found from the peak of this averaged correlation function. To find a slowly-varying velocity field, the time window T is kept as $1ms$ and the window is slided with $128\mu s$ spacing, but no ensemble average is computed. Since the plasma rotates once in $\sim 0.5m$s and the sheared azimuthal flow evolves at a frequency of hundreds of Hz (which will be described in details in chapter 4), we therefore choose an intermediate time window length, $T = 1m$s. This window will average the azimuthal mode number m $>$0 turbulence, but still resolve the more slowly varying sheared azimuthal flow. The choice of 128μs spacing ensures the highest frequency that can be resolved of the varying azimuthal flow is $\sim$ 4kHz, well above the slowly varying sheared azimuthal flow frequency.

The TDE technique can also be applied to the fast-framing imaging data. To obtain we first perform a time average image from 2000 frames. Then subtract this averaged intensity from the instantaneous image. This then results in an image of the fluctuation intensity, which is related to plasma density. We then select a series of pixel points along the azimuthal direction with radius R on the density fluctuation images (see Fig.2.6)and denote the pixel point located at $\theta = 0$ as the reference point and then calculate the cross-correlation between the first two pixel points' time history data (as described above). The separation between the two pixel points that are cross-correlated is then increased and the correlation function is computed and another τ_{max} and velocity u are found. This process is repeated with increasing separation until the correlation peak value reaches a threshold. Here we set the threshold value to be 0.4. Fig.2.6b shows the decreasing of correlation peak value with increasing separation. By doing this, a series of $\Delta x - \tau_{max}$ pairs are obtained, which are the symbol star shown in the Fig.2.6c. Lastly we linear fit these data points and the velocity is computed as the gradient of this fit line, i.e., $u = \dfrac{dx}{d\tau}$.

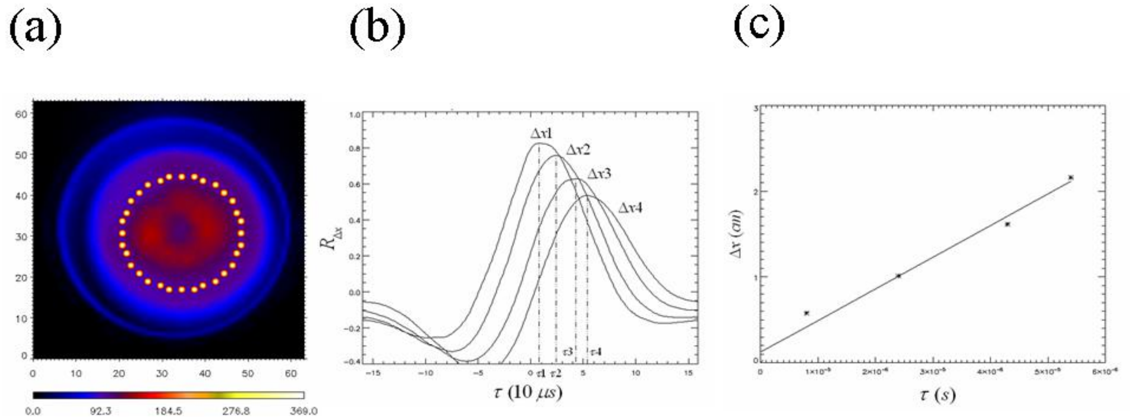

Figure 2.6: (a) Image with selected circular pixel points high lightened. (b) Cross-correlation $C_{xy}(\tau)$ between two pixel points with increasing separation Δx. (c) Distance Δx between two-pixel points v.s. time lag τ.

2.3.3.2 Velocity measurements by 2D TDE on fast-framing imaging

A 2D flow field was obtained by applying 2D TDE to the fast-framing images. The principle of this algorithm is: instead of computing the cross-correlation between 1D data sets(azimuthal or radial), we compute the cross-correlation in a range of $A \times B$ 2D area with a series of given increasing time lag τ from $\tau = 0$ with a time step $\delta\tau$. For example, Fig.2.7 is a 2D 11×11 grid centered at point $P_0(x_0, y_0)$. To compute the velocity at point $P_0(x_0, y_0)$ we first compute the cross-correlation between point $P_0(x_0, y_0)$ and other points located in a square range from $(x_0 - 5, y_0 - 5)$ to $(x_0 + 5, y_0 + 5)$ for a time lag $\tau = 0$. A 2D 11×11 cross-correlations are obtained with the maximal value R_{max} located at point $P_0(x_0, y_0)$. This process is then repeated for a new time lag $\tau_1 = \tau + \delta\tau$, and a new 2D cross-correlations is obtained with the maximal value R_{max} located at point P_1. Same process is repeated for increasing time lag until the maximal cross-correlation R_{max} is smaller than some threshold set initially as R_0. The velocity vector $\vec{v}$ is then a linear fit of these R_{max} data points shown by the blue arrow.

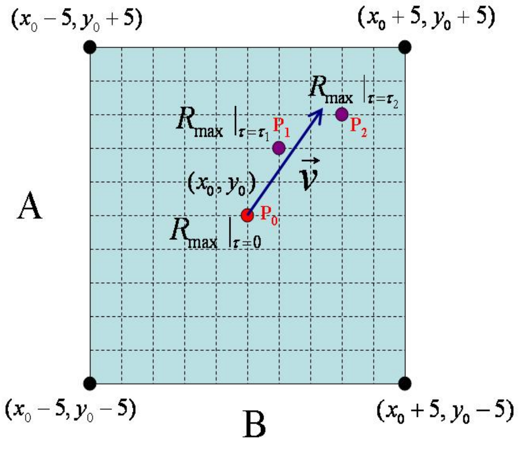

Figure 2.7: 2D time-delay estimation (TDE) technique.

2.3.3.3 Velocity measurements from probe by Two-point technique

The two-point technique was first proposed by Beall et al.[53]. The two-point spectrum $S(k, \omega)$ is the power spectrum of the fluctuations in both frequency (ω) and wavenumber (k) space. It reveals the dispersion relation $\omega(k)$ of the fluctuations. When $S(k, \omega)$ is integrated over k, the standard power spectrum as a function of frequency $S(\omega)$ is obtained. When it is integrated over frequency ω, a spectrum in wave number space

$S(k)$ is obtained.

Velocity from two-point technique can be realized by utilizing two spatially separated probe tips measuring same field quantities. A cross-phase α of the mode between two probe tip pairs is firstly estimated for a series M FFT time window. The local wave number is then obtained from $k(\omega) = \dfrac{\alpha}{\Delta x}$. For each FFT window the power-weighted phase velocity can be computed as $u_n = \sum_\omega \sum_k \dfrac{\omega}{k} S(k, \omega) / \sum_\omega S(\omega)$. The averaged velocity is then the ensemble average of all the FFT windows $u = \dfrac{\sum_n u_n}{M}$. A key assumption for the two-point technique to work is a unidirectional flow in the direction of the probe tip difference. A violation of this would be the case of counter-propagating modes. In previous work, Burin[19] has tested this with a quartet of the sinusoids signals, $y(t) = \sum_1^4 y_i$, where $y_i = \sin(\omega_i t + \theta_i)$, and where θ_i may vary between members of ensembles. It is found for the counter-propagating mode the dispersion relation is erroneously lying along a vertical line at the average phase delay $\alpha \approx 0$. In CSDX this assumption is satisfied since the plasma flows mainly in one azimuthal direction (can be verified by the fast-framing imaging).

2.3.4 Estimation of turbulent Reynolds stress

The turbulent Reynolds stress is given as $RS = \langle \widetilde{v}_r \widetilde{v}_\theta \rangle$, where $\widetilde{v}_r$ and $\widetilde{v}_\theta$ are computed from $\vec{E} \times \vec{B}$ drift velocity, i.e., $\widetilde{v}_r = \widetilde{E}_\theta / B_0$ and $\widetilde{v}_\theta = -\widetilde{E}_r / B_0$, and $\langle\rangle$ denotes a time or ensemble average. This is based on the assumption that the dominant plasma flow is $\vec{E} \times \vec{B}$ drift. Since for CSDX the fluctuation frequency is much less than the ion cyclotron frequency ($\dfrac{\omega}{\Omega_{ci}} \approx 0.03 - 0.3$) and the ion-ion collisional frequency is marginally below the ion cyclotron frequency ($\frac{\mu_{ii}}{\Omega_{ci}} \approx 0.3 - 1.0$), this assumption is reasonable for our experimental conditions. The radial and azimuthal electric fields are computed from the gradient of the measured floating potential, assuming the electron temperature fluctuations are negligible, i.e., $\widetilde{E}_r = -\frac{\Delta\widetilde{\phi}}{\Delta x_r}$ and $\widetilde{E}_\theta = -\frac{\Delta\widetilde{\phi}}{\Delta x_\theta}$.

The turbulent Reynolds stress could also be computed spectrally as [57],

$$\langle \widetilde{v}_r \widetilde{v}_\theta \rangle = C_{\widetilde{v}_r \widetilde{v}_\theta} = \int_{-\infty}^{\infty} S_{\widetilde{v}_r \widetilde{v}_\theta}(f) e^{i2\pi f\tau}|_{\tau=0}\, df \qquad (2.11)$$

where, $C_{\widetilde{v}_r \widetilde{v}_\theta}$ is the cross-covariance between $\widetilde{v}_r$ and $\widetilde{v}_\theta$. τ is the time lag and $S_{\widetilde{v}_r \widetilde{v}_\theta}(f)$ is the cross-spectrum between $\widetilde{v}_r$ and $\widetilde{v}_\theta$. Since the cospectrum ($Re(S_{\widetilde{v}_r \widetilde{v}_\theta}(f))$) is an even function of f and the quadspectrum ($Im(S_{\widetilde{v}_r \widetilde{v}_\theta}(f))$) is an odd function of f, Eq.2.11 becomes,

$$\langle \widetilde{v}_r \widetilde{v}_\theta \rangle = 2\int_{0}^{\infty} Re(S_{\widetilde{v}_r \widetilde{v}_\theta}(f))\, df \qquad (2.12)$$

and we arrive at,

$$\langle \widetilde{v}_r \widetilde{v}_\theta \rangle = \int_{0}^{\infty} 2\gamma_{\widetilde{v}_r \widetilde{v}_\theta} \cos\alpha_{\widetilde{v}_r \widetilde{v}_\theta} \sqrt{S_{\widetilde{v}_r \widetilde{v}_r}(f)}\sqrt{S_{\widetilde{v}_\theta \widetilde{v}_\theta}(f)}\, df \qquad (2.13)$$

This representation would allow us to determine how the cross-spectrum $S_{\widetilde{v}_r \widetilde{v}_\theta}(f)$, cross-phase $\alpha_{\widetilde{v}_r \widetilde{v}_\theta}$ and the cross-coherence $\gamma_{\widetilde{v}_r \widetilde{v}_\theta}$ contribute to the Reynolds stress. We will utilize this representation to investigate the statistical properties of the turbulent Reynolds stress and the detailed results are described in the next chapter.

3

Statistical properties of the turbulent Reynolds stress and its link to the shear flow generation

3.1 Introduction

In magnetic confinement fusion devices the anomalous transport across the magnetic field is thought to be caused by plasma turbulence. The two fundamental instabilities are thought to be the interchange instability and the drift wave instability[17, 58]. Theory suggests for a given background pressure gradient, the turbulence saturation occurs via the formation of a large-scale shear flow that is generated by the turbulence Reynolds stress (radial transport of azimuthal momentum) which mediates the nonlinear transfer of turbulent momentum and kinetic energy into the larger scaled shear flow. The shear flows can also mitigate turbulence by tearing apart turbulent eddies, resulting in the formation of a self-regulating complex system[8]. Many experimental studies in tokamaks have provided evidence of the existence of shear flow during the transition from L mode to H mode[39, 50, 37], as well as in stationary discharges[31]. In recent experiments carried out on the Controlled Shear Decorrelation eXperiment (CSDX) linear device, a radially sheared azimuthal flow has been demonstrated to be sustained by the Reynolds stress against ion-neutral collisional and viscous damping through the analysis of momentum balance (see Fig.1.14), providing a direct experimental test of the theory of drift-turbulence/shear flow interaction[41, 59].

In all the theoretical and experimental studies of turbulence/shear flow interactions the Reynolds stress plays an important role. However, in the existing publications, only the measured mean Reynolds stress profile and its link with the large-scale shear flow have been examined[39, 60, 61, 62]; to date there has been no study of how the turbulent statistical properties (e.g. turbulence amplitudes, cross phases, cross coherency) lead to the development of the detailed Reynolds stress profile associated with the shear flow. Furthermore, no detailed experimental study of the link between the turbulent Reynolds stress, background shear flow, and formation of bursty transport events has been carried out.

This chapter describes such a detailed study of the statistical properties of the turbulent Reynolds stress in a laboratory-scale plasma device and uses these results to build a physical picture of shear flow generation from turbulent momentum transport that is consistent with experimental observations. The results show that the cross-phase between turbulent radial and azimuthal velocity fields plays a critical role in determining the divergence of the turbulent Reynolds stress, which drives shear flow between the density gradient maximum and the peak shear layer (we denote this region as the negative viscosity region, since the turbulent shear stress is acting to reinforce the shear flow); at other radial locations the Reynolds stress acts to dissipates shear flow. Bursts of outward going positive density fluctuations are born at or near the density gradient maximum, and carry positive azimuthal momentum, resulting in a positive Reynolds stress in this region. As the fluctuations move outwards from the maximum density gradient and towards the shear layer their amplitudes decrease, resulting in a gradual decrease in the positive Reynolds stress, which then results in a negative stress divergence that reinforces the shear flow. These results indicate that a system of radially propagating turbulent structures which are immersed within a background seed shear flow naturally form a Reynolds-stress profile that then acts to reinforce the shear flow.

We have also examined the role that the collisional ion-ion viscosity plays in determining the time-averaged azimuthal flow profile. Collisional viscosity acts to transfer azimuthal flow from the shear layer located at the periphery of the plasma column into the central plasma region. If this viscosity is strong enough then it will give (nearly) solid body azimuthal rotation near the plasma axis resulting in the formation of plasma rotation in the central region away from the shear layer. The similarities of these results with observations in tokamak devices are pointed out, suggesting that the observations may be a universal signature of turbulent-driven shear flows interacting with bursty transport events, and may also be related to recent reports of links between edge plasma flows and so-called ”intrinsic rotation” in the core of tokamak plasmas.

The rest of this chapter is organized as follows: In Sec. 3.2 we briefly describe our experimental set up. In Sec. 3.3, we present our probe measurements of turbulent Reynolds stress, while in Sec. 3.4 we show the statistical properties of the Reynolds stress. In Sec. 3.5 we compare with intermittent density fluctuations, following it is the section 3.6 discussions, and lastly in Sec. 3.7 we review and summarize our results.

3.2 Radial profiles of equilibrium and fluctuating quantities

The measurements presented here are made on the linear machine CSDX plasma device described in the precious chapter. The plasma was operated with 4mTorr Argon gas pressure, 1kG magnetic fields and 1.5kW power input. Measurements are made by the 18-tip Langmuir probe (See Fig.2.2) located at an axial position $Z = 170$cm downstream of the exit of the plasma source. The frame rate for the fast-framing imaging measurements is $100,000$/sec with 64×64 image resolution, and a Pentax 50mm $f/1.4$ lens is used in the experiments. The Langmuir probe is out of the plasma when recording images.

Fig. 3.1(a, b) shows the radial profile of time-averaged plasma density and the amplitude of the density fluctuations, as well as the radial particle flux. As can be seen the fluctuation amplitude peaks near the region of maximal density gradient, i.e. $r \approx 3.1$cm (This position is shown by the dot-dashed line on all the radial profiles in this chapter). Previous work has shown these fluctuations are collisional drift waves driven unstable by electron-ion collisions[19]. Measurements of the mean azimuthal plasma velocity using the two-point estimation technique, along with the momentum balance analysis discussed in chapter 1 [59], using the model of the ion-ion viscosity profile shown in Fig.3.1 (d) are also shown in Fig.3.1 (e). The results show that the plasma exhibits roughly solid body rotation for $r < 3.5$cm , while for the region $r > 4$cm the azimuthal velocity is inversely proportional to the radius. A radial shear layer of the azimuthal velocity then exists at the interface region located between 3.5cm$< r < 4$cm, which is shown by the shadow region on all the radial profiles in this chapter. In previous work we have shown that this shear layer is consistent with the experimentally observed turbulent Reynolds stress for reasonable estimates of the collisional ion-ion viscosity[59, 41]. The effect of different ion-ion viscosity profiles are also examined here, and are discussed in section 3.6.

Fig. 3.1(c) shows the radial profile of the time-averaged Reynolds stress $\langle \widetilde{v}_r \widetilde{v}_\theta \rangle$. In this chapter we use an averaging timescale of 0.45msec, which corresponds to the timescale needed for the plasma at $r = 3.6$cm to rotate once in the azimuthal direction (and thus this timescale provides an effective average over all fluctuations with azimuthal mode number $m > 0$). Because CSDX operates in a steady state we record several 10^3 plasma rotation periods resulting in small statistical variance (which is within the thickness of the lines for these results). As a result, these results present an ensemble averaged picture and average out slow variations that occur.and In this figure the $\langle \widetilde{v}_r \widetilde{v}_\theta \rangle$ profile peaks at $r \sim 3.3$cm, while at $r < 2.8$cm and $r > 3.8$cm, the Reynolds stress becomes negative. Earlier results show that the divergence of the Reynolds stress (which then indicates either the concentration or diffusion of angular momentum) is balanced by the dissipation profile[59, 41].

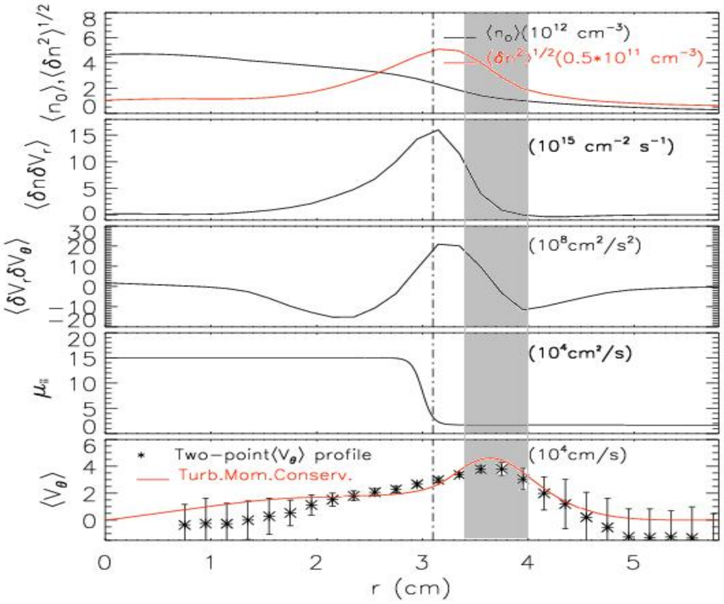

Figure 3.1: Radial profiles of relevant equilibrium quantities: (a) Time-averaged density profile (black solid line) and RMS amplitudes of density fluctuations (solid red line). (b) Time-averaged turbulent radial particle flux. (c) Time-averaged turbulent Reynolds stress. (d) Model of ion-ion viscosity profile estimated from measured plasma density and line-averaged ion temperature. (e) Mean azimuthal velocity profiles measured by two-point technique ($\star$) and predicted by turbulent ion momentum balance (red solid line). In all figures the dot-dashed line is the position of the density gradient maximum. Shadow region indicates the shear layer location

3.3 Statistical Properties of Reynolds Stress

In this chapter, we are interested in the origin of the shape of the turbulent Reynolds stress profile, since it is this shape that enters most critically into the turbulent momentum conservation equation. We therefore use different statistical analysis tools to investigate the statistical properties of the turbulent Reynolds stress, including calculation of the power spectrum, cross-phase, and cross-coherence between the two fluctuating velocity components, as well as the PDF of the velocities.

The absolute magnitude of the frequency-resolved power spectrum $S_{R(t)}(f)$ of the turbulent Reynolds stress $R(t) = \widetilde{v}_r \widetilde{v}_\theta$ at 1kG is shown in Fig. 3.2(a). The strongest power featured at 15kHz-23kHz is located at approximately $r \sim$ 3.3cm, which is close to the region of density gradient maximum. Using previously published azimuthal wavenumber spectra[19], these frequencies correspond to azimuthal wave numbers in the range of $2 - 3cm^{-1}$, which correspond to fluctuation $\tilde{\phi} \propto e^{im\theta}$ with azimuthal mode number $m = 5 - 10$. Thus the Reynolds stress is associated with fluctuations with spatial scales that are significantly smaller than the plasma column radial scale $\sim 4 - 5$cm. Most power of the turbulent Reynolds stress is concentrated in the region from $r \sim$ 2cm to $r \sim$ 5cm with broadband frequency properties. Outside this region the power drops off rapidly. Fig.3.2(b) and (c) show the radial and frequency resolved cross-phase $\alpha_{\widetilde{v}_\theta \widetilde{v}_r}$ between $\widetilde{v}_r$ and $\widetilde{v}_\theta$ and the squared cross-coherence $\gamma^2_{\widetilde{v}_r \widetilde{v}_\theta}$. In both figures we see significant variations in a region from $r \sim$ 3.0cm to $r \sim$ 3.8cm, with cross-phase first changing from $-\pi$ to 0 then to π (or equivalently $-\pi$), and the coherence changing from 0.8 to 0 then back to 0.5.

(The sign here is such that a positive cross-phase means $\widetilde{v}_r$ leads $\widetilde{v}_\theta$ in time). This region is the same as where the shear flow is located. It is also interesting to note that the innermost location of this phase change coincides with the mean density gradient maximum location and, as shown below, coincides with the birth location of outward going positive density events.

The power-weighted averages over frequency of these two quantities defined as $\langle \alpha_{\widetilde{v}_r\widetilde{v}_\theta} \rangle = \dfrac{\int \alpha_{\widetilde{v}_r\widetilde{v}_\theta} \left| S_{\widetilde{v}_r\widetilde{v}_\theta}(f) \right| \, df}{\int \left| S_{\widetilde{v}_r\widetilde{v}_\theta}(f) \right| \, df}$ and $\left\langle \gamma^2_{\widetilde{v}_r\widetilde{v}_\theta} \right\rangle = \dfrac{\int \gamma^2_{\widetilde{v}_r\widetilde{v}_\theta} \left| S_{\widetilde{v}_r\widetilde{v}_\theta}(f) \right| \, df}{\int \left| S_{\widetilde{v}_r\widetilde{v}_\theta}(f) \right| \, df}$ are shown in Fig.3.3 (a) and (b). It is clear that at $r \sim 3.4$cm the cross-phase goes to 0, while the coherence drops down to 0.2. The fact that the cross-coherence nearly vanishes at the shear location indicates that there is only a weak statistical correlation between the two fluctuation velocity components at this position. As a result, the cross-phase between the two velocity components must vary nearly randomly between $[-\pi, \pi]$ at the shear layer location from one ensemble to the next, as might be expected for two randomly phased signals. When averaged over many statistical ensembles, the cross-phase then averages to a small value at the point where the cross-coherency vanishes as seen in our results.

We now use the expression described in Eqn.2.13 to investigate how the cross-spectrum $S_{\widetilde{v}_r\widetilde{v}_\theta}(f)$, cross phase $\alpha_{\widetilde{v}_r\widetilde{v}_\theta}$ and cross-coherence $\gamma_{\widetilde{v}_r\widetilde{v}_\theta}$ contribute to the total Reynolds stress. Fig.3.4 shows the comparisons between the time-averaged Reynolds stress directly measured in experiments and from the above computations, in which the black solid line includes all the factors of power-spectrum, cross-phase and cross-coherence, and the blue, red and purple solid line exclude the cross-phase, cross-coherence and both

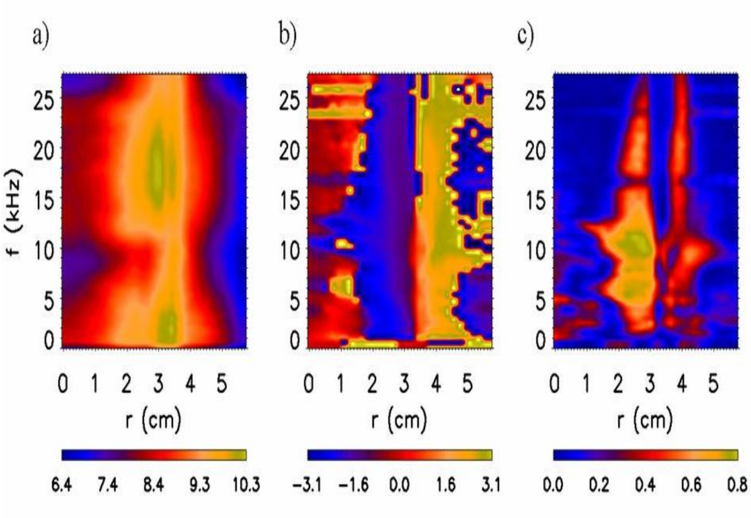

Figure 3.2: (a) Absolute magnitude of the power spectrum of the turbulent Reynolds stress ($\log_{10}$). (b) Cross-phase between radial and azimuthal turbulent velocity fields $\alpha_{\widetilde{v}_r \widetilde{v}_\theta}$. (c) Squared cross-coherence between radial and azimuthal turbulent velocity fields $\gamma^2_{\widetilde{v}_r \widetilde{v}_\theta}$.

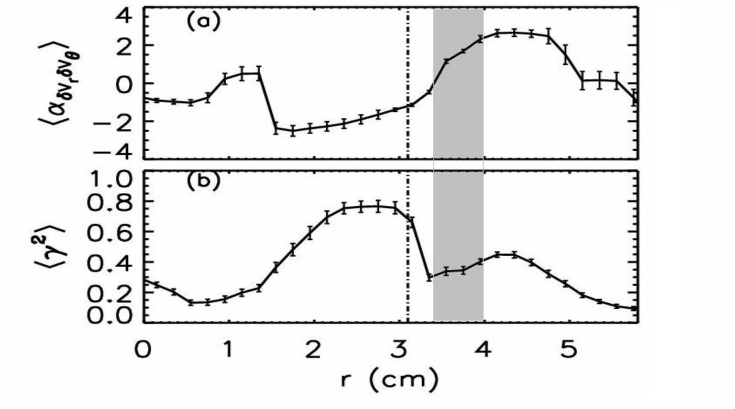

Figure 3.3: (a) Power-weighted average cross-phase $\langle \alpha_{\widetilde{v}_r \widetilde{v}_\theta} \rangle$. (b) Power-weighted average squared cross-coherence $\left\langle \gamma^2_{\widetilde{v}_r \widetilde{v}_\theta} \right\rangle$.

respectively. It is found that when the cross-phase is excluded, the profile differs significantly from the experimental measurements, which are represented by the symbol '+'. However, when the cross-coherence only is excluded, the profile agrees strikingly well with direct measurements. This shows that the cross-phase provides the dominant contribution to the shape and magnitude of the Reynolds stress. The radial and frequency resolved cosine of the cross-phase is evaluated, as well as the power-weighted average cosine of cross-phase, which is shown in Fig.3.5(a) and (b). The cosine of the cross-phase changes sign at $r \sim 2.8$cm and $r \sim 3.8$cm, which is the same as where the time-averaged Reynolds stress changes sign. This result indicates again that the cross-phase plays a determining role in the shape of the time-averaged Reynolds stress (and thus in the divergence of the Reynolds stress).

These FFT-based analyses provide a time-averaged view of the turbulence. To obtain insight into the dynamics of the turbulence, we now look at the PDF and the skewness (i.e. the third moment of the PDF) of the turbulent Reynolds stress. Fig.3.6(a) shows the turbulent Reynolds stress PDF at three different radial locations. At $r \sim 2$cm, which is inside of the shear layer and density gradient maximum, the PDF shows a significant negative skewness (see also Fig.3.6b) indicating that on average the Reynolds stress is composed of either outward going transport of negative perturbed azimuthal velocity events, or of inward going positive perturbed azimuthal velocity events. At $r \sim 2.8$cm the PDF is close to symmetric, indicating no preferential transport of azimuthal momentum. At $r \sim 3.4$cm, which is between the density gradient maximum and shear layer, the Reynolds stress PDF has a large (> 1) positive skewness indicative of intermittent

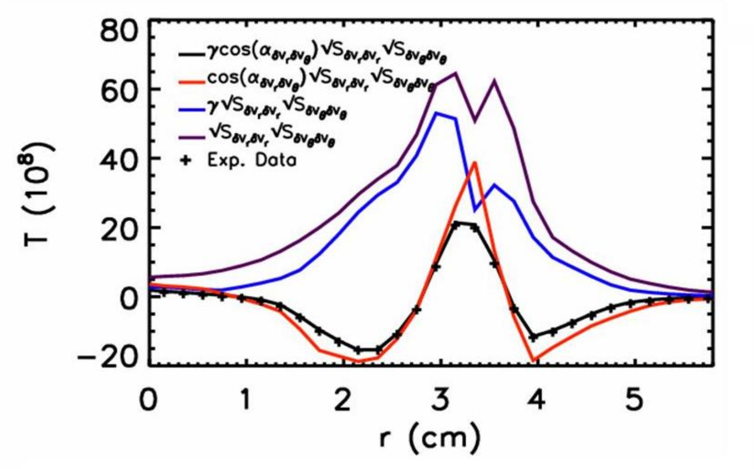

Figure 3.4: Experimentally measured time-averaged turbulent Reynolds stress (plus sign). Calculation including all factors of power spectrum, cross-phase and cross-coherence (black solid line), calculation with both cross-phase and cross-coherence excluded (purple solid line), calculation with cross-phase only excluded (blue solid line), and calculation with cross-coherence only excluded (red solid line).

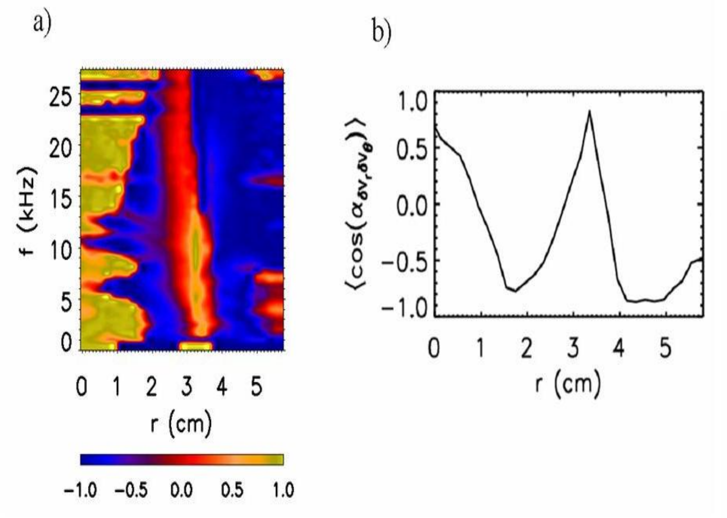

Figure 3.5: (a) Radial and frequency resolved $\cos(\alpha_{\widetilde{v}_r\widetilde{v}_\theta})$, and (b) power-weighted average $\langle\cos(\alpha_{\widetilde{v}_r\widetilde{v}_\theta})\rangle$.

or bursty momentum transport events which are characterized by outward-going positive turbulent azimuthal velocities. Fig.3.6(b) shows the radial profile of the skewness of the turbulent Reynolds stress. A comparison of Fig.3.6b with Fig.3.5b shows that the location where the skewness of the turbulent Reynolds stress is significantly positive (i.e. where outward going bursts of positive plasma flow occur) is linked to the variation of the cosine of the cross-phase between the radial and azimuthal turbulent velocity fields. This is borne out by an examination of the joint PDF of the turbulent velocity fluctuations shown in Fig. 3.7. At $r \sim$ 2cm and $r \sim 4$cm, the PDFs are oriented from the second quadrant pointing down towards the fourth quadrant, consistent with radial velocities that are out of phase with the azimuthal velocities. At $r \sim 3.4$cm, the velocities are in phase, and thus the joint PDF is oriented along an axis running from the first quadrant to the third quadrant.

3.4 Relationship between intermittent density fluctuations and Reynolds stress

It has been reported that there is a universal nature to bursts of outward-going blobs of plasma in the edge of magnetic confinement laboratory plasma devices such as tokamaks[63] and stellarators[64]. These blobs have also been referred to as intermittent plasma objects (IPOs) in the literature[63]. One simple signature of such events is that the PDF of the ion-saturation current exhibits strongly non-Gaussian distributions in regions where these events are being generated and propagating. Several mechanisms of the

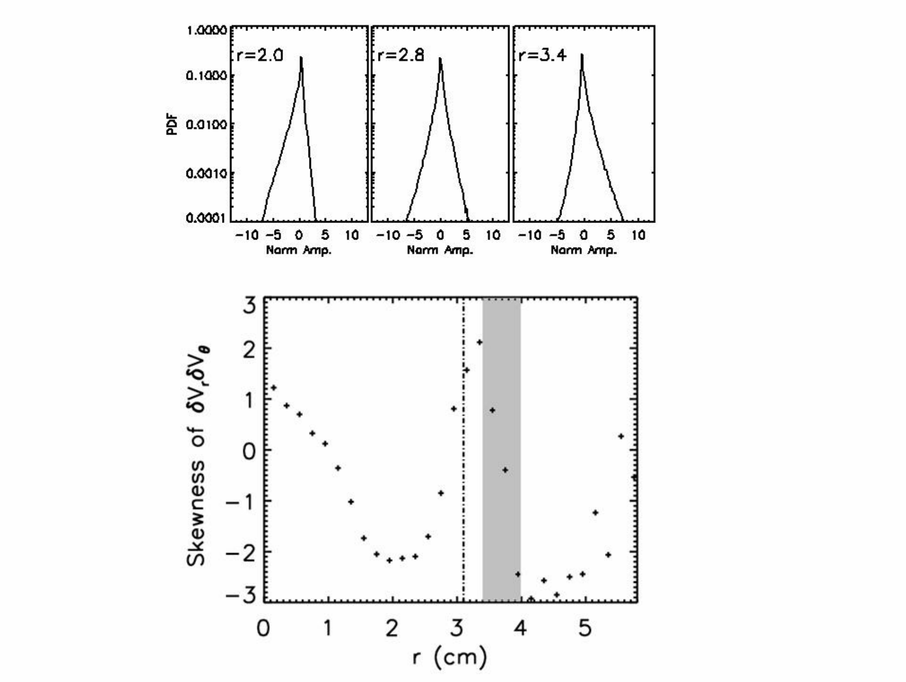

Figure 3.6: (a) Turbulent Reynolds stress PDF at three radial locations (normalized by standard deviation), and (b) radial profile of the skewness of the turbulent Reynolds stress $\widetilde{v}_r\widetilde{v}_\theta$.

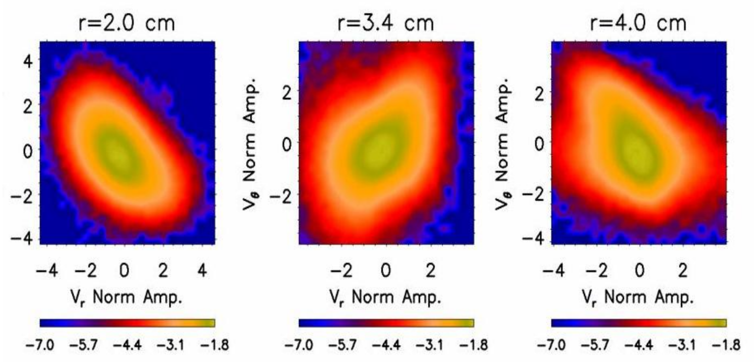

Figure 3.7: Joint PDF of radial and azimuthal velocity fields at three radial locations ($\log_{10}$). Normalization is standard deviation.

generation of these intermittent turbulent structures have been reported[65, 66]. These earlier results, and the behaviors of the Reynolds stress PDF discussed above, motivate us to examine the PDF of the ion saturation current. Here we provide experimental results which suggest that the behavior of the turbulent Reynolds stress and the generation of intermittent density bursts at the region are all related.

Fig.3.8(a) shows the PDF of ion saturation current at three different radial locations, $r = 2$cm, $r = 2.8$cm and $r = 3.4$cm. At $r = 2$cm the ion-saturation fluctuation is skewed negatively, indicating a predominance of negative going density events, while at $r = 3.4$cm the fluctuation is skewed positively, indicating a predominance of positive going density events at this location. At $r = 2.8$cm the distribution is close to symmetric, indicating that the outward going (inward going) positive (negative) density events are generated near the maximum density gradient. The Isat PDF behavior is also similar to those observed in the linear device LAPD[67] as well as at the edge of tokamak plasma devices[63]. Fig.3.8(b) shows the radial profile of the skewness of ion-saturation current fluctuations computed from the Isat PDF at each radial location. The Isat skewness changes sign at $r \sim 2.7$cm, and reaches a maximum near $r \sim 4$cm, after which it decays at larger radii. This behavior is consistent with the generation of positive bursts of density near the density gradient maximum.

We can gain additional insight by examining the radial and azimuthal turbulence correlation lengths computed from fast-framing imaging data (Fig.3.9). These correlation lengths are obtained by computing the cross correlations between the fluctuating intensity at two radially or azimuthally separated positions. The cross-correlation function enve-

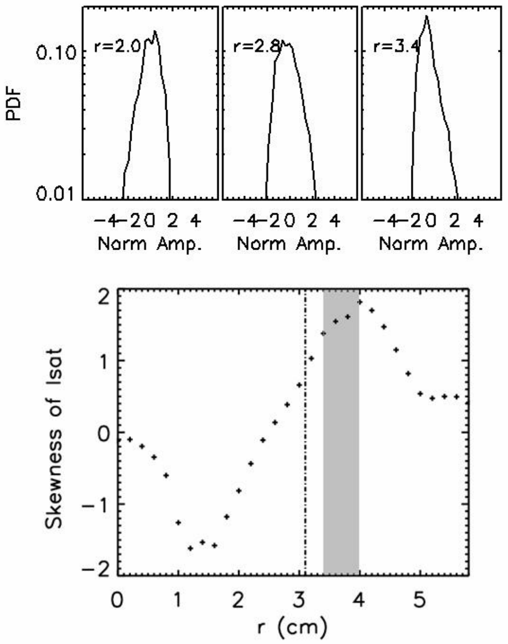

Figure 3.8: (a) PDF of the fluctuating ion saturation current at three radial locations (normalized by standard deviation), and (b) radial profile of the skewness of the fluctuating ion saturation current.

lope is then used to find the correlation length, defined as the location where the envelope is down by a factor of $1/e$ from the peak value at zero spatial separation. The light intensity of the image is somewhat correlated to the density fields, but also likely is influenced by the electron temperature fluctuations and neutral density. Regardless of this fact, we can still gain insight into the turbulence dynamics from this analysis. On the core side of the density gradient maximum the radial correlation length is larger than the azimuthal correlation length. Near the shear layer, there is a pronounced dip in the radial turbulence correlation length which is reduced to a few millimeters ($\sim$ 3mm) at the location of maximum flow shear, while the azimuthal turbulence correlation length is unchanged ($1.5 \sim$ 2cm). These results, with the Isat PDF shown above, indicate that the density fluctuations originate at or near the density gradient maximum and have, on average, a radially elongated shape at this location. Near the shear layer these turbulent fluctuations are elongated in the azimuthal direction, with an azimuthal correlation length that is about $3-4$ times larger than the radial correlation length. This behavior is similar to the $E \times B$ flow shear decorrelation process that is thought to occur in the edge of H-mode tokamak plasmas[68]. Outside the shear layer these perturbations recover their radially elongated shape, and move on average away from the shear layer. This is consistent with the observation of finger like blobs near $4 \sim$ 5cm from imaging in previous studies[49].

The joint PDF of the turbulent radial particle flux and the Reynolds stress is also investigated as seen in Fig.3.10. At $r \sim$ 2cm and $r \sim$ 4cm these PDFs are oriented from second quadrant to the fourth quadrant, and the largest probabilities lie in the second quadrant, indicating that the momentum transport is associated with outward going

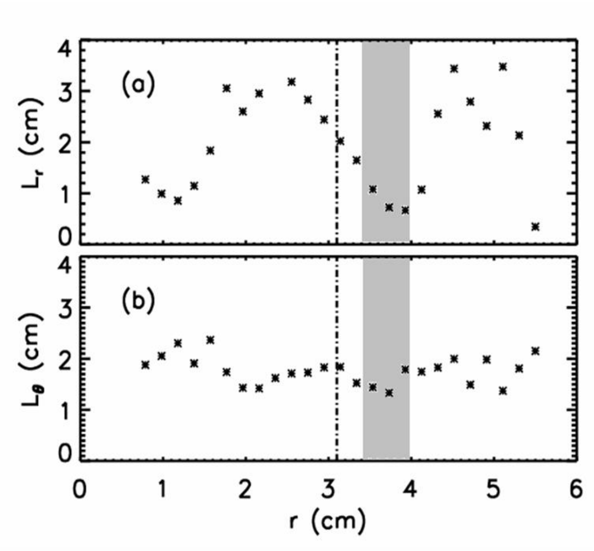

Figure 3.9: (a) Radial turbulence correlation length, and (b) azimuthal turbulence correlation length, both estimated from fast-imaging.

particle flux carrying a deficit of azimuthal momentum (i.e., a negative momentum fluctuation), which is consistent with negative skewness of the turbulent Reynolds stress at those locations. At $r \sim 3.4$cm, the joint PDF is oriented from the first quadrant to the third quadrant, with the largest probability lying in the first quadrant. This suggests that near the shear layer the bursty momentum transport is associated with outward going particle flux fluctuations carrying an excess of azimuthal momentum (a positive momentum fluctuation), consistent with the positive skewness of the turbulent Reynolds stress. An empirical investigation between the momentum and the particle transport was reported in the boundary region of fusion plasmas and suggested the same conclusion[69]. In the time-averaged analysis above, the cross-phase was shown to determine the detailed shape of the time averaged Reynolds stress profile, which in turn is linked to the time-averaged velocity shear layer. The Reynolds stress measurements, ion saturation current PDF, and the joint PDF between Reynolds stress and radial particle flux suggest that the turbulent Reynolds stress is associated with radially-directed plasma density events, which also carry azimuthal plasma flow and momentum. A significant negative radial divergence to such bursts of angular momentum transport will then lead to the concentration of azimuthal flow in that region[70].

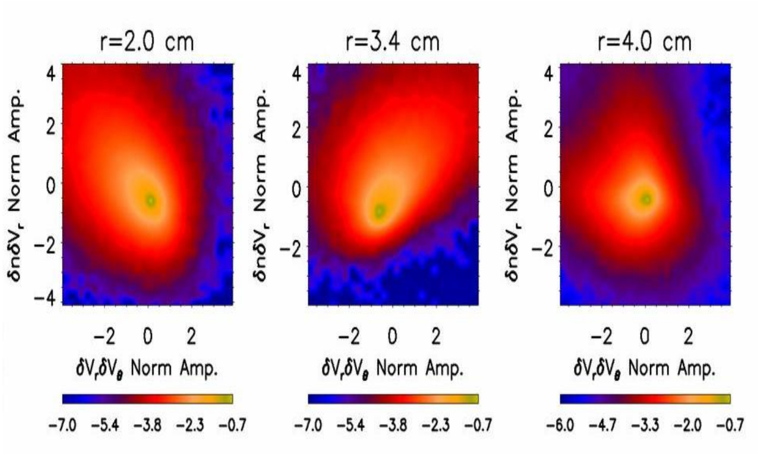

Figure 3.10: Joint PDF of radial particle flux and the turbulent Reynolds stress at three radial locations ($\log_{10}$). Normalization is standard deviation.

3.5 Discussion

The above results are consistent with the schematic of shear flow generation shown in Fig.3.11. The density fluctuations, due to collisional drift waves, have a peak amplitude at the largest density gradient region located at $r \sim r_2$(Fig.3.11a). The Isat skewness results show that at or near this region the outgoing density bursts or blobs are generated and on average form outward going positive density excursions, resulting in a positive Isat skewness at r_2. For $r < r_1$, these perturbations carry angular momentum with fluctuating radial and azimuthal velocity fields that are out of phase (Fig.3.11b), resulting a joint velocity PDF as shown in Fig.3.11c. As a result, the mean Reynolds stress is negative in the region $r < r_1$. In the region $r > r_2$, on average the fluctuations consist of outward going positive density events which have a positive azimuthal velocity increment associated with them. Thus in the region $r_2 < r < r_4$ the fluctuating radial and azimuthal velocity fields are in phase resulting in a positive mean Reynolds stress in this region (Fig.3.11b). The joint velocity PDF then has the orientation shown in Fig.3.11c. The location of the positive Isat skewness coincides with the positive turbulent Reynolds stress skewness comparing from Fig.3.6 and Fig.3.8, suggesting that the bursts of positive stress are associated with bursts of density, consistent with the results shown in Fig.3.10. The mean Reynolds stress decays for $r > r_3$ since the background density gradient is weaker here and thus the turbulence drive is weaker. In addition, the Reynolds stress couples energy from the higher frequency fluctuation scales into the shear flow, resulting in a decrease in fluctuation amplitude in this region. As a result, there is a peak in the turbulent stress located at $r \sim r_3$, which lies between the density gradient maximum and the shear layer located at r_4. The divergence of the Reynolds stress thus changes sign across the region from r_1 to r_4. A negative radial divergence to the momentum flux will act to amplify a positive azimuthal flow, resulting in the formation of a positive going flow in the region $r_3 < r < r_4$; a positive radial divergence to the momentum flux will drive a negative mean azimuthal flow, so the plasma rotation could be reversed either for $r_1 < r < r_3$ or for $r > r_4$. Evidence for such a flow reversal at large radius is indeed seen in our data (see Fig.3.1e). However, we expect that the collisional ion-ion viscosity is largest near $r \sim 0$ and it will act to dissipate the shear flow in the central part of the plasma column, resulting in nearly solid body rotation in this portion of the plasma. A detailed study of the effect of the ion-ion viscosity on plasma rotation is discussed below.

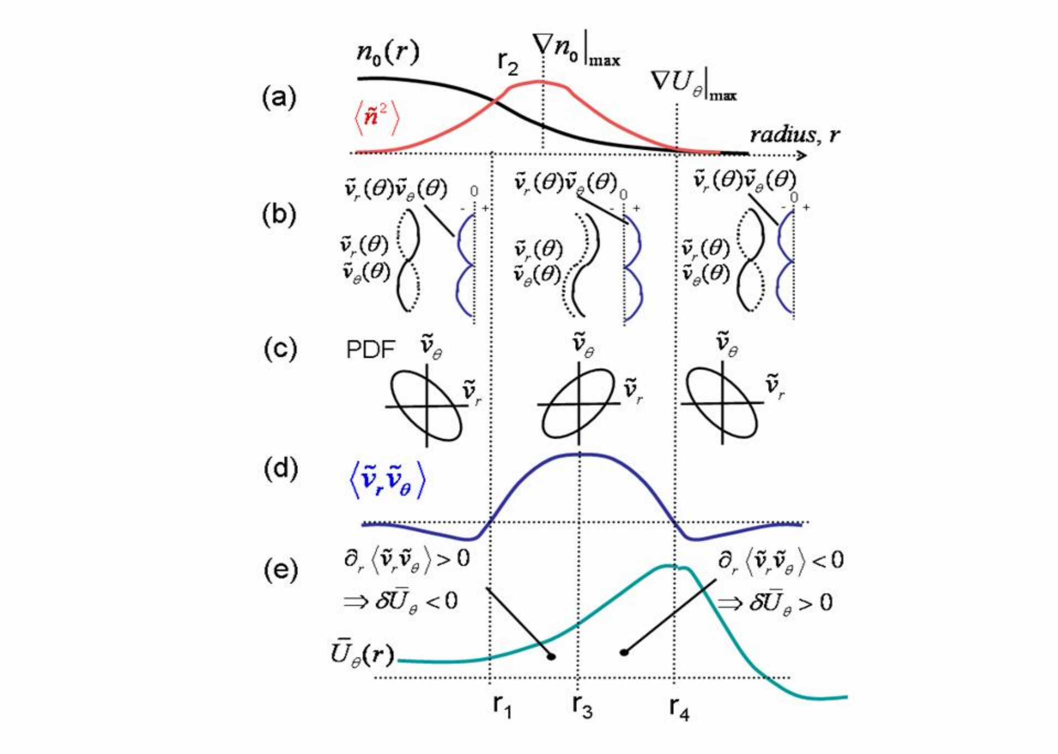

Figure 3.11: Physical picture of shear flow generation from drift turbulence.

Theory predicts that, since the turbulence shear flow interaction conserves energy, the radial correlation length of the turbulence will decrease[8], as seen in our observations. The reduction in radial correlation length is most pronounced where the Reynolds stress changes sign at r_4. At this location there is little or no radial transport of azimuthal momentum even though there are finite velocity fluctuations. Thus either the cosine of the velocity cross phase and/or cross-coherency of the two velocity components must vanish at this point. The link between the PDF of the Isat, Reynolds stress and the joint PDF of particle flux and Reynolds stress suggests a hypothesis where the plasma density fluctuations born near the maximum density gradient also carry angular momentum as well, and thus may in fact be two elements of the same underlying phenomena. Taken together with recent results from the TORPEX device[71] which show that the density blobs are formed by flow-shear ”pinching off” drift-interchange fingers of plasma extending from a dense core region into a lower density scrape-off layer region, these results point towards a strong link between turbulent generated shear layer formation, shear layer mediated bursty transport, angular momentum transport, and spontaneous central plasma column rotation. We are now planning experiments to test this picture using a combination of probe-based and fast imaging based diagnostics, and will report the results in future publications.

In the initial ion momentum balance analysis presented in Ref.[59] and [41], we assumed a step-like model of the ion-ion viscosity $\mu_{ii} = \rho_i^2 \nu_{ii} \propto nT_i^{-1/2}$ since we did not measure a radial profile of T_i. Here, we perform an analysis with different μ_{ii} profiles to better understand its effect on shear flow generation. Fig.3.12(a) shows several different plausible μ_{ii} profiles (step-like model and Gaussian, consistent with the mean density and ion temperature decreasing with r, since $\mu_{ii} \propto nT_i^{-1/2}$), and (b) is the mean azimuthal velocity field computed from ion momentum balance equation with assumed μ_{ii} profiles in (a). The symbols $\star$ are the experimental measurements of the azimuthal velocity. In both figures the black dashed lines indicate the largest positive radial divergence to the angular momentum flux and the red dashed lines indicate the largest negative radial divergence to the angular momentum flux. An examination of $v_\theta(r)$ for the various $\mu_{ii}(r)$ shows that if the ion-ion viscosity is large enough at the location of the largest positive radial divergence to the momentum flux, the ion-ion viscosity drag transfers the azimuthal flow at the shear layer to the central part of the plasma column and generates nearly solid body rotation inside the shear layer. If the ion-ion viscosity is small, then the plasma rotation could be reversed due to the effect of the Reynolds stress. Similar results have recently been found in numerical simulations[72].

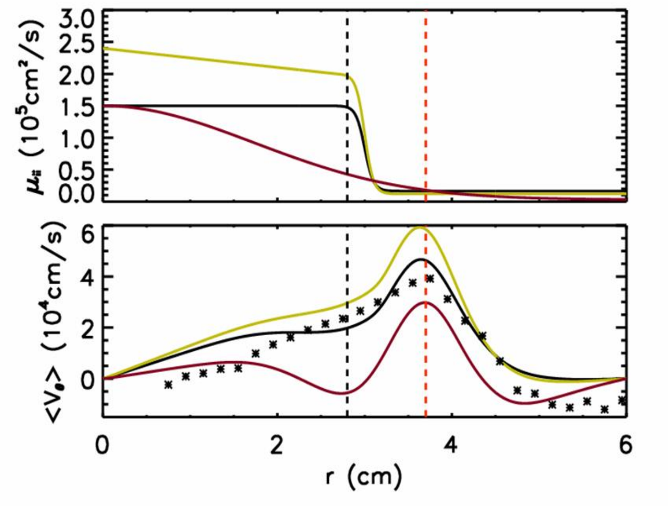

Figure 3.12: (a) Assumed ion-ion viscosity profiles, and (b) mean azimuthal velocity from ion momentum balance analysis.

3.6 Summary

In summary, we have directly measured the Reynolds stress using Langmuir probes in a linear machine and analyzed the data statistically. We found the cross-phase between radial and azimuthal velocity fluctuations is the key factor to determine the shape and the amplitude of the Reynolds stress. The skewness of turbulent Reynolds stress shows a positive peak at $r \sim 3.4$cm, and coincides with positively skewed Isat events. The observations indicate a link between the behavior of the Reynolds stress, its cross-phase and cross-coherence, generation of bursty radially going density and azimuthal momentum transport events, and the formation of the large-scale shear layer.

These results were obtained using an ensemble average approach and thus represent an averaged view of the shear flow generation process. Theory suggests that in fact this generation should exhibit important temporal dynamics. The next chapter will study this topic in details.

3.7 Acknowledgement

The text and data in Chapter 3, in full, is a reprint of the material as it appears in 'The statistical properties of the turbulent Reynolds stress and its link to the shear flow generation', Z.Yan, J.H.Yu, C.Holland, M.Xu, S.H.M$\ddot{u}$ller and George Tynan, Phys. Plasmas, 15, 092309 (2008). Copyright 2008 American Institute of Physics. The dissertation author was the primary investigator and author of this paper.

4

Experimental observation of shear flow dynamics

4.1 Introduction

Heat and particle transport in magnetically confined fusion plasmas is due to turbulent transport driven by pressure gradient-driven instabilities. One of the key issues of the fusion research is to understand the underlying physics of this turbulent transport which results in particle and heat fluxes that are significantly larger than that which results from 'classical transport theory'[73]. The relationship between the fluxes and the mean gradients is of particular interest, since this is what determines to a large degree the system size needed for a positive energy gain. Theory and simulation have both suggested that this flux-gradient relationship is determined by the saturation of drift wave turbulence (DWT) occurring via the generation of linearly damped radially sheared poloidally and toroidally extended plasma flows denoted as zonal flows (ZFs) via the action of the DWT Reynolds stress[9, 8] which acts to nonlinearly transfer turbulence energy into a large-scale damped motion that does not yield transport itself.

The ZFs have been viewed theoretically as being generated by a nonlinear modulation instability in which a small seed shear flow acts to scatter DWT energy into the shear flow itself, resulting in an amplification of the original seed shear and producing a turbulent-driven sheared flow that is denoted as the ZF. The amplification of the ZF then comes at the expense of the DWT energy. Thus as the ZF grows the DWT energy should decrease in this picture. In addition the DWT radial wavenumber is increased due to the random shearing effect of the ZF. If most of the energy goes into the ZF, resulting in smaller DWT energy, eventually the nonlinear drive of the ZF is eliminated. As a result the ZF decays away (via a process that is usually assumed to be linear). The background plasma pressure gradient, which is sustained by a constant external heat input, then leads to the growth of DWT energy and the cycle is then repeated. If cross field transport is interrupted for a significant period of time, the plasma pressure profile can then respond, resulting in a change to the underlying drive of the DWT. Detailed reviews of the theoretical elements of this picture are available in the literature[8, 74]; a summary of the experimental status of the subject is also available[30].

A complete experimental demonstration of the theoretical picture of the above DWT-ZF dynamics requires several simultaneous observations to be made in the same experiment. First, the existence of a radially sheared azimuthal flow must be demonstrated. Second, the shear flow should be sustained by the turbulent Reynolds stress against collisional and viscous damping in order to distinguish it from so-called mean shear flows which are, by definition, sustained by non-turbulence processes such as the return current associated with ion orbit losses[75] or the ion pressure gradient associated with transport barrier formation[25]. This can be done in configuration space by looking at the turbulent momentum conservation equation[59], or in the Fourier domain using bispectral techniques[25, 76]. Third, the ZF shear should be strong enough to reduce the radial correlation length of the turbulent fluctuations, which is a key element in the shear flow dynamics. Finally, the ZF kinetic energy should increase at the expense of the turbulent kinetic energy, while the total kinetic energy is conserved. Qualitatively this could be manifested by an anti-correlation between the high frequency turbulence kinetic energy and the low frequency kinetic energy. Observations of some of these predictions have been reported in the literature[30, 31, 32], but to our knowledge no complete set of such measurements from a single experiment exist.

In this chapter we show that all of these theoretically predicted behaviors indeed occur simultaneously in a simple plasma system that is amenable to the detailed multi-field, multipoint turbulence measurements necessary to examine the fundamental physics of the coupled DWT-ZF system. An azimuthally symmetric shear flow is observed and evolves at a low frequency (~ 250Hz). The mean of this slowly varying shear flow has already been shown to be consistent with the measured turbulent Reynolds stress and estimated linear ZF dissipation profiles[41, 77]. Fluctuation quantities such as floating potential, turbulent Reynolds stress, divergence of the turbulent Reynolds stress, density gradient and the turbulent radial particle flux are all modulated at the same frequency and have the expected phase relationship with the sheared ZF. A detailed analysis of the ion momentum balance equation demonstrates that this slow evolving shear flow is correlated with the variation of the measured turbulence Reynolds stress and estimated damping profiles. The high frequency turbulence kinetic energy and the low-frequency ZF kinetic energy are anti-correlated and a bicoherence analysis shows that the associated potential fluctuations are phase-coherent, and therefore energy can be exchanged between the two scales. An analysis of fast-framing imaging of the plasma emission fluctuations demonstrates the existence of the same slow oscillating shear flow as the probe measurements and shows that when the shear is strong (weak), the radial turbulence correlation length and radial particle transport are both small (large), demonstrating the shearing effect of the zonal flow on the turbulence.

The rest of the chapter is organized as follows: In Section 4.2, we show that the shear flow varies slowly in time and that this slow variation is associated with slow variations in the turbulence statistics. In Section 4.3 we examine the back-reaction of the shear flow on the turbulence and show via direct imaging the essential elements of the shear decorrelation process. In Section 4.4 we discuss the experimental results, and lastly in Section 4.5 we summarize our results.

4.2 Evidences of the slow evolving shear flow

The measurements described in this chapter are made by the 18-tip probe in a plasma condition of 3mTorr gas pressure and 1kG magnetic fields. Fast-framing imaging are also used with the optical set up described in Chapter 2. The frame rate is $97,560$/sec for the 128×64 resolution. A Pentax 25mm f/1.4 lens is used. When capturing images, the probe is out of the plasma.

Previous work has demonstrated the onset of collisional drift waves in the device and has documented transition to a state of weak drift wave turbulence[19] as well as the existence of a time-averaged radially sheared azimuthally symmetric plasma fluid flow at the interface region located between $3.5 - 4$cm which has been shown to be consistent with the experimentally observed turbulent Reynolds stress for reasonable estimates of the collisional ion-ion viscosity[41, 59, 77] - signatures that are consistent with the interpretation of this flow as a zonal flow. In present work we investigate the temporal dynamics of the ZF-DWT system.

The Phantom V7 fast-frame camera is used to capture the visible light emission from the plasma through the telescope. No interference filter is used and thus the measurements integrate over the entire visible spectrum. However, most of the light emission occurs from a combination of neutral Ar-I (750nm) and singly ionized Argon (488 nm) emission. In this work, a total of 24000 ($\sim$ 240ms) frames images are recorded and used in the analysis. The light intensity of the image is somewhat correlated to the plasma density[49] but it is also likely to be influenced by the electron temperature and the neutral density. The detailed relationship between these plasma discharge quantities and the light intensity is currently under investigation and will be discussed in a future publication. Regardless of this fact, we can still gain insight into the turbulence dynamics from the fast-framing imaging.

The azimuthal symmetry of the ZF is best shown by examining images obtained with the fast-framing camera observing the visible light intensity fluctuations associated with the DWT fluctuations[49]. To obtain the intensity fluctuation images we first perform a time average image from 2000 frames, and then subtract this mean image from each frame. Applying the 2D time-delay estimation (TDE) technique described in chapter 2 to a time-sequence of these images, we obtain the 2D time-averaged flowfield in the plane normal to the magnetic field. Here we choose L to be 16 pixels, corresponding to about 2.4cm, and $\Delta\tau$ to be 6μs (the imaging data are interpolated by a factor 10). In computing cross-correlation we use $\sim$1ms time window and then ensemble average all the windows to get averaged cross-correlation function. The result is shown in Fig.4.1 by arrows overlay on the intensity fluctuations. At r$\sim$ 3.6cm the RMS deviation of the azimuthal velocities $v_\theta(\theta)$ is only 11% of the azimuthally averaged $v_\theta(\theta)$ showing that the $m = 0$ component to the azimuthal flow indeed exists and is a dominant component of the azimuthal flow. A previous study shows that this azimuthally averaged flow is due to the combined effect of a mean plasma fluid flow (presumably due to an E×B drift) and the plasma diamagnetic flow[56] and that the mean plasma fluid flow dominates the diamagnetic flow. Thus we take the motion of the fluctuations to represent to lowest order the motion of the plasma fluid in the azimuthal direction.

The radial profile of the time-varying azimuthal flow field is found from 1D TDE technique described in chapter 2. Several radial profiles at different times are shown in Fig.4.2a. The azimuthal flow is found to gradually develop a sheared profile, which then decays back to a flow profile that is close to solid body rotation and then the process re-

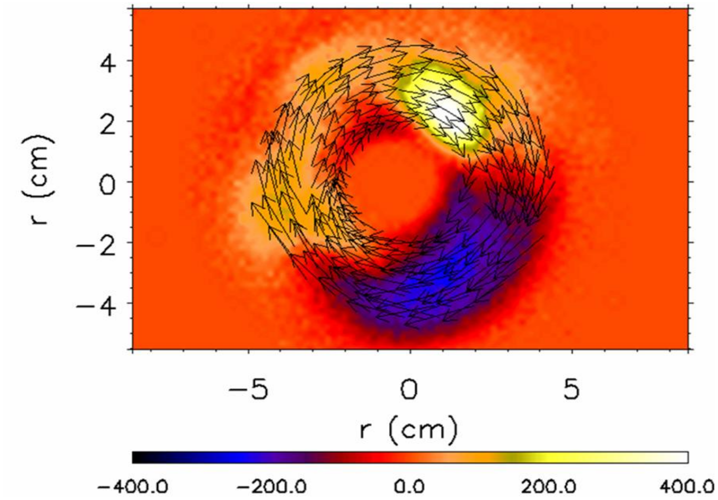

Figure 4.1: 2D flowfield obtained from 2D TDE technique on the fast-framing imaging.

peats. Fig.4.2b shows the time history of the $v_\theta(t)$ obtained at r=3.6cm, illustrating this time variation. A probability distribution function (PDF), computed as the histogram of the $v_\theta(t)$ at r=3.6cm normalized by the time-averaged $v_\theta(t)$, is shown in Fig.4.3. This PDF shows that the most probable velocity is about 80% of the time-averaged $v_\theta(t)$ and the distribution is non-Gaussian and asymmetric over that time average. This suggests that the time-evolving shear flow behaves like a bursty event that remains in the weaker shear flow condition (see Fig.4.2a yellowish line at around 2820μs for example) and then has shorter transient into a stronger shear flow state (see Fig.4.2a red line at around 830μs for example). The frequency spectrum of $v_\theta(t)$ shows that the mean frequency of this oscillation is around 250kHz (Fig.4.4 black solid line); the oscillation is clearly not coherent as the width of the frequency spectrum is also several 100s of Hz. Our previous studies of the shear flow in CSDX and the relationship to the turbulent Reynolds stress[59, 41] used large numbers of statistically independent ensembles and thus those prior results represent a time-averaged view of this slowly oscillating shear flow, and is close to (less than 20% difference) the time-averaged flow field obtained in this experiment from fast-framing imaging, as shown by the red dotted line in Fig.4.2a

The earlier results showed that the time-averaged shear flow was consistent with the time-averaged Reynolds stress and estimated flow damping profiles,suggesting a strong link between the turbulence and the shear flow. Thus the question arises: How does the slow variation in the shear flow affect the turbulence? In order to address this question, the time-varying azimuthal velocity field is also measured with two azimuthally separated probe tips (separation distance of 5mm) measuring floating potential also by using the TDE technique[56] with a serial of overlapping time windows each being ~ 1ms. The frequency spectrum of the time-varying shear flow measured with the probe is shown in Fig.4.4 as red dot-dash line. Again, the shear flow is found to varying with a low frequency of about 250Hz and has a frequency width also in the order of 100Hz, consistent with the results obtained with the fast imaging.

To investigate if the turbulence statistics are also modulated at the same frequency, we look at the envelopes of the fluctuation quantities, such as fluctuation floating potential, turbulent Reynolds stress, divergence of the turbulent Reynolds stress, density gradient and the turbulent radial particle flux, obtained by applying a high pass digital filter (using a 5kHz cutoff frequency) to each instantaneous fluctuating quantity measured by the multi-tip probe array, and then taking the square of the filtered result. The envelopes are found by applying a smoothing function with a ~ 1ms time window. Fig.4.5a shows

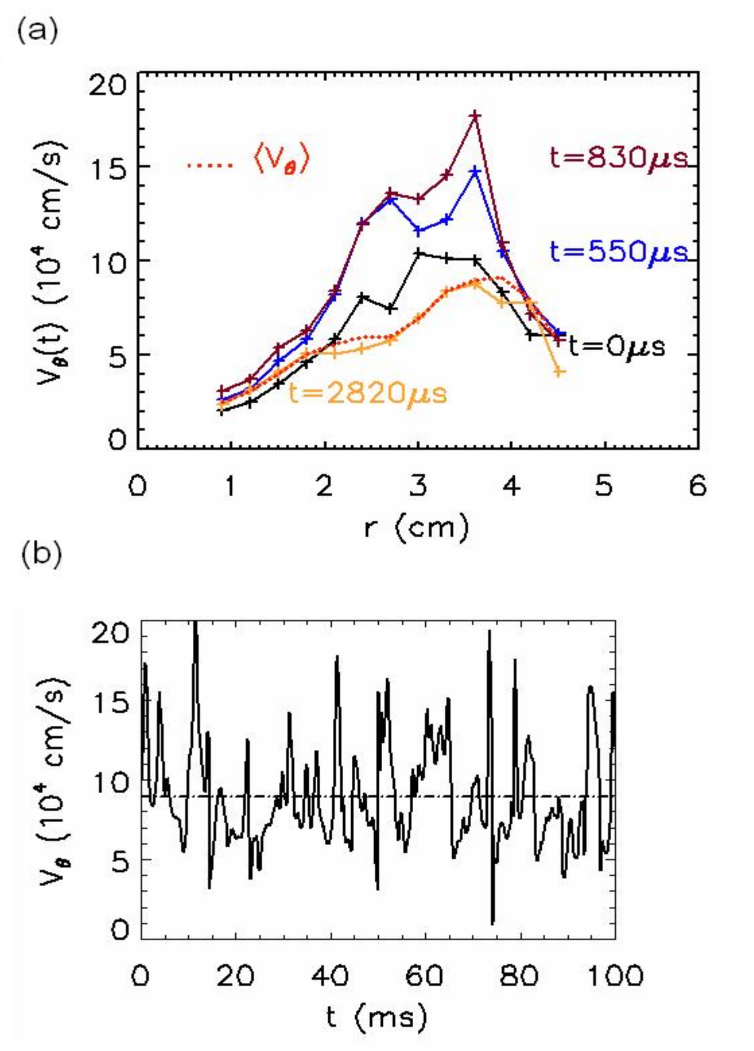

Figure 4.2: (a) Radial profiles of azimuthal flow obtained from azimuthally averaging the visible light TDE flowfield for different observation times. A radially sheared flow is observed to grow and decay with a period of ~ 4msec. (b) Time varying azimuthal flow field at r~ 3.6cm

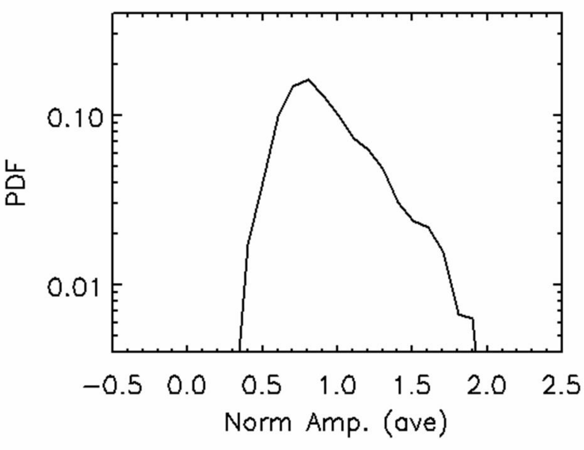

Figure 4.3: PDF of the $v_\theta(t)$ at r$\sim$ 3.6cm. (Normalized by the time-averaged $v_\theta(t)$).(log 10).

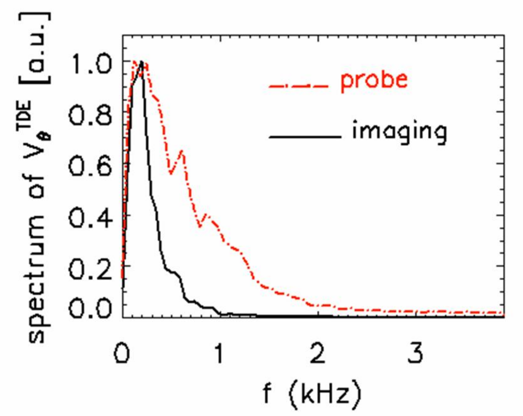

Figure 4.4: Spectrum of the time varying azimuthal velocity field at the shear location (r=3.6cm) from visible light velocimetry (black solid line) and from Langmuir probe measurements (red dot-dashed solid line).

the square of the fluctuating floating potential, turbulent Reynolds stress, divergence of the turbulent Reynolds stress, the turbulent radial particle flux and density gradient, as well as their envelopes, which are shown as the colored line on each panel. A spectral analysis of these envelopes demonstrates that they are all modulated with the same frequency as the shear flow evolution (Fig.4.5b). A similar result is obtained for 0.5msed smoothing window indicating that this result is insensitive to the choice of the smoothing window duration. The red dot-dash line on the panels in Fig.4.5b is the spectrum of the azimuthal velocity field obtained from the probe TDE measurement. Clearly the fluctuating envelopes exhibit temporal evolutions that are nearly identical to that of the slowly varying sheared flow. To further look at the modulation effect of the shear flow we compute the cross-correlation between envelopes of the density gradient, floating potential fluctuations, particle flux and the flow velocity at shear layer (~ 3.6cm) respectively for 2s duration data, as shown in Fig.4.6. In all cases, we find that there are finite anti-correlations between these turbulence quantities and the shear flow. The values are above the statistical significant value, and show that the high frequency DWT fluctuations are modulated out of phase with the ZF.

Keeping in mind our previous results linking the time-averaged shear flow and the time-averaged Reynolds stress, these results suggest that the variation in fluctuations may cause a slowly varying Reynolds stress which can in turn be linked with the slowly varying sheared flow. Therefore, to test this possibility and investigate the modulation of the turbulent Reynolds stress with ZF, we next consider the turbulent momentum balance equation.

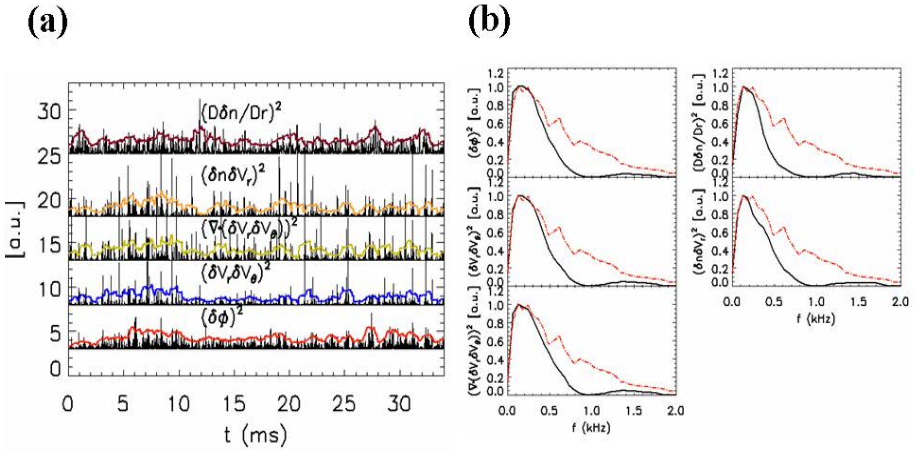

Figure 4.5: (a) Square of the turbulent floating potential, turbulent Reynolds stress, divergence of the turbulent Reynolds stress, density gradient and turbulent radial particle flux and their envelopes. (b) Spectrums of the envelopes of the turbulent floating potential, turbulent Reynolds stress, divergence of the turbulent Reynolds stress, density gradient and turbulent radial particle flux. The red dot-dashed line on each figure is the spectrum of the azimuthal velocity field.

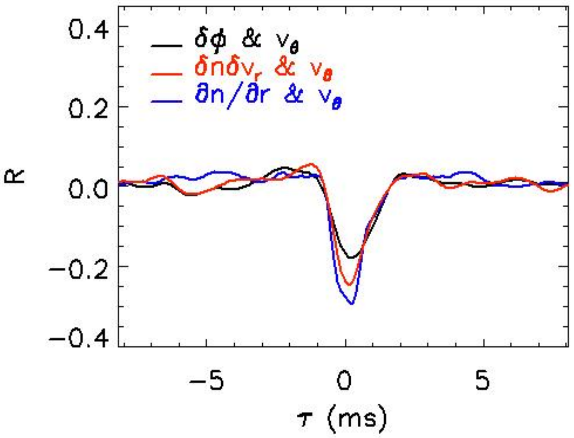

Figure 4.6: Cross-correlation between envelops of floating potential (black solid line), density gradient (blue solid line), particle flux (red solid line) and flow velocity at shear layer.

For the collisional plasmas found in these experiments, the azimuthal component of the ion momentum equation is[41] :

$$\frac{\partial v_\theta}{\partial t}+v_r\frac{\partial v_\theta}{\partial r}+\frac{v_\theta}{r}\frac{\partial v_\theta}{\partial \theta}+v_z\frac{\partial v_\theta}{\partial z}+\frac{v_r v_\theta}{r}=\frac{e}{M_i}(E_\theta-v_rB)-\nu_{i-n}v_\theta+\mu_{ii}(\nabla^2 v_\theta+\frac{2}{r^2}\frac{\partial v_r}{\partial \theta}-\frac{v_\theta}{r^2}) \tag{4.1}$$

where ν_{i-n} is ion neutral collision rate and μ_{ii} is the ion viscosity and where we assume neutrals have negligible velocity, ion pressure fluctuation is negligible since the ion temperature is low (~ 0.5eV) and the velocity fluctuations are incompressible. Our observations show that the plasma rotates once azimuthally in about 0.5msec, while the time scale of the azimuthal velocity oscillation is approximately 4 msec (corresponding to the 250Hz frequency above). We therefore chose an intermediate timescale of 1 msec over which we average this equation. This choice will average over the mode number m 0 turbulence, but will still resolve the more slowly varying sheared azimuthal flow.

Introducing the fluctuating radial and azimuthal velocities $\tilde{v}_r$ and $\tilde{v}_\theta$, and denoting the azimuthal flow that survives the time averaging operation as $\langle v_\theta \rangle_t$, the turbulent momentum conservation equation can then be reduced to:

$$\frac{\partial \langle v_\theta \rangle_t}{\partial t} + \frac{1}{r^2}\frac{\partial}{\partial r}(r^2 \langle \widetilde{v}_r \widetilde{v}_\theta \rangle_t) = -\nu_{i-n} \langle v_\theta \rangle_t + \mu_{ii}(\frac{\partial^2 \langle v_\theta \rangle_t}{\partial r^2} + \frac{1}{r}\frac{\partial \langle v_\theta \rangle_t}{\partial r} - \frac{\langle v_\theta \rangle_t}{r^2}) \tag{4.2}$$

where, $\langle \rangle_t$ denotes 1ms time window average. A detailed derivation can be found in Ref.[41]. For simplicity, and since no other measurements are available, the dissipation coefficients ν_{in} and μ_{ii} are assumed to be time stationary and to have values similar to those reported earlier[59]. From the multi-tip Langmuir probe the slow (1msec) variation of the turbulent Reynolds stress and the azimuthal velocity field from TDE technique at shear location ($\sim$ 3.6cm) are calculated. Both quantities are averaged over 1 msec time window allowing a comparison of the inertial term $L(t) = \frac{\partial \langle v_\theta \rangle_t}{\partial t} + \frac{1}{r^2}\frac{\partial}{\partial r}(r^2 \langle \widetilde{v}_r \widetilde{v}_\theta \rangle_t)$ and the force due to dissipation $R(t) = -\nu_{i-n} \langle v_\theta \rangle_t + \mu_{ii}(\frac{\partial^2 \langle v_\theta \rangle_t}{\partial r^2} + \frac{1}{r}\frac{\partial \langle v_\theta \rangle_t}{\partial r} - \frac{\langle v_\theta \rangle_t}{r^2})$. Fig.4.7a shows the time traces of of $L(t)$ and $R(t)$ obtained in this manner. There are clearly some instances when the two sides of the momentum balance have a similar time variation, while at other times there appears to be little relationship between the two time series. The cross-correlation between $L(t)$ and $R(t)$ allows the statistical relationship to be better quantified. The result (Fig.4.7b), which is computed independently from probe measured Reynolds stress and the azimuthal velocity fields, has a finite in-phase correlation of around $0.3 - 0.4$, a value that is well above the statistical significant level of ~ 0.05. Although this peak value is lower than expected value $\sim$1 (probably due to the combined errors arising from the use of floating potential in place of plasma potential, the error associated with the finite differencing of the spatial gradients, and the assumption that the dissipation rates are fixed), the results show that there is clear in-phase variation between the slow evolving shear flow and slowly evolving turbulent Reynolds stress against the collisional and viscous damping, qualitatively consistent with earlier results showing that the time-averaged shear flow is maintained against flow damping by the turbulent Reynolds stress.

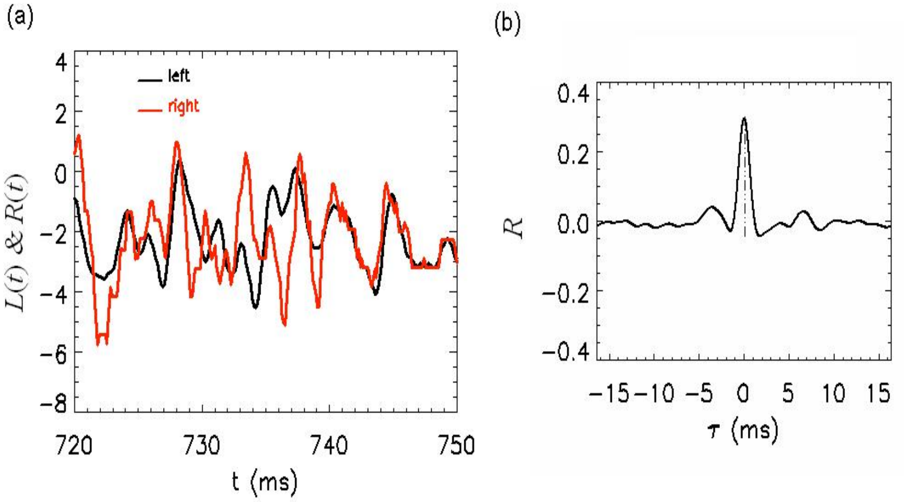

Figure 4.7: (a) Time traces of the left hand side of the ion momentum equation (black) and the right hand side of the ion momentum equation (red). (b) Cross-correlation between the left and right hand side of the momentum equation.

We further illustrate the relationship between the slowly varing shear flow and the turbulence by examining the auto-bicoherence of floating potential fluctuation, which provides a measure of the phase coherence between fluctuations at two frequencies f and

f_1 and which is defined as[57],

$$\hat{b}^2_{XXX}(f, f_1) = \frac{\left|\hat{S}_{XXX}(f_1, f_2)\right|^2}{\frac{1}{M}\sum_{k=1}^{M}\left|X^{(k)}(f)\right|^2 \frac{1}{M}\sum_{k=1}^{M}\left|X^{(k)}(f_1)X^{(k)}(f_2)\right|^2} \tag{4.3}$$

where, $\hat{S}_{XXX}(f_1, f_2)$ is the bispectrum of floating potential fluctuations, defined as,

$$\hat{S}_{XXX}(f_1, f_2) \equiv E\left[X(f)X^{\star}(f_1)X^{\star}(f_2)\right] = \frac{1}{M}\sum_{k=1}^{M} X^{(k)}(f)X^{\star(k)}(f_1)X^{\star(k)}(f_2) \tag{4.4}$$

In the above equations (k) indicates the k^{th} realization, M is the total number of realizations and the symbol $\star$ denotes a complex conjugate. Fig.4.8a shows the bicoherence $b^2(f = 300Hz, f_1)$with $f = f_1 + f_2 = 300$Hz (which corresponds to the slow variation of the shear flow). This result shows that the slowly varying ZF is nonlinearly coupled to other frequencies, which can be identified by examining $b^2(f, f_1)$ shown in Fig.4.8b. It is clear that the low frequency ZF is coupled with fluctuations with frequencies in the range of $\sim$ 5kHz up to $\sim$ 11kHz; the coupling with fluctuations near 10kHz appears to be particularly strong. These frequency range have been previously identified as drift wave turbulent fluctuations[19]. Thus energy is clearly exchanged between DWT and the ZF. A detailed measure of the nonlinear energy transfer between the different frequency ranges using cross-bispectral analysis with a two-field model of the fluctuations is underway and will be reported in another paper[78].

Additional evidence showing a link between the time-varying ZF and the turbulence comes from examining the relationship between the turbulence kinetic energy and the ZF kinetic energy in the time domain. However, this comparison is complicated by the results above which show that the density gradient is modulated. Since this gradient is the

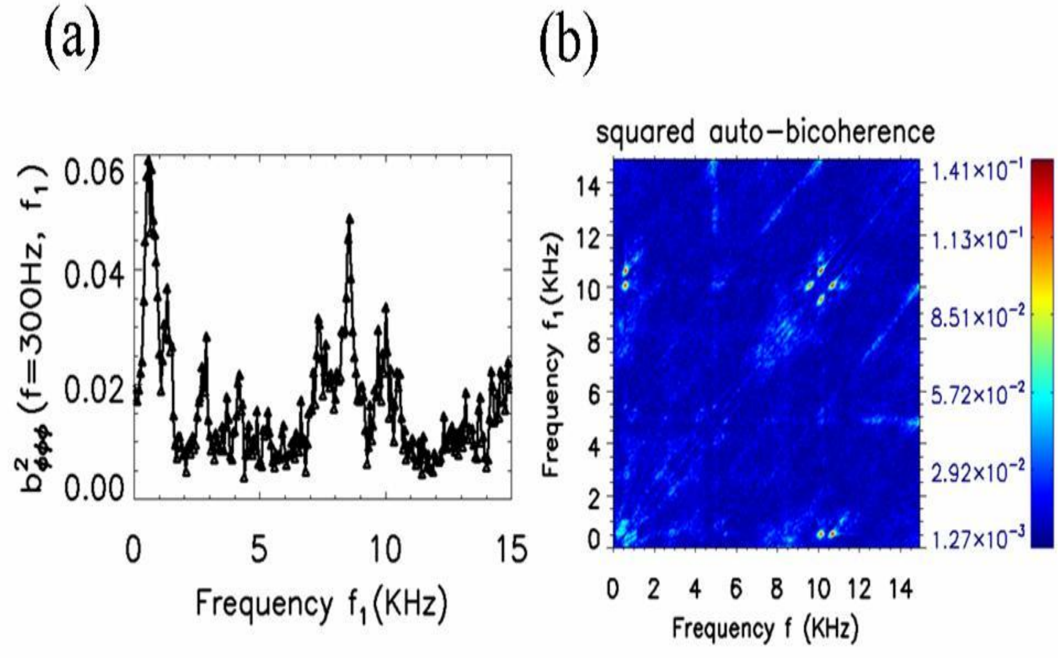

Figure 4.8: (a) Auto-bicoherence of the floating potential fluctuations at r$\sim$ 3.6cm for f = 300Hz. (b) 2D plot of the auto-bicoherence of the floating potential fluctuations at r$\sim$ 3.6cm.

principle drive behind the DWT, the resulting energy contained in the DWT can vary due simply to this change in linear drive since the estimated growth rates are sufficiently fast for the DWT amplitude to increase during one oscillation of the ZF. To account for this effect, we examine the variation in the fluctuating ZF and DWT energy normalized to the total fluctuating energy[79] to study the exchange of energy between the DWT and ZF range of frequencies. Here, the normalized power is defined as $S_{f_{low}}^{f_{high}} = \frac{\int_{f_{low}}^{f_{high}} P(f)\, df}{\int_{0}^{\infty} P(f)\, df}$,Where P(f) is the sum of the radial and azimuthal electric field spectra. The ZF frequency range is taken to be 0 to 2kHz, while the DWT frequency range is taken to be 5kHz to Nyquist frequency 250kHz. Fig.4.9a shows the normalized powers fractions $S_{f_{low}}^{f_{high}}$ of three different frequency ranges ($5 - 250$kHz, $2 - 5$kHz and $0 - 2$kHz). And Fig.4.9b and 4.9c is the cross correlation between high frequency range ($5 - 250$kHz) with low frequency range ($0 - 2$kHz), and intermediate frequency range ($2 - 5$kHz) with low frequency range ($0 - 2$kHz) respectively. It is found there is a high anti-correlation between the high frequency turbulence and the low frequency range, while there is no significant correlation between the intermediate frequency range and the low frequency range. This suggests a direct energy exchange between fluctuations of high frequency and low frequency ranges, qualitatively consistent with an exchange of energy between the DWT kinetic energy and ZF energy. Similar results are also reported in the literature [79]. We note that by doing normalization we force the total energy to be constant and this may overemphasize the correlation between the high frequency and low frequency ranges. We have repeated this analysis without this normalization (and thereby ignoring the effect of the change in mean gradient) and find a cross- correlation of -0.3 peaking at zero-time delay for the ZF-DWT case, consistent with an anti-phased relationship between these two spectral components.

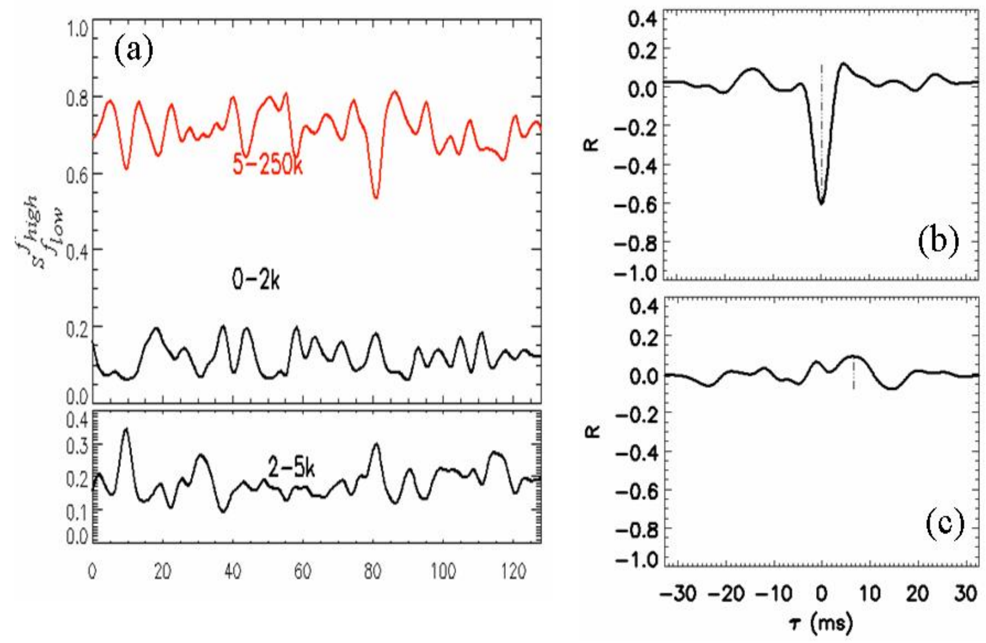

Figure 4.9: (a) Time-varying DWT kinetic energy in different frequency ranges, $5 - 250$kHz, $2 - 5$kHz and $0 - 2$kHz. (b) Cross-correlation between high frequency kinetic energy ($5 - 250$kHz) and low frequency kinetic energy ($0 - 2$kHz). (c) Cross-correlation between intermediate frequency range ($2 - 5$kHz) and low frequency range ($0 - 2$kHz) kinetic energy.

4.3 Effect of shear flow back on the turbulence from fast-framing imaging

The effect of the ZF on the scale lengths of the DWT is also of interest since at the end of the day it is this effect that impaches the energy transport across the pressure gradient. This process can be visualized by selecting a sequence of fast-framing images obtained in both the strong shear case and the weak shear case. A representative example is shown in Fig.4.10a and Fig.4.10b, which provide two sets of four consecutive images of the density fluctuation with time interval 20μs for strong shear case (the case shown in Fig.4.2a by the red line, which is around 830μs) and weak shear case (the case shown in Fig.4.2a by the yellowish line, which is around 2820μs) respectively. It is found that for the strong shear case (Fig.4.10a) the positive visible light perturbation, which is highlighted by a green ellipse, is formed near the density gradient maximum (indicated by the dashed blue lines) and moves outward radially and azimuthally in the clockwise direction. As it approaches the shear layer (indicated by the dashed black lines) the structure is distorted in the azimuthal direction and eventually becomes highly elongated azimuthally. The radial scale length of the structure is reduced from $\sim$ 2cm to less than $\sim$ 1cm. On the contrary for the weak shear case (Fig.4.10b) the positive visible light perturbation is not distorted during the radial and azimuthal propagations, as a result there is no observable reduction of the radial scale length. This phenomenon suggests a time varying shearing of the turbulent structure by the shear flow and provides the first direct visualization of this important process. For the typical conditions of our experiment we find the turbulence correlation time τ_c is $\sim\ 50\mu$s, so the turbulence decorrelation rate, $\omega_\tau\ =\ \frac{1}{\tau_c}$, is $\sim\ 2\times 10^4 1/s$. In the strong shear case the shearing rate defined as $\omega_s\ =\ r\frac{d}{dr}(\frac{v_\theta}{r})$ at r$\sim$ 3.6cm is estimated to be $\sim 4\times 10^4 1/s$, and for the weak shear case the shearing rate is estimated to be $\sim 0.7\times 10^4 1/s$. Therefore in the strong shear case the shear flow satisfies $\omega_s > \omega_T$, sufficient to have impact on the turbulence[27], while for the weak shear case, $\omega_s < \omega_T$ and thus can not effectively decorrelate the turbulence, and that when the shear is strong (weak), the radial scale length of the turbulent structure is small (large).

We can also statistically test the shearing effect by using the imaging data to compute the time varying radial correlation length from a long series of images obatined at $\sim$ 100kHz framing rate over a period of 240ms. The radial turbulence correlation length at any point in time is obtained by computing the cross correlation (using $\sim$1ms time window) between the fluctuating intensity as a function of the radial separation between a reference point located at $r\ =\ 3.6$ cm and a second point located at a variable radial separation. The cross-correlation function envelope is then used to find the correlation length, defined as the location where the envelope is down by a factor of $1/e$ from the peak value at zero spatial separation. This correlation length then varies slowly in time, and this variation can then be cross-correlated with the time variation of the shearing rate. Fig.4.11 shows the result for data obtained at r$\sim$ 3.6cm which is the shear layer location. We find that there is a finite anti-correlation lying outside the noise level confirming that the the radial turbulent correlation length is related to the shearing rate, qualitatively consistent with the theoretical picture of the random shearing effect of the shear flow on the

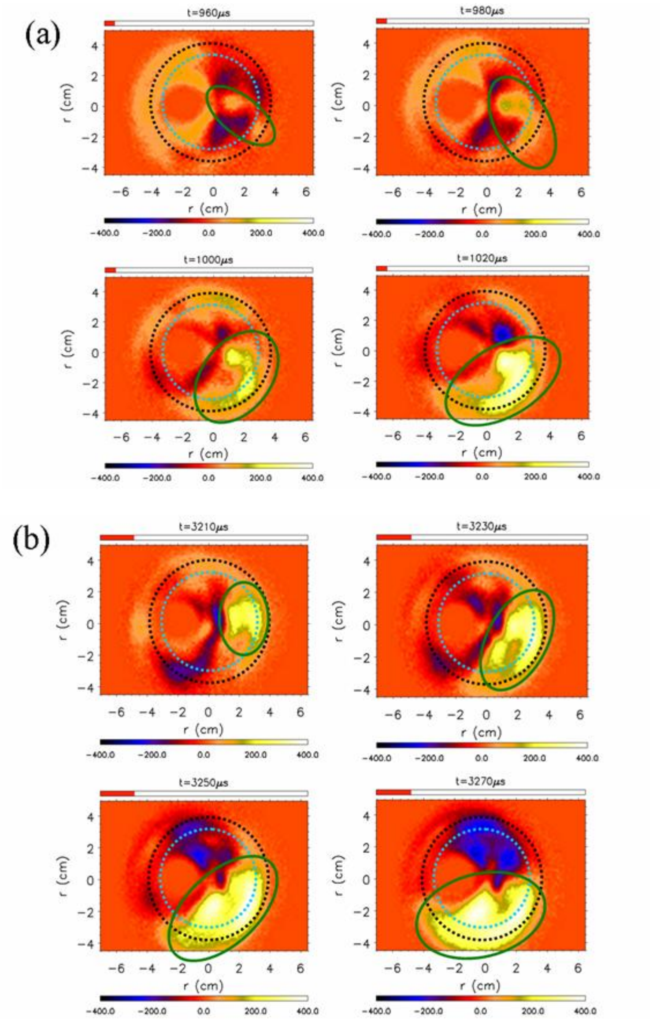

Figure 4.10: (a) Snap shots of the four consecutive density fluctuation images with 20μs time interval for strong shear case. (b) Snap shots of the four consecutive density fluctuation images with 20μs time interval for weak shear case. Black dashed line indicates the peak shear location, blue dashed line indicates the maximal density gradient location and the green solid ellipse indicates the positive visible light perturbation structure.

turbulence[8].

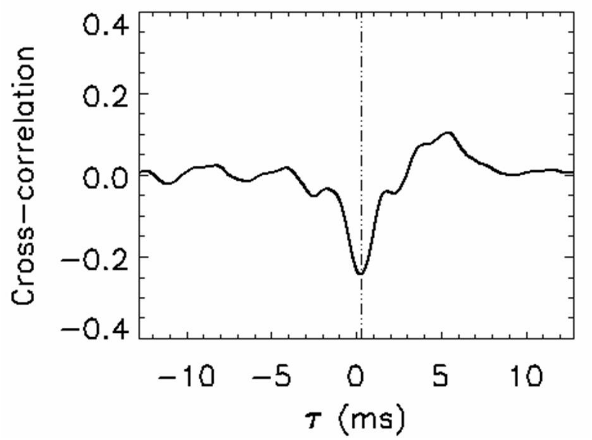

Figure 4.11: Cross-correlation between the azimuthal velocity shear and the radial turbulence correlation length at shear location r$\sim$ 3.6cm.

4.4 Discussion

The above results demonstrate all of the essential elements of the theoretically predicted ZF-DWT dynamics. An existence of the slowly varying azimuthally symmetric ZF has been demonstrated from both probe-based measurements and fast-framing imaging. Such flow lies at the bottom or foot of the steep pressure gradient, and that this region is determined by the radius of the heat input into the system (which is the source size). The slowly varying ZF modulates the high frequency floating potential associated with DWT, density gradient and cross-field transport. A strong anti-correlation is found between normalized DWT kinetic energy (5-250kHz) and the ZF energy (0-2kHz), but not between the intermediate frequency range (2-5kHz) and ZF. This suggests a direct energy exchange between DWT and ZF. The results shown here are qualitatively consistent with the theory of the modulation instability in which a small shear flow scatters energy from turbulence into the shear flow resulting in amplification of the shear flow while the total energy is conserved. However, thus picture is complicated by the fact that the density gradient also increases as the turbulence is damped by the shear flow, resulting in an increase in the turbulence drive. Such an increased drive is neglected in current theoretical models. The momentum balance analysis shows that this energy exchange is mediated by the turbulent Reynolds stress. This exchange is also observed in the frequency domain by a bicoherence analysis of the DWT and ZF. Fast-framing imaging has also shown an existence of the strong and weak shear flow and found that when the shear flow is strong, the radial correlation length is small, and vise verse. The imaging also directly demonstrates that the ZF can shear apart and decorrelate the DWT structures that move into the ZF, which is also qualitatively consistent with turbulent decorrelation process.

It is also interesting to note that the imaging data show a dominant $m = 1$ intensity emission pattern when the shearing is weak, while the fluctuations have smaller spatial scales in periods with stronger flow shear. In previous work[49, 80] such $m = 1$ flow patterns have been found to be associated with the formation of blobs or intermittent edge transport events in which a burst of dense plasma breaks off from the central plasma region and propagates outwards into the low density halo region surrounding the main plasma column. The results reported here suggest that the shear flow dynamics may be linked to the birth of such intermittent transport events. A detailed study is needed to determine if indeed this is the case.

4.5 Summary

In summary we have presented experimental results that are qualitatively consistent with the theoretic picture of the DWT/ZF dynamics. The slowly evolving ZFs are found to exist modulate plasma turbulence and resultant transport. ZFs can shear turbulent eddies and reduce the radial correlation length. Energy is exchanged between DWT and ZF and is mediated by the slowly varying turbulent Reynolds stress. Therefore the experimental results support the theoretical expectation of the DWT-ZF dynamics. Future work will be focused on studying the nonlinear energy transfer from DWT to the ZF by bispectral analysis from two-field model in the frequency domain, which will be an additional important evidence of the ZF generation from DWT.

5

Scaling properties of turbulence driven shear flow

5.1 Introduction

In Chapter 3, the detailed spatial variation of the turbulence statistics was examined. Those results showed that the cross-phase between the turbulent radial and azimuthal velocity fluctuations played a key role in determining the shape of the Reynolds stress profile. Since the shape is related to the time-averaged momentum balance through the divergence of the Reynolds stress, this cross-phase thus plays a key role in setting the conditions for the generation of the time-averaged shear flow. In Chapter 4, the temporal dynamics of this shear layer were studied in detail. The results showed that the shear layer in fact exhibits slow ($\sim 200-300$ Hz) variations, and that these variations are linked to corresponding changes in the turbulence amplitudes, cross-field particle transport, and plasma density gradient- observations which are consistent with theoretical expectations.

These previous results were all obtained well above the threshold for the onset of drift wave turbulence, i.e., at 1000G magnetic field. Previous results[19] have shown that the magnetic field strength is an important control parameter governing the development of drift turbulence. As the magnetic field was increased from 400G to 1000G the plasma drift wave fluctuations evolve from narrow-band (i.e. frequency width much smaller than the wave frequency) coherent wave-like perturbations that were consistent with collisional drift turbulence linear eigenmodes into a state of weak drift turbulence that was characterized by broad frequency and wave number spectra that still roughly follow the linear dispersion relation (and hence these fluctuations were characterized as being in a state of weak turbulence). The role of the magnetic field acting as a control parameter for the transition to drift turbulence has also reported in other literatures[81, 82]. This effect is attributed to the reduction of ion-ion collisional viscosity $\mu_{ii} \propto \rho_i^2 \nu_{ii} \propto \frac{1}{B^2}$ that occurs at higher magnetic fields. As the viscosity is reduced the convective derivative, and hence the nonlinear interactions that are mediated by it, becomes more prominent in the fluid conservation equations[19] in a manner analogous to the transition to turbulence that occurs in neutral turbulence when the Reynolds number is increased. Given these earlier results, and the observations that the turbulence and zonal flows form a nonlinearly coupled system, the question naturally arises: how does this coupled system evolve as the magnetic field is increased? The neutral gas pressure has also been used to control the transition to turbulence[43, 44]. Ion-neutral drag due to collisions between these species can also act to damp out turbulent-driven shear flows[59] in a process that is analogous to the damping of zonal flows in toroidal devices due to collisions between trapped and passing ions[10], and is thus of fundamental interest as well. Therefore it would be very interesting to study how the shear flow and its generation change when the flow damping is also changed.

There is no straightforward way to study the scaling properties of the shear flow generation with magnetic field or flow damping in larger confinement devices, and thus the experiments discussed here provide the first such experimental study of the onset of turbulent-driven shear flows in plasmas, as well as the first controlled study of the effect of flow damping on these flows.

The rest of the Chapter is organized as follows: In Sec. 5.2 we discuss the magnetic field scaling properties of the turbulence driven shear flow. In Sec. 5.3 we discuss the pressure scaling properties of the turbulence driven shear flow. Lastly in Sec. 5.4 we discuss and conclude our experimental results.

5.2 Magnetic field scaling of the turbulence driven shear flow

The experiments presented here are carried on the CSDX device that has been described elsewhere[19, 45]. A dual 3×3 array of Langmuir probes is used to measure the plasma density and floating pressure at several radial locations for various magnetic fields and plasma pressure conditions. A detailed description of this probe can be found in Chapter 2. A two-point time delay estimation (TDE) technique is applied to the density fluctuation measurements to obtain a radial profile of the azimuthal velocity fields.

Fig.5.1 provides a plot of time-averaged plasma density for different magnetic fields obtained from the ion saturation current measurements, while Fig.5.2 provides the density fluctuation amplitude and radial particle flux near the density maximal gradient location (r=3cm). All the data are taken at an Argon fill pressure of 3.18mTorr and a source power input of 1.5kW. The density fluctuations and radial particle flux are all normalized by the corresponding values at 1000G magnetic field. The results show that plasma time-averaged density gradient increases slightly as the magnetic field is increased, but that this gradient increase appears to saturate once the magnetic field exceeds ∼700-800G. The density fluctuation amplitude and the radial particle flux both become significant once the magnetic field exceeds ∼600G, and they rapidly increase as the magnetic field is increased towards 1000G, consistent with previous results[19].

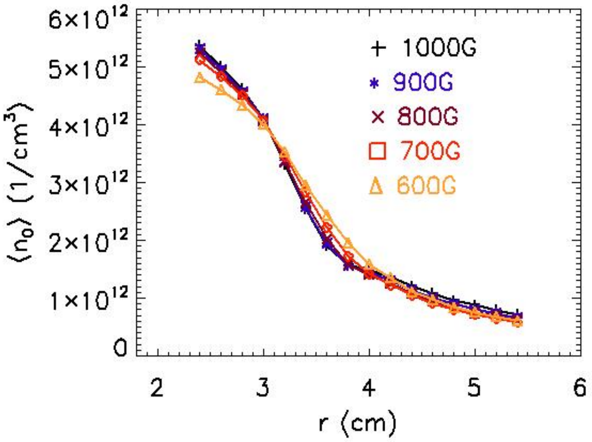

Figure 5.1: Equilibrium plasma density profile for different magnetic fields.

Fig.5.3 shows the time-averaged radial profile of the azimuthal velocity, which is

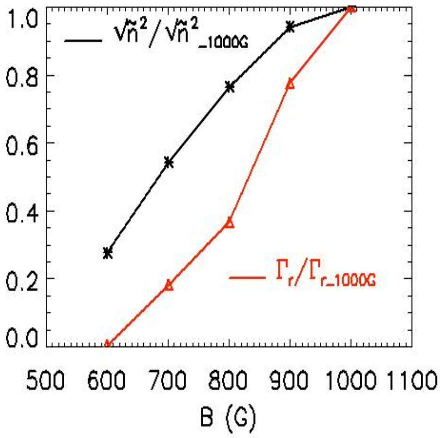

Figure 5.2: Density fluctuation amplitude (black solid line and symbol $\star$) and radial particle flux (red solid line and symbol Δ) at 3.18mTorr for different magnetic fields. Each is normalized by the corresponding value at 1000G magnetic field.

averaged over the slowly varying results discussed in Chapter 4 in a 3.18mTorr 1.5kW Argon discharge at five different magnetic fields. Fig.5.3b is the shearing rate at $r = 3.8$cm at different magnetic fields. The result shows that shear flow exists when the magnetic field $B \geq 700$G, while for lower magnetic fields (600G is shown in the figure) the fluctuations propagate close to solid body rotation. The power spectra of both ion saturation current and floating potential fluctuations obtained at the shear layer ($r = 3.8$cm) are shown in Fig.5.4, with dashed line indicating the density fluctuation spectrum and solid line indicating floating potential fluctuation spectrum. Several features are of note. First, note that as the magnetic field is raised, the low frequency (<2kHz) potential fluctuation power increases substantially. We interpret this as representing the onset of the slowly varying shear flow that was documented in Chapter 4. Second, as the magnetic field begins to exceed 700G, a new set of fluctuations in the frequency range of $\sim$7-8kHz appear. As the magnetic field is raised to 1000G these fluctuations move up to $\sim$9-10kHz. As was shown in the bicoherence analysis of Chapter 4, at 1000G it is this frequency range that is most strongly coupled to the slowly varying shear flow. Comparing with the results shown in Fig.5.3, and keeping in mind the results from Chapter 4 that showed a slow variation in the shear flow and also a strong phase coherent coupling between this low frequency flow and the drift wave fluctuations at $\sim$10kHz, these observations suggest that the onset of the shear flow is related to the development of the $\sim$7-8kHz fluctuations at B$\sim$700G and then the subsequent evolution of those fluctuations to $\sim$9-10kHz as the magnetic field is raised to B$\sim$1000G. The amplitude of the low frequency floating potential oscillation, which is consistent with the slow varying shear flow, is also proportional to the magnetic field. Taken together, these results indicate that as the magnetic field is increased, the drift wave turbulence amplitude increases, the nonlinear coupling into the shear flow increases, and strength of the shear flow increases. This scaling is qualitatively consistent with the theoretical picture of turbulence driven shear flow that is summarized in the literature[8]. We also note that we do not see the 'Quasi-coherent' mode at $\sim$700G as was reported in the previous work of Burin[19], and the most prominent frequency of both density and floating potential fluctuations is below 15kHz, not as high as 30kHz reported in that work. The difference is likely due to a change in end-plate boundary conditions caused by the removal of the concentric conducting end rings between the time of those earlier experiments and the current work.

If the shear flow is driven by the fluctuations, as suggested by the above results,

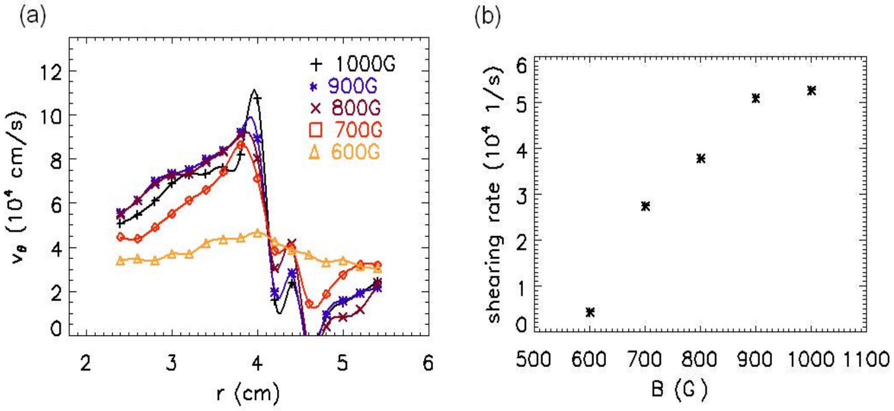

Figure 5.3: Time-averaged azimuthal velocity fields for different magnetic fields.

then the divergence of the turbulent Reynolds stress should also be small or zero for B<700G, and then should increase once the magnetic field exceeds this threshold. In particular, from theory and previous experimental studies for the statistical properties of the turbulent Reynolds stress discussed in the Chapter 3 we know that the negative divergence of turbulence Reynolds stress ($\nabla \cdot (\tilde{v}_r\tilde{v}_\theta)$) will reinforce shear flow. Therefore it would be interesting to look at the evolution of $\nabla \cdot (\tilde{v}_r\tilde{v}_\theta)$ with magnetic fields. In Fig.5.5 the symbols $\star$ are the absolute values of the $\nabla \cdot (\tilde{v}_r\tilde{v}_\theta)$ at shear layer (~3.8cm) for different magnetic fields. The results show that the amplitude of the $\nabla \cdot (\tilde{v}_r\tilde{v}_\theta)$ is small at 600G and then increases with magnetic field consistent with expectations. We also note that at low magnetic field as 600G, there is a finite divergence of the turbulent Reynolds stress, but there is no shear flow at that condition. This discrepancy may because that ion-gyro frequency is small when the magnetic field is small, thus the ion-ion collision

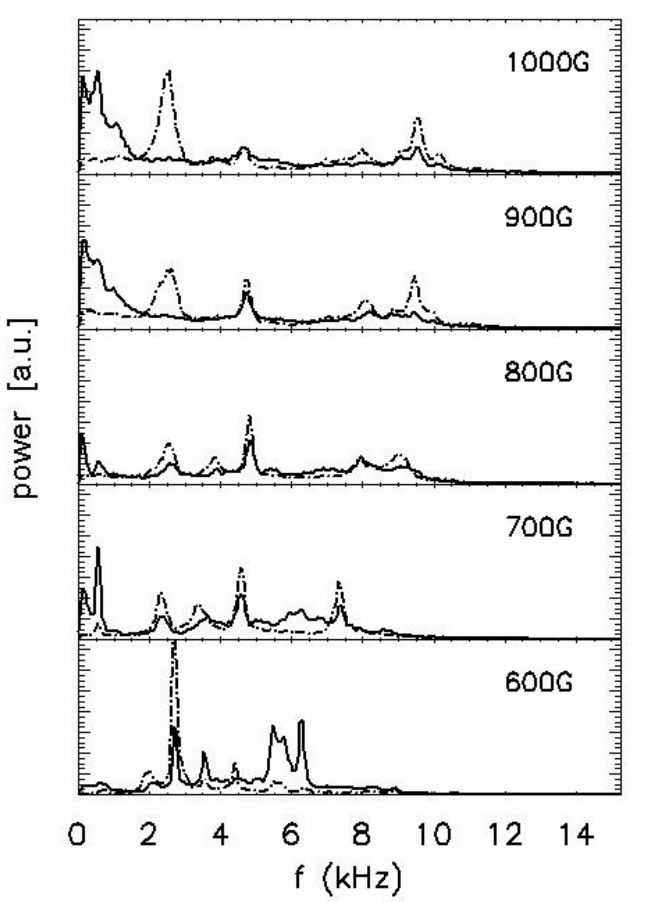

Figure 5.4: Power spectra of density fluctuations (dashed line) and floating potential (solid line) at shear layer (~ 3.8cm), 3.18mTorr, for different magnetic fields.

rate will be comparable with the ion-gyro frequency thereby invalidating the assumption of $\vec{E} \times \vec{B}$ dominated guiding center drifts.

In Chapter 3 we have known that the cross-phase between the radial and azimuthal components of the velocity field is a key factor to determine the detailed turbulent Reynolds stress and hence the shear flow generation. We have also investigated the evolution of the cross-phase with magnetic field to determine if this statistic governs the variations of the turbulent Reynolds stress with magnetic fields. Fig.5.6a shows the radial profile of the turbulent Reynolds stress computed in the frequency domain using Eqn.2.13. As the magnetic field is increased, the negative divergence of the Reynolds stress needed to drive the shear slow increases in the region 3.5cm<r<4cm, which is precisely the location of the shear flow development. Using an approach similar to that described in detail in Chapter 3, an examination of the role of the velocity cross-phase (Fig.5.6(b-c)) shows that the Reynolds stress divergence is determined primarily by the evolution of the turbulent velocity cross phase. In particular, we note that when the cross-phase is excluded from the turbulent Reynolds stress (Fig.5.6c), there is much less variation near the shear layer. Our results therefore show that the turbulent velocity cross-phase determines the variation of the turbulent Reynolds stress and is influenced by the strength of the magnetic field.

Magnetic field scaling properties of the ion momentum balance equation are also of interest, and can demonstrate if the theory that the shear flow is driven by turbulence is valid for different plasma conditions. In order to estimate the ion viscosity and ion-neutral flow drag, it is necessary to measure ion and neutral temperatures. Previously

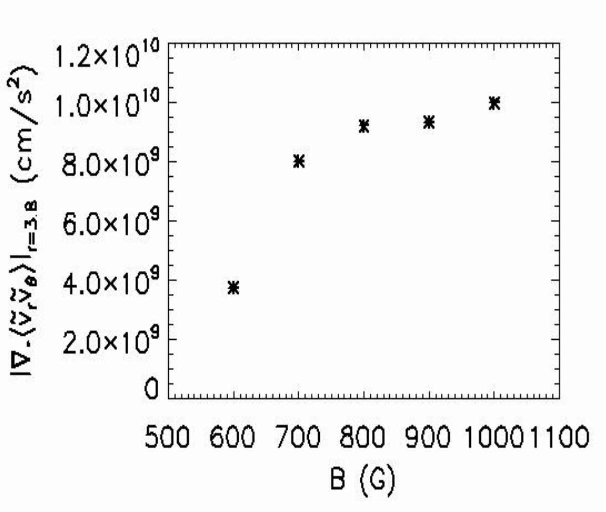

Figure 5.5: Absolute value of the divergence of the turbulent Reynolds stress at shear layer (~ 3.8cm) for different magnetic fields.

we used a very high (∼million-Angstrom) resolution spectrometer to make the necessary measurements. Unfortunately that instrument is not available and thus such measurements and the corresponding momentum analysis must be deferred until such time that the measurements can be made.

5.3 Neutral gas pressure scaling of the turbulence driven shear flow

Since the neutral gas pressure is also a possible parameter to control the transition to turbulence[43, 44] and the ion-neutral drag can also damp out turbulence driven shear flow[59], we have studied the evolution of the drift turbulence and sheared zonal flow for various neutral gas pressures, while keeping the other discharge conditions con-

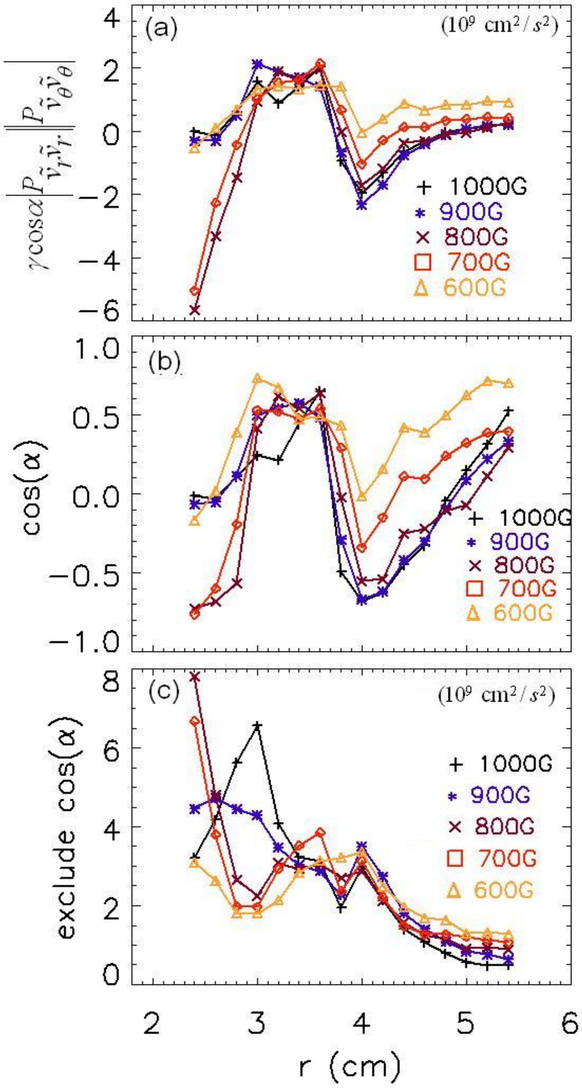

Figure 5.6: (a) Turbulent Reynolds stress computed in frequency domain using Eqn.2.13. (b) Cosine of the cross-phase. (c) Cross-phase is excluded from Eqn.2.13.

stant (a magnetic field of 1000G and a source power of 1.5kW were used). Fig.5.7 shows the radial distribution of the equilibrium plasma density for different neutral gas pressures while Fig.5.8 presents the variation of the density fluctuation amplitude and radial particle flux at 1000G for data obtained at r=3cm. Each quantity is normalized by the corresponding value at 1000G, 4mTorr Argon plasma condition. The results show that the plasma density increases with neutral gas pressure while the density fluctuation amplitude decreases with increasing neutral gas pressure. The radial particle flux peaks at 3.18mTorr and decreases for higher pressures. Fig.5.9 shows the time-averaged radial profile of the azimuthal velocity fields at 1000G magnetic field for different neutral gas pressures. The results show that the shear flow velocity and the overall shearing rate decrease with the neutral gas pressure. The power spectra of both density fluctuations and floating potential at shear location (∼3.8cm) for various neutral gas pressures at 1000G magnetic field are shown in Fig.5.10. It is found that the amplitude of the 8∼10kHz drift wave turbulence decreases with neutral gas pressure, consistent with our earlier observations linking the shear flow to the 8∼10kHz components of the drift wave turbulence. We note that there is also decrease in the amplitude of the low frequency (<2kHz) floating potential oscillation associated with the shear flow as the neutral gas pressure is increased. Thus an increase in the neutral gas pressure reduces the turbulence amplitude (which is the nonlinear drive for the shear flow) and also increases the flow damping rate. As a result, at higher gas pressure the shear flow becomes weaker.

The divergence of the turbulent Reynolds stress $\nabla \cdot (\tilde{v}_r \tilde{v}_\theta)$ at the shear layer (∼3.8cm) decreases with an increase in the neutral gas pressure(Fig.5.11), again consis-

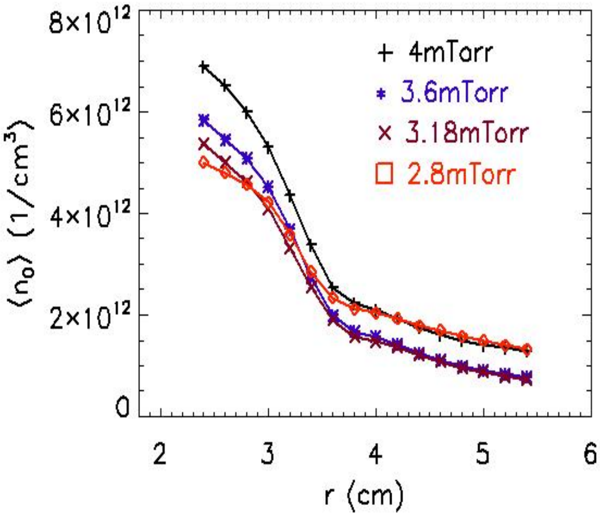

Figure 5.7: Equilibrium plasma density for different discharge pressures.

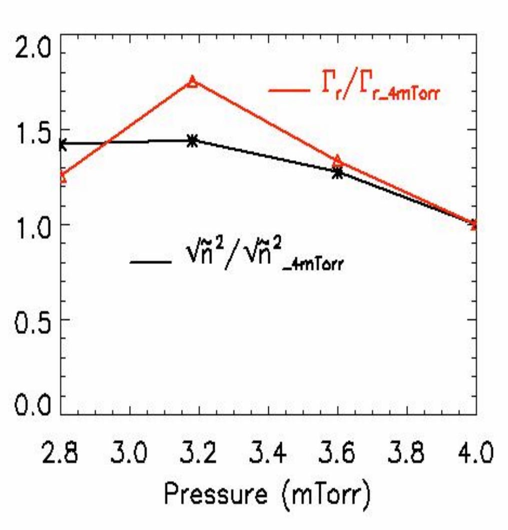

Figure 5.8: Density fluctuation amplitude (black solid line and symbol $\star$) and radial particle flux (red solid line and symbol Δ) at 1000G magnetic field for different discharge pressures. Each is normalized by the corresponding value at 4mTorr pressure.

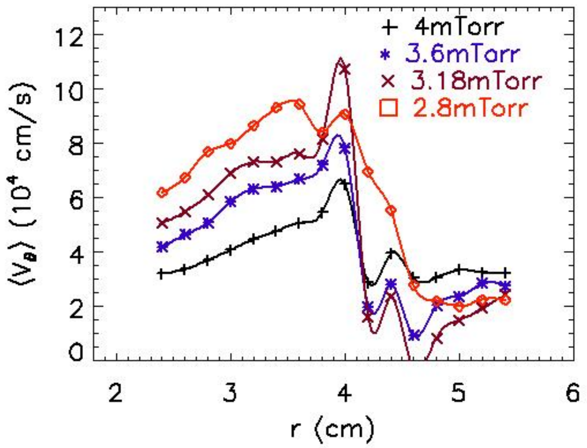

Figure 5.9: Time-averaged azimuthal velocity fields for different discharge pressures.

tent with expectations. An examination of the role of the cross-phase and cross-coherence shows that this decrease is caused in large part by the variation of the turbulent velocity cross phase (Fig.5.12) together with the reductions in fluctuation amplitude discussed above. Ideally it would also be interesting to look at the ion momentum balance equation, Eqn.4.2, for different pressure conditions. However, due to the same reason we explained in the previous section, we will defer this work to the future.

5.4 Discussion and Concluding Comments

These results show that as the relative strength of the convective derivative term to the viscous damping term is increased by increasing the magnetic field, a sheared $m = 0$ flow develops. The onset of this flow coincides with a rapid increase in the divergence of the turbulence Reynolds stress at the spatial location where the shear layer

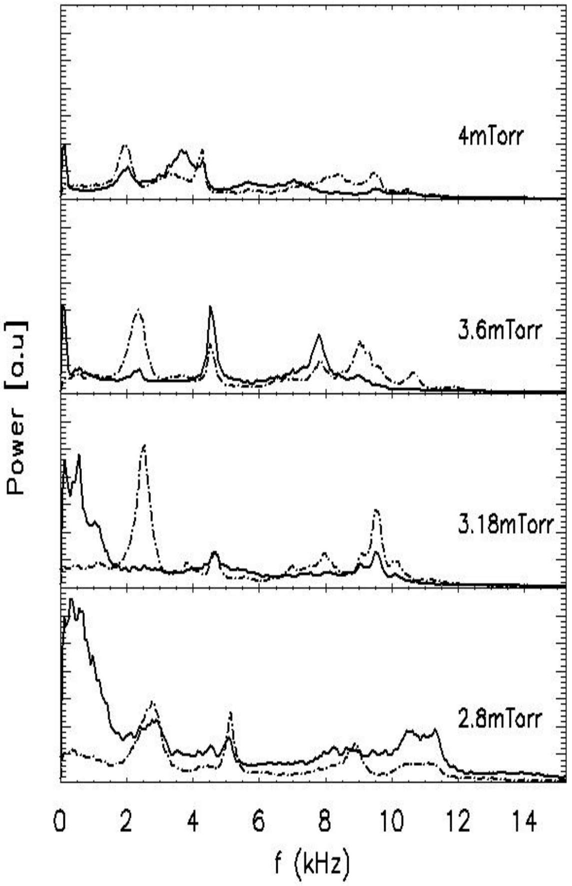

Figure 5.10: Power spectra of density fluctuations (dashed line) and floating potential (solid line) at shear layer (~ 3.8cm), 1000G magnetic field, for different discharge pressures.

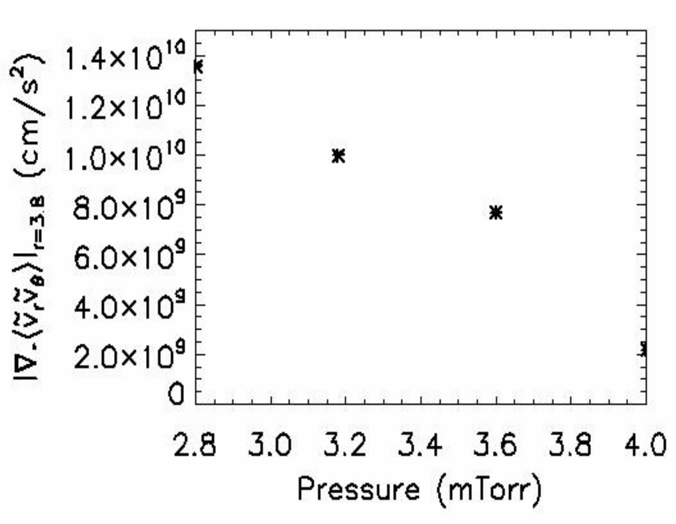

Figure 5.11: Absolute value of the divergence of the turbulent Reynolds stress at shear layer (~ 3.8cm) for different discharge pressures.

develops. In addition, the onset of the shear flow coincides with the rapid growth in the drift turbulence frequency components that are most strongly phase coherent with the slowly varying shear flow. As has been shown elsewhere[25], this phase coherency is a necessary condition to transfer energy from the turbulence into the shear flow. Finally, the shear flow is damped when the net ion-neutral collision rate is increased. When coupled with previous studies that show that the turbulent Reynolds stress is self-consistent with the shear layer, these parametric variation studies provide additional strong evidence that the shear flow is indeed driven by the turbulence and, in turn, regulates the turbulence and associated transport rates.

These parameter scan studies have important implications. Theory and numerical

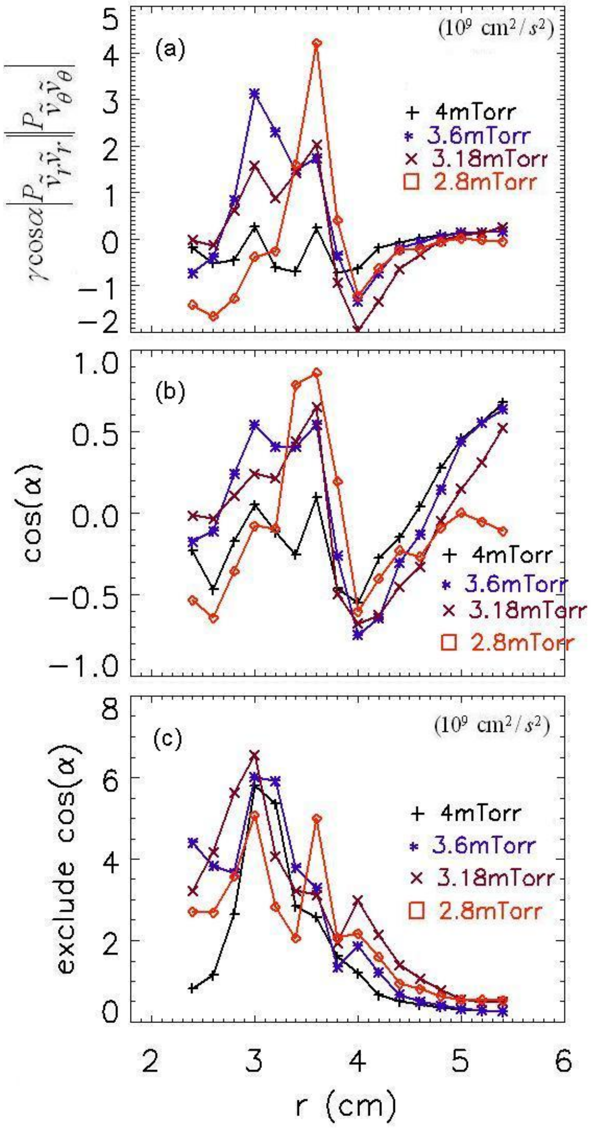

Figure 5.12: (a) Turbulent Reynolds stress computed in frequency domain using Eqn.2.13. (b) Cosine of the cross-phase. (c) Cross-phase is excluded from Eqn.2.13.

simulation of the coupled drift turbulence/ZF system in large fusion experiments show a critical gradient behavior in which the turbulence transport and the ZF are weakly driven when the mean plasma pressure gradient is below a critical value. When this critical gradient is then exceeded e.g. by increasing the heat flux through the system, the turbulent transport and the ZF both are predicted to then increase rapidly. This behavior then forces the system to stay close to the critical gradient, resulting in pressure gradients that are ”stiff” - i.e. the gradients do not depend sensitively upon the heat flux. As a result, the central plasma conditions (which are essential for achieving energy gain in a fusion reactor) are determined in large part by the conditions at the plasma boundary, where other physics mechanisms associated with the transition to open magnetic field lines and plasma-wall interactions become important. This behavior has been observed in large confinement experiment and simulation, but the key turbulence/ZF dynamics responsible for this behavior have never been studied in a confinement experiment.

The results discussed here provide the first such study for the coupled DWT/ZF system in a plasma experiment. The critical gradient behavior relates the flux Γ to the gradient scale length via a relation in the form [83],

$$\Gamma = \Gamma_s(\frac{\rho_s}{L_\perp} - \frac{\rho_s}{L_\perp}|_{crit})^\alpha H(\frac{\rho_s}{L_\perp} - \frac{\rho_s}{L_\perp}|_{crit}) + \Gamma_0 \tag{5.1}$$

where $\frac{\rho_s}{L_\perp}$ and $\frac{\rho_s}{L_\perp}|_{crit}$ denote the normalized actual and critical inverse pressure gradient scale length, H() denotes the Heaviside step function, and the saturated and the minimal fluxes are given as Γ_s and Γ_0 respectively. The parameter α is usually referred to as the ”stiffness” parameter and determines how quickly the flux increases once the critical gradient is exceeded.

The HW model[26] shows that the dimensionless critical gradient scales as,

$$\frac{\rho_s}{L_\perp}|_{crit} \propto \frac{\mu_{ii}}{\rho_s^2 \Omega_{ci}} = \frac{3}{10}\frac{\rho_i^2 \nu_{ii}}{C_s^2}\Omega_{ci} \tag{5.2}$$

where the usual Braginskii expression for the ion-ion viscosity is used. Taking note of the scaling of the ion-ion collision frequency and using the definitions of the other terms we can then re-write this scaling as

$$\frac{\rho_s}{L_\perp}|_{crit} \propto \frac{n}{T_i^{1/2} T_e^{3/2}} \propto \frac{1}{B^\alpha}, 0 < \alpha < 1 \tag{5.3}$$

where in the last scaling we have taken note that the density does not vary strongly with (Fig.5.1) and we have used earlier results[19] where the ion and electron temperature variation with magnetic field was measured. Thus we then expect that if $\frac{1}{L_\perp} \approx const$ as B is raised (as seen in the experiment) then at some critical value $B = B_{crit}$ then the inequality $\frac{1}{L_\perp} > \frac{1}{L_\perp}|_{crit}$ will occur and the fluctuations will increase rapidly. Since the turbulence in turn drives the shear flow, we would also expect a rapid onset of the shear flow. Then, when the shear flow becomes strong enough, it should then begin to affect the turbulence amplitude and correlation lengths via the shear decorrelation process summarized in Chapter 1 and discussed extensively in the literature[8]. The results shown in Fig.5.2 and Fig.5.3b, i.e. experimentally observed variation of the turbulence amplitude, cross-field flux, and ZF shearing strength verses magnetic field for the 3.18mTorr 1.5kW Argon discharges studied in most of this dissertation, have demonstrated such expected behavior - namely a rapid increase in turbulence amplitude, particle flux, and turbulent-driven shear flow as the critical gradient, which occurs between 600G<B <700G, is exceeded. As a result, one would expect the density profile to exhibit a very stiff behavior once the critical magnetic field is exceeded. This is indeed the case as seen by a careful examination of Fig.5.1.

The experimental results presented here have also shown that when the neutral gas pressure is increased, the increased ion-neutral drag begins to damp the shear flow. Recent simulation on edge momentum transport has shown that with increase in damping term (viscosity) the shear flow is reduced because the instability growth rate and the resulting nonlinear processes are all slowed down[72]. Our observations appear to be consistent with this simulation result. As what we have pointed out in the discussion of Chapter 4 the shear layer in all conditions lies at the bottom or foot of the steep pressure gradient, and that this region is determined by the radius of the heat input into the system (which is the source size).

6

Conclusion and future work

In this chapter the results from Chapter 3, Chapter 4 and Chapter 5 are summarized. The contributions to current plasma drift turbulence and structure formation studies are discussed. Future work based on the accomplishments of present work is recommended and discussed.

6.1 Summary of present work

Theories of the drift wave turbulence have been extensively studied and described, notably the early works of Hasegawa & Mima [18], Hasegawa & Wakatani[26]. Later based on their model, numerical simulations[84, 85] confirmed the same predictions: for 2D fluid dynamics a dual cascade of energy and enstrophy wherein the kinetic energy is transfered to the largest scales and enstrophy is transfered to the smallest scales resulting in a formation of the large-scale coherent structure and zonal flows. Experimentally, the generation of such large-scale coherent structure and zonal flows associated with the transport barrier has been observed on various magnetic confinement devices as we have described in Chapter 1. However, there are some limitations of the existing experiments. Because the plasma on most large scale magnetic confinement plasma device has high electron temperature and density, it is difficult to direct measure the Reynolds stress with Langmuir probe. Therefore, to date, there have been no studies of how the turbulent statistics lead to the development of the detailed Reynolds stress profile associated with the shear flow. Since the theory suggests that the Reynolds stress plays an important role in the shear flow generation process, it would be desired and significant to study the detailed statistical properties of the Reynolds stress. In addition most experiments carried out on the large-scale plasma device are already in ’turbulent’ state, therefore there is no way to study the scaling properties of the shear flow generation during the transition to turbulence. On the other hand, most experiments have confirmed the formation of the transport barrier during the transition from L mode to H mode, but to the author’s knowledge there have been no conclusive studies of the relationship between the particle transport, Reynolds stress and shear flow generation. Theories and simulations have effectively predicted and interpreted the drift-wave turbulence/zonal flow dynamics, however, no detailed experiments have provided a full validation of such basic theories. In light of this state of affairs at the beginning of this thesis we identified four questions to be answered by this experimental work:

1. As a state of turbulence is approached, what statistical properties lead to the development of the Reynolds stress and what are their contributions to the shear flow generation?

2. What is the relationship, if any, between the universally observed ion-saturation current bursty events, momentum transport and shear flow generation?

3. Is there any evidence in the experiments confirming the theoretical picture of the drift-wave turbulence/zonal flow self-regulated dynamical system?

4. What are the scaling properties of the turbulence driven shear flow during the transition to turbulence?

To address these questions we proceeded as follows: From previous studies we understand the plasma on CSDX undergoes a transition from discrete mode (below 600G) to broad-band turbulence (1000G) with increasing magnetic fields and the known source of free energy driving this turbulence has been identified as the radial electron pressure gradient. Therefore, for the first set of experiments we choose our background plasma condition to give a state of drift turbulence in the plasma. In these conditions we then studied the statistical properties of the turbulent Reynolds stress and shear flow dynamics. For the scaling properties of the shear flow investigation, the measurements were made in various magnetic fields and neutral pressures. We used a novel multi-tip Langmuir probe array that was designed to have 18tips that were distributed in a way that allow the computation of Reynolds stress and various statistical properties analysis. This probe diagnostic was complemented by the use of a new fast-framing camera that was coupled to a telescope to capture the visible light emission from plasma providing for the first time the capability of visualizing the turbulence structure formation and evolution in the presence of a sheared zonal flow.

For the first question, 'As a state of turbulence is approached, what statistical properties lead to the development of the Reynolds stress and what are their contributions to the shear flow generation?', the results in this thesis provide answers through two lines. First, by decomposing the Reynolds stress into the cross-coherence γ, the cross-phase α and the auto-power of the radial and azimuthal velocity fields $S(v_r v_r), S(v_\theta v_\theta)$, and analyzing how significant of each component in determining the Reynolds stress profile, we found that the cross-phase between the two components of the velocity fields $\alpha_{v_r v_\theta}$ plays key role in determining the detailed Reynolds stress profile, which drives the shear flow. Second, we found the Reynolds stress PDF is non-Gaussian and positively skewed at the observed shear flow location. Momentum transport therefore behaves like bursty density transport events that have been reported earlier, and is concentrated in the region of the shear layer. The radial and azimuthal velocity fields are in phase at shear layer, but out of phase beyond this region. This results in a radial variation of the Reynolds stress and the negative divergence of the Reynolds stress which reinforce the shear flow.

For the second question, 'What is the relationship between the universally observed ion-saturation current bursty events, momentum transport and shear flow generation?', the results in this thesis show that these three are all linked. Firstly, the PDF of Reynolds stress and ion-saturation current are found both non-Gaussian and the regions of positive stress and density skewness coincide with each other. This suggests that the bursts of particle transport is associated with bursts of momentum transport. A study of the joint PDF between particle flux and Reynolds stress confirmed the relationship between the particle transport and the momentum transport.

We used these results to construct a physical picture of the shear flow generation:

The bursts of outward going density fluctuations born near the maximal density gradient location carry angular momentum, resulting a positive Reynolds stress in that region. As they are propagating away from the maximal density gradient and towards the shear layer the fluctuation amplitude decreases resulting in a decreasing Reynolds stress and hence a negative divergence of the Reynolds stress which drives or reinforces the shear flow. These results indicate a system of radially propagating turbulence structures which are immersed within a background seed shear flow naturally form a Reynolds stress profile that then acts to reinforce the shear flow.

For the third question, 'Is there any evidence in the experiments confirming the theoretical picture of the drift-wave turbulence/zonal flow self-regulated dynamical system?', the results in this thesis have provided six observations that qualitatively support the expected theoretical picture. First, we have observed an existence of shear flow through the Langmuir probe measurements by applying TDE technique to the floating potential measured from two azimuthally adjacent probe tips. A 2D velocimetry study obtained from fast-framing imaging has directly confirmed, for the first time, the azimuthally symmetry of this shear flow. Second, spectral analysis of the azimuthal velocity field both from probe and fast-framing imaging show that such shear flow evolves with a low frequency about $\sim$250-300Hz. Quantities associated with higher frequency ($\sim$5-15kHz) drift turbulence such as floating potential, Reynolds stress and particle flux are all modulated at the same low frequency. Third, detailed ion momentum balance analysis show that such slow evolving shear flow is sustained by the Reynolds stress against collisional and viscous damping with a reasonable estimation of the stationary ion-ion viscosity coefficient. Fourth, a bi-coherence of the floating potential calculation shows the $\sim$300Hz oscillation is phase coherent with the 10kHz turbulence which suggests the energy transfer between these two could indeed happen. Five, the high frequency turbulence (5kHz above) kinetic energy is found to be anti-correlated with the low frequency range (0-2kHz), but no correlation is found between the intermediate frequency range (2-5kHz) and the low frequency range, which is qualitatively consistent with the theoretical picture of the energy conservation between turbulence kinetic energy and shear flow energy. Six, fast-framing imaging shows the radial turbulence correlation length is anti-correlated with the flow shear. Thus when the shearing rate is strong, the radial turbulence correlation length is small, and vice versa. This is consistent with the decorrelation process of the turbulence by the shear flow. Taken together, the results in this thesis have provided evidences qualitatively consistent with the theoretical picture of the drift-wave turbulence/shear flow as a self-regulated dynamical system.

For the fourth question, 'What are the scaling properties of the turbulence driven shear flow during the transition to turbulence?' the results in the present work have shown that the higher the magnetic fields the stronger the shear flow, and the lower the neutral pressure the stronger the shear flow. There is a critical value of the magnetic field (which results in a critical value of the inverse of the normalized density gradient scale length), above which both turbulence and shear flow are spontaneously excited. When the magnetic field is increased above this critical value, the drift wave turbulence amplitude and zonal flow shearing rate both increase rapidly as might be expected for a system that follows a critical flux-gradient type of behavior. When the neutral gas pressure is increased, the drift wave turbulence is decreased due to the increase of the damping coefficients from ion-neutral drag. The resulting decreasing divergence of the turbulent Reynolds stress causes a reduction of the shear flow amplitude. In both situation the cross-phase between the radial and azimuthal velocity components is critical to determine the turbulent Reynolds stress profiles for various plasma conditions. Taken together the results have suggested a causal relationship between the drift wave turbulence and shear flow for various plasma conditions.

6.2 Limitations of present work

In this thesis we have demonstrated experimentally that the shear flow generation is due to the the momentum transport which is carried by the outward going density bursts and also provided experimental validation of the theoretical picture of the drift-wave turbulence/zonal flow dynamical system, as well as an investigation of the scaling properties of the shear flow. However, in the work presented in the thesis there are several limitations needed to be kept in mind.

Firstly, in current work we use floating potential ϕ_f instead of plasma potential ϕ_p to compute the electric field, i.e., $E = \dfrac{\Delta\phi_f}{\Delta x}$, where Δx is the distance between the two spatial locations of floating potential. By applying this we assume there is no significant electron temperature fluctuations. This assumption is used by many experimentalists. However this has not been confirmed in our experiments yet. And we also do not know the spectral properties of the electron temperature fluctuations. This uncertainty could cause error in the calculation of turbulent Reynolds stress and kinetic energy.

Secondly, in current work there is no detailed measurements of spatial profile of ion and neutral temperature. Therefore the spatial profiles of the damping coefficients, i.e., ion-ion viscosity coefficient μ_{ii} and ion-neutral collision rate ν_{in} are assumed in the computation of ion momentum balance equation. For the ion-neutral collision rate we assumed a constant profile along radial direction and for the ion-ion viscosity coefficient we assume a quasi-step function like profile since the $\mu_{ii} \propto n_i T_i^{-2}$ and the density n_i and ion temperature T_i drop at large radii. In addition we do not have measurements of time varying damping coefficients. Therefore in studying the dynamics of the shear flow we assumed a time-stationary damping coefficients. These may cause error in the ion momentum balance analysis and maybe one of the reasons of the not high value correlation between the initial term and force term in the ion momentum equation. In the analysis of the scaling properties of the shear flow we are not able to perform a detailed analysis of the ion momentum balance equation for various plasma conditions due to the lack of the damping coefficients.

Thirdly, we assume the light emission intensity from plasma is somewhat correlated with the plasma density fluctuation. However, we do not understand the detailed relationship between these two so far. The light emission intensity is thought to be not only correlated with the plasma density fluctuation but also correlated with electron temperature and neutral density. Therefore we should note the velocity field inferred from light emission intensity of the plasma does not only exactly reflect the velocity of the plasma density fluctuations.

6.3 Recommended future work

Based on the accomplishments and the limitations of the present work there are a number of ways that maybe furthered as we have mentioned sporadically throughout Chapter 3, Chapter 4 and Chapter 5. In this last section we will describe what future work will be profitable.

6.3.1 Measuring electron temperature T_e

The most straightforward way to measure electron temperature is to measure the current-voltage characteristic (I-V curve) of the plasma by applying an oscillating (or sweeping) voltage to a single probe tip at a frequency about 100Hz[19]. As the voltage is more positive than the floating potential, the current and voltage satisfy the relationship $I \propto \exp(\frac{-e\phi_p}{kT_e})$[48]. The electron temperature is then found to be the inverse of the slope of the straight line of this I-V trace on a semi-logarithmic plot. The electron temperature found this way has limited information of the fluctuation properties since it is an average value over the sweeping frequency. To validate the assumption that we used in our work, i.e., the electron temperature fluctuation is negligible, fast electron temperature measurement should be made. One possible method is to use triple probe, consisting of two electrodes biased with the same voltage and a third which is floating. The schematic is shown in Fig.6.1. The electron temperature is computed as $kT_e = \frac{e(V_e - V_f)}{ln(1 + \frac{A_i}{A_e})}$, where V_e and V_f are the voltage of the electron collecting tip and floating tip respectively, and A_i and A_e are the collecting area of the ion tip and electron tip respectively.

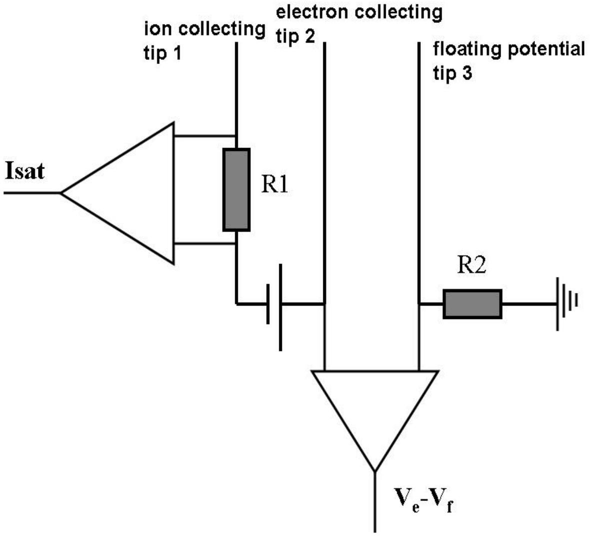

Figure 6.1: Schematic of triple probe measurment.

6.3.2 Measuring ion temperature T_i and neutral temperature

Measurements of ion and neutral temperature should be made in the future by spectroscopy. This would allow the better estimation of damping coefficients, i.e, ion-neutral collisional rate and ion-ion viscosity coefficient, and hence the ion momentum balance analysis. This could be performed by measuring the ArI (750nm) and ArII (488nm) doppler broadening and deconvolution with Gaussian instrument response at multiple chords. These results would then need to be Abel inverted to obtain the desired radial ion and neutral gas temperature profiles.

6.3.3 Measuring bulk ion flow velocity

In the present work we assume the convecting velocity is dominated by the $\vec{E} \times \vec{B}$ flow since the ion-ion collisional rate is marginally below the ion cyclotron frequency $\frac{\nu_{ii}}{\Omega_{ci}} \sim 0.3 - 1.0$. However, to be precise the bulk ion flow is not exactly $\vec{E} \times \vec{B}$ flow when $\nu_{ii} \sim \Omega_{ci}$, especially at low magnetic field. Therefore the bulk ion flow velocity should be made. This quantity could in principal measured from the Doppler-shift of Ar-II emission lines or alternatively from Laser-Induced Fluorescence (LIF) technique[86].

6.3.4 Changing source diameter

In the present work the RF source diameter is about 10cm. This dimension determines the size of the plasma column, the location of the maximal pressure gradient, and hence the shear layer position. To exam this a larger source could be used in the future work to demonstrate that the shear layer is indeed linked to the pressure gradient region and thus to the source diameter.

6.3.5 Studying the relationship between the light emission intensity from the plasma and plasma parameters

Fast-framing imaging is a promising technique to study the plasma turbulence. It has been utilized broadly in studying the basic physics of shear flow. A critical issue of this technique is to understand the relationship between the measuring emission light intensity from plasma itself or neutral beam injected into the plasma and the plasma parameters, such as plasma density and temperature. It has been considered in previous work that the light emission intensity I is proportional to nT^{α}[49] with $\alpha \sim 3/4$ and in measurements in DIIID that $\frac{\tilde{n}}{n} = C(\frac{\tilde{I}}{I})$, where $\tilde{I}$ is the fluctuation of light emission intensity and $\tilde{n}$ is plasma density fluctuation. C is a proportional factor depending on the plasma density, temperature, and beam energy. For typical DIIID plasma parameter, $C \sim 2-3$[87]. In our linear machine CSDX, however, this relationship has not been studied in details and quantified. It is currently performed underway by others in our research group.

6.3.6 Increase resolution of B field strength from 600G to 700G

In the investigation of the scaling properties of the shear flow we have demonstrated that the shear flow is getting stronger when the magnetic field is increased close to or above 700G. No shear flow is observed when the magnetic field is as low as 600G. It would be very interesting to increase the resolution of B field strength from 600G to 700G to clarify the detailed transition from no shear flow to the onset of shear flow.

6.3.7 2D turbulence structure evolution from probe measurements

In the present work fast-framing imaging has been used to provide important information of the turbulent structure formation and evolution. However, due to the uncertainty information of the relationship between the light emission intensity and the plasma parameters (plasma density and temperature), it would be useful to study the 2D turbulence structure evolution from probe measurements. This would require a 2D probe array to be made. This probe array should cover an area of about several cm^2 since the average radial and azimuthal turbulence correlation length are a few cm. A series of conditional averaging and 2D cross-conditional averaging could then be applied to study the turbulent structure evolution. Wave number spectrum could also be obtained directly from 2D probe array instead of previous two-point technique. However, it should be noted that larger probe array might perturb more to the plasma. Therefore it would be useful to use both 2D probe array and fast-framing imaging technique and compare their results.

6.3.8 Dynamical bi-spectral analysis of the energy transfer

In the present work we have shown in the configuration space that the time-varying shear flow is sustained by the turbulent Reynolds stress against collisional and viscous damping. This would also be manifested by the three-wave coupling processes from bi-spectral analysis in the frequency domain. Since the shear flow and turbulence are in a self-organization dynamical system with ∼250-300Hz frequency, the bi-spectral should in principal also indicate this time varying property. To do this a very long time data would be needed and short time windows would be applied.

Bibliography

[1] Jeffrey Freidberg, Plasma physics and fusion energy, Cambridge university press, 2007

[2] J. D. Lawson, Proceedings of the Physical Society B, Vol. 70, p. 6 (1957).

[3] George R. Tynan, A proposal for a controlled shear decorrelation experiment (CSDX), Jan. (1999).

[4] B. Carreras, IEEE Trans. Plasma Sci. 25, 1281, (1997).

[5] G.R.McKee et al., Phys. Plasmas 10, 1712, (2003)

[6] G. R. McKee, R. Ashley, R. Durst, R. J. Fonck et al., Rev. Sci. Instrum. 70, 913 (1999).

[7] J. L. Luxon, Nucl. Fusion 42, 614 (2002)

[8] P.H.Diamond et al., Plasma Phys. Control. Fusion 47, R35, (2005).

[9] X Garbet, Plasma Phys. Control. Fusion 43, A251, (2001)

[10] M.N.Rosenbluth and F.L.Hinton, Phys.Rev.Lett. 80, 724, (1998)

[11] F.L.Hinton and M.N.Rosenbluth, Plasma Phys. Controlled Fusion, 41, A653, (1999)

[12] K.Hallatschek and D.Biskamp, Phys. Rev. Lett., 86, 1223, (2001)

[13] T.S.Hahm, K.H.Burrell, Z.Lin, et al., Plasma Phys. Controlled Fusion, 42, A205, (2000)

[14] K.H.Burrell, Phys. Plasma 4, 1499 (1997).

[15] R.E.Bell, et al., Plasma Phys. Control. Fusion 40, 609 (1998).

[16] F.F Chen, Introduction to Plasma Physics, Plenum Press, New York, (1974)

[17] W. Horton, Rev. Mod. Phys. 71, 735 (1999).

[18] A. Hasegawa, et al., Phys. Rev. Lett. 39, 205, (1977).

[19] M. J. Burin,et al., Phys. Plasma, 12, 052302, (2005).

[20] A. Dinklage, T. Klinger, G. Marx, and L. Schweikhard, Plasma Physics (Confinement, Transport and Collective Effects), Springer-Verlag Berlin Heidelgerg, 175, (2005).

[21] E. Pope, Turbulent Flow (Cambridge: Cambridge University Press), (2002).

[22] T.H.Kraichnan, Phys. Fluids, 10, 1417, 1967

[23] J. C. McWilliams, J. Fluid Mech. 146, 21, (1984).

[24] P. Tabeling, Phys. Rep. 362,1,(2002).

[25] G.R.Tynan, R.A.Moyer, et al., Phys. Plasmas 8, 2691, (2001)

[26] A. Hasegawa and M. Wakatani, Phys. Rev. Lett. 59,1581, (1987)

[27] H. Biglari, P.H.Diamond, and P.W.Terry, Phys. Fluids B 2, 1 (1990).

[28] C.P.Ritz,Phys. Fluids, 27, 2956, (1984)

[29] C.Holland, Rev. Sci. Instrum. 75, 4278 (2004)

[30] A.Fujisawa, T.Ido, A.Shimizu, S.Okamura, K.Matsuoka, et al., Nucl. Fusion, 47, s718, (2007)

[31] A. Fujisawa, K.Itoh, H.Iguchi, K.Matsuoka, S.Okamura, et al., Phys. Rev. Lett. 93, 165002, (2004)

[32] A. Fujisawa, et al., Plasma Phys. Control. Fusion 48, A365 (2006)

[33] T.Ido, Y.Miura, K.Hoshino, K.Kamiya, Y.Hamada, et al., Nucl. Fusion, 46,512,(2006)

[34] A.V.Melnikov, V.A.Vershikov, L.G.Eliseev, S.A.Grashin, et al., Plasma Phys. Controlled Fusion, 48, s87, (2006)

[35] P. M. Schoch, K. A. Connor, D. R. Demers, and X. Zhang, Rev. Sci. Instrum. 74, 1846 (2003)

[36] G.R.Mckee, et al., Plasma Phys. Control. Fusion 45, A477 (2003)

[37] G.D. Conway, B. Scott, J. Schirmer, M. Reich, A. Kendl and the ASDEX Upgrade Team, Plasma Phys. Control. Fusion 47 1165, (2005)

[38] C. Hidalgo, et al., in Proceedings of the 17th Conference on Plasma Physics and Controlled Nuclear Fusion Research (Report No. IAEA-F1-CN-69/EXP1/20), (1998)

[39] Y.H.Xu, et al., Phys. Rev. Lett. 84, 3867, (2000)

[40] A. Fujisawa, et al., Plasma Phys. Contol. Fusion 48, S205 (2006)

[41] G.R.Tynan, C. Holland, et al., Plasma Phys. Control. Fusion 48, S51, (2006)

[42] C. Holland, G.R Tynan, et al., Plasma Phys. Control. Fusion 49, A109, (2007)

[43] L. I and M. Wu, Phys. Lett. A 124, 271, (1987)

[44] D. Weixing, H. Wei, W., Xiaodong, and C. X. Yu, Phys. Rev. Lett. 70, 170, (1993).

[45] G.R.Tynan, et al., J. Vac. Sci. Tech-A, 15, 2885, (1997)

[46] P. H. Diamond and Y.B. Kim, Phys. Fluids B 3, 1626, (1991)

[47] S.J.Zweben and S.S.Medley, Phys. Fluids B, 1, 2058, (1989)

[48] I.H.Hutchinson, Principles of Plasma Diagnostics (Cambridge University Press, Cambridge,1987)

[49] G.Y.Antar, J.H.Yu, and G.R.Tynan, Phys. Plasmas, 14, 022301, (2007)

[50] M. Jakubowski, R.J.Fonck, and G.R.McKee, Phys. Rev.Lett. 89, 265003 (2002)

[51] Ch.P.Ritz, E.J.Powers, and R.D.Bengtson, Phys. Fluids B 1, 153 (1989)

[52] C. Holland, G.R.Tynan, G.R.McKee, and R.J.Fonck, Rev. Sci. Ins. 75, 4278 (2004)

[53] J.M.Beall, Y.C.Kim, and E.J.Powers, J. Appl. Phys. 53, 3933, (1982)

[54] G. R. McKee et al., Rev. Sci. Instrum. 75, 3490 (2004)

[55] A. Hasegawa and M. Wakatani, Phys. Rev. Lett. 50, 682, (1983)

[56] J.H.Yu, C.Holland, G.R.Tynan, G. Antar, Z. Yan, J. Nucl. Materials, 363, 728, (2007)

[57] E. J. Powers, Jae Y. Hong, and Christoph P. Ritz, Applied Digital Time Series Analysis (Preliminary Version), 1986

[58] C. Hidalgo, et al., Plasma Phys. Controlled Fusion, 37, A53 (1995)

[59] C. Holland, et al., Phys. Rev. Lett. 96, 195002, (2006)

[60] C. Hidalgo, C. Silva, et al., Phys. Rev. Lett. 83, 2203, (1999)

[61] V Antoni, E. Spada, et al., Plasma Phys. Controlled Fusion, 47, B13, (2005)

[62] G. S. Xu, B. N. Wan, et al., 20th IAEA Fusion Energy Conf. Vilamoura, Portugal, IAEA-CN-116/EX/8/-4Rb, (2004)

[63] J.Boedo, D. Rudakov, et al., Phys. Plasmas 8, 4826, (2001)

[64] R. Sanchez, B. Ph. van Milligan, et al., Phys. Rev. Lett., 90, 185005, (2003)

[65] P. H. Diamond and T.S.Hahm, Phys. Plasmas, 2, 3640, (1995)

[66] A. Smolyakov00, P.H.Diamond and M. Malkov, Phys. Rev. Lett., 84, 491, (2000)

[67] T.R.Carter, Phys. Plasmas, 13, 010701, (2006)

[68] H.Biglari, P.H.Diamond and P.W.Terry, Phys. Fluids-B 2, 1 (1990)

[69] C. Hidalgo, B. Goncalves, et al., Phys. Rev. Lett. 91, 065001, (2003)

[70] E. Kim and P.H.Diamond, Phys. Rev. Lett. 88, 225002, (2002)

[71] S.H.Muller, A. Diallo, et al., Phys. Plasmas, 14, 110704, (2007)

[72] J.R.Myra, D.A.Russell, and D.A.D'Ippolito, Phys. Plasmas, 15,032304, (2008)

[73] S.I.Braginskii, Reviews of Plasma Physics, edited by M.A.Leontovich, 1, 205, (1965)

[74] K. Itoh, S.-I. Itoh, P. H. Diamond, T. S. Hahm, A. Fujisawa, G. R. Tynan, M. Yagi, and Y. Nagashima, Phys. Plasmas 13, 055502 (2006)

[75] K. C. Shaing and E. C. Crume, Jr., Phys. Rev. Lett. 63, 2369 - 2372 (1989)

[76] P.H.Diamond et al., Phys. Rev. Lett. 84, 4842 (2000)

[77] Z.Yan, J.H.Yu, C.Holland, M.Xu, S.H.Muller, G.R Tynan, Phys. Plasmas, 15, 092309 (2008)

[78] M. Xu, G. R. Tynan, C. Holland, Z. Yan, S. H. Muller, J. H. Yu, 'A Two-field Model for Studying Nonlinear Energy Transfer in Frequency Domain', to be submitted.

[79] A. Fujisawa, A.Shimizu, H. Nakana, S. Ohsima, K. Itoh, H. Iguchi, K. Matsuoka, S. Okamura, S-I Itoh and P H Diamond, Plasma Phys. Control. Fusion, 48, A365, (2006)

[80] T. Windisch, O. Grulke, and T. Klinger, Phys. Plasmas, 13, 122303, (2006)

[81] U. Kauschke and H. Schluter, Plasma Phys. Controlled Fusion 32, 1149, (1990)

[82] U. Kauschke, Plasma Phys. Controlled Fusion 35, 93, (1993).

[83] F. Ryter, et al Plasma Phys. Controlled Fusion, 48, B453, (2006)

[84] S.J.Camargo, D.Biskamp and B.D.Scott, Phys. Plasmas, 2,48,(1995)

[85] D.Biskamp and A. Zeiler, Phys. Rev. Lett., 74, 706, (1995)

[86] J.L.Kline et al., Phys. Rev. Lett., 88, 195002, (2002)

[87] G.R.Mckee, C.Fenzi, R.J.Fonck, et al., Rev. Sci. Instrum., 74, 2014, (2003)